OPTICAL STRUCTURE-PROPERTY RELATIONS IN METAL AND SEMICONDUCTOR NANOPARTICLES

by

Nicholas J. Borys

A dissertation submitted to the faculty of
The University of Utah
in partial fulfillment of the requirements for the degree of

Doctor of Philosophy

in

Physics

Department of Physics and Astronomy

The University of Utah

May 2011

The University of Utah Graduate School

STATEMENT OF DISSERTATION APPROVAL

The dissertation of **Nicholas J. Borys**

has been approved by the following supervisory committee members:

John M. Lupton	, Chair	**3/10/2011** Date Approved
Carleton DeTar	, Member	**3/25/2011** Date Approved
Jordan M. Gerton	, Member	**3/10/2011** Date Approved
Ajay Nahata	, Member	**3/10/2011** Date Approved
Z. Valy Vardeny	, Member	**3/10/2011** Date Approved

and by **David B. Keida**, Chair of the Department of **Physics and Astronomy**

and by Charles A. Wight, Dean of The Graduate School.

ABSTRACT

The optoelectronic properties of nanoscale metal and semiconductor material systems are notably sensitive to their corresponding physical structure. Contemporary synthesis techniques enable careful control of nanoparticle configurations and therefore provide a wide array of systems where the effects of physical morphology on the interaction between nanoscale materials and light can be carefully probed. The investigated properties are immediately relevant to light-harvesting and ultra-sensitive trace-analysis and sensing applications.

In this work, the structure-property relationships of both individual semiconductor nanocrystal heterostructures and aggregates of plasmonic silver nanoparticles in rough metal films are probed. The semiconductor heterostructures behave as model light-harvesting systems where optical energy absorbed by one portion of the structure is funneled, on the nanoscale, to a model light-harvesting center, in analogy to photosynthesis. In the plasmonic silver nanostructures, collective optical excitation of the conduction electrons - plasmons - confines electromagnetic radiation to well beyond the traditional diffraction limit of light in nanoscale regions called "hot spots." Within these hot spots, light-matter interactions are greatly enhanced and thus enable trace-sensing applications such as Raman scattering from a single molecule. Thorough application of relatively simple single particle spectroscopy techniques is combined with high resolution electron microscopy to elucidate the subtle details on how physical structure controls the optical properties of both material systems.

There are four main results of this work. (1) The linear and nonlinear optical response of rough silver films is shown to be enhanced by the excitation of surface plasmon polaritons. (2) The enhanced nonlinear response of rough metal films is conjectured to originate from metal clusters, and the observation of stark fluctuations in their efficiency of second-harmonic generation is reported for the first time. (3)

The presence of and enhanced emission from silver clusters of only a few atoms plays an important role in the intrinsic optical response of the silver films with considerable implications for surface-enhanced Raman scattering. (4) The effects of physical anisotropy on the electronic states of semiconductor nanocrystals are explicitly identified through correlated optical and electron microscopy of single particles. These effects are shown to have important ramifications in the internal energy-transfer process of single nanocrystals.

CONTENTS

LIST OF FIGURES

LIST OF TABLES

ACKNOWLEDGMENTS

The completion of this work was aided by a number of people, and I am deeply indebted to them for their assistance and support:

- **Prof. John Lupton** for giving me countless opportunities, continually pushing me, and constantly inspiring me to grow scientifically. I am forever indebted to John for looking past my shortcomings as a new graduate student and giving me the opportunity to help build his new lab and then work in his group. It is impossible for me to imagine a more fruitful graduate student career without John as my adviser.

- **Prof. Carleton DeTar**, **Prof. Jordan Gerton**, **Prof. Ajay Nahata**, and **Prof. Valy Vardeny** for taking an interest in my work and the time to serve on my Supervisory Committee. I would also like to express my gratitude to Prof. Ajay Nahata for valuable scientific discussions, and to Prof. Valy Vardeny for providing me an initial opportunity to work in his labs.

- **Dr. Manfred Walter** whom I owe almost all of my practical training to, for three great years of sharing an office together, and a very cherished friendship. Manfred through his incredible attention to detail, amazing discipline and unrelenting thoroughness, continually inspired me to be a better researcher. I am forever indebted to Manfred for taking me under his wing and patiently training me.

- All of the other members of Nanoscale Optoelectronics Group including **Douglas Baird**, **Sebastian Bange**, **Debangshu Chaudhuri**,**Patrick Heissler**, **Philippe Klemm**, **Dongbo Li**, **Sue Liu**, **Alex Theissen**, and **Kipp van Schooten** for technical support, critical analysis of my data and interpreta-

tions, all of the imaginative, colorful, and fruitful scientific and nonscientific discussions, and most importantly, treasured friendships.

- **Dr. Dane McCamey** for my first successful scientific collaboration, support, inspiration and a cherished friendship.

- **Dr. Matt DeLong** and **Dr. Randy Polson** for their patience and invaluable assistance with the electron microscopy measurements.

- **Dr. Enrico Da Como** for numerous scientific discussions, a very successful collaboration and a wealth of invaluable technical advice.

- **Jing Huang** and **Prof. D. V. Talapin** who synthesized the high-quality semiconductor nanocrystals used in this work and allowed me to visit their facilities in Chicago to finalize some electron microscopy work.

- **Kathy Blair**, **Heidi Frank**, **Jackie Hadley**, **Vicki Nielsen**, **Harold Simpson**, **Kathrine Skollingsberg**, **Jolene Snyder**, and **Wayne Wingert** for administrative and facilities support.

Finally, I would like to express my deepest gratitude to my family including my parents, **Dan** and **JoAnn Borys**, my sister **Jenna Borys**, and **Stefanie Michaelson**. Their continued faith and support undoubtedly played a crucial role throughout my studies.

CHAPTER 1

INTRODUCTION

The interaction and coupling between light and material systems with nanoscale dimensions constitutes a significant portion of the forefront of contemporary materials science. The electronic properties that commonly dominate how a material interacts with electromagnetic radiation can be widely tuned for nanoscale systems through structural properties. Continuing advances in fabrication and synthesis techniques have resulted in the creation of a diverse set of nanoparticle morphologies from a wide range of materials. This work studies the effects of particle morphology on nanoparticles derived from bulk metal and semiconductor components.

The unbound conduction electrons in metal nanoparticles dominate the particle's interaction with electromagnetic radiation. Light of an appropriate frequency can excite the collective motion of the conduction electrons – an excitation referred to as a surface plasmon [1]. In bulk metals, the surface plasmons can propagate on the surface of the metal and give rise to effects such as anomalous transmission as well as enable the engineering of mesoscopic metal devices that can focus the propagating surface plasmons to suboptical-wavelength regions with, for example, a sharp tip. In contrast, nanoparticles do not support propagating surface plasmons [2]. The spatial confinement in all dimensions prevents propagation and localizes the surface plasmon excitation to the nanoparticle. Since the particle is metallic, the localized surface plasmon excitation confines the incident electromagnetic energy primarily to the surface of the nanoparticle therefore enabling enhanced interactions between light and matter within close proximity to the nanoparticle surface [3–6]. Aggregates of multiple metal nanoparticles of diverse shape and size lead to even stronger surface plasmon localization and thus stronger enhancement of light-matter interactions [7, 8]. The

enhancement of metal nanoparticle systems through either surface plasmon focusing or localization enables unprecedented sensing abilities [4] where trace amounts of analyte (down to the level of single molecules) placed within close proximity to the metal experience phenomenally enhanced light-matter interactions. In this manner, very weak interactions such as Raman scattering can be observed at the single molecule level [9].

Nanoparticles derived from semiconductor materials are distinctly different from their metal counterparts as they do not have free conduction electrons. Instead, the electrons are contained in valence band states, and the electronic properties reflect excitation of the valence electrons into conduction band states across an energetic band gap [10, 11]. The spatial confinement of the nanoparticles plays an important role in the energetic size of the band gap, and consequently, the optical properties such as absorption and emission sensitively depend on particle size and shape [12,13]. Modern synthesis techniques enable very precise tuning of particle morphology, and thus optical and electronic properties [14,15]. As a result, semiconductor nanocrystals are exciting materials for applications including light-emitting devices, photovoltaics, ultrasensitive photodectectors, nanoscale light sources, and nanoscale photocatalysts [14].

The morphological sensitivity of the electronic characteristics of nanoparticle systems can be considered a problem as much as it is a tool. For example, not all semiconductor nanocrystals will make ideal photovoltaic materials. Their structural properties must be precisely tuned to optimize optical absorption and subsequent charge separation. Likewise, careful analysis of metal nanoparticle systems is needed, for example, to minimize contaminant background signal in trace analysis applications or to maximize emission stability in biological labeling applications. In this work, careful consideration is given to the structural properties of both *single* metal nanoparticle aggregates (Chapters 3 and 4) and *single* semiconductor nanoparticles (Chapter 5) with the goal of identifying crucial properties and characteristics that should be optimized for a variety of practical applications.

This introductory section serves to briefly introduce the electronic and optical

properties of both metal nanoparticle aggregates and semiconductor nanoparticles. The difference between bulk material electronic properties and those of the corresponding nanoparticles is briefly discussed for both metal and semiconductor systems. Then, an introduction to metal nanoparticle aggregates is approached in a bottom-up manner where the electronic properties of the nanoparticle building blocks are established before discussing their interaction in an aggregate system which gives rise to surface-enhanced optical processes. A brief discussion of small clusters of only a few metal atoms follows and is crucial to understanding the intrinsic optical response of silver nanoparticle aggregates presented in Chapters 3 and 4. Next, a brief discussion of the structural and electronic properties of colloidal semiconductor nanoparticles is given. The introduction is then concluded with overviews of both the unique properties of single quantum emitters and the nonlinear optical response of materials.

Following the introduction, Chapter 2 describes the particular material systems and experimental methods used in this work. Chapters 3 and 4 present careful analysis of the intrinsic linear and nonlinear emission from silver nanoparticle aggregate films, and conjectures a physical picture of emissive silver clusters interacting with the localized plasmon modes of the nanostructure. Chapter 5 comprehensively studies the role of nanoparticle morphology for semiconductor heterostructure nanoparticles that act as model light-harvesting systems. In the final chapter, the work is quickly summarized and then concluded with a few thoughts on future research directions.

1.1 Electronic properties of nanoparticles: from clusters to nanoparticles

In general, "cluster science" refers to the study of material systems with physical dimensions which are comparable to those of the constituent atoms [2]. At these length scales, which range from 10 Å to over 100 nm, the material systems are discrete particles consisting of as few as 2 atoms in molecular clusters to more than 10^7 atoms in larger nanoparticles [13]. In this size regime, material systems are in an electronic configuration which bridges discrete molecular-like electronic states and the bulk electronic bands which are associated with the material's familiar macroscopic

properties [10, 13].

Figure 1.1 conceptually depicts the bottom-up construction of a bulk material's electronic properties starting with a single atom [2, 13, 15, 16]. For both metals and semiconductors, the fundamental building blocks of the material are the constituent atoms in the primitive cells of the crystalline lattice [10]. In general, the primitive cell may contain multiple atoms, but for the sake of clarity, the discussion here focuses on single-atom materials. As two atoms are brought together to form a dimer, the molecular states become an energetically split symmetric and antisymmetric combination of the individual atomic states, and the highest occupied and lowest unoccupied atomic orbitals become the highest occupied and the lowest unoccupied molecular orbitals (HOMO and LUMO, respectively). In an identical manner, further splitting occurs in larger clusters with more atoms. Eventually in clusters with a relatively large number of atoms, the splitting becomes negligible (i.e., less than the thermal energy), and the set of closely separated states centered around the original atomic energy level can be considered a quasicontinuous band [2, 13].

The electronic configuration of the constituent isolated atoms is intricately linked

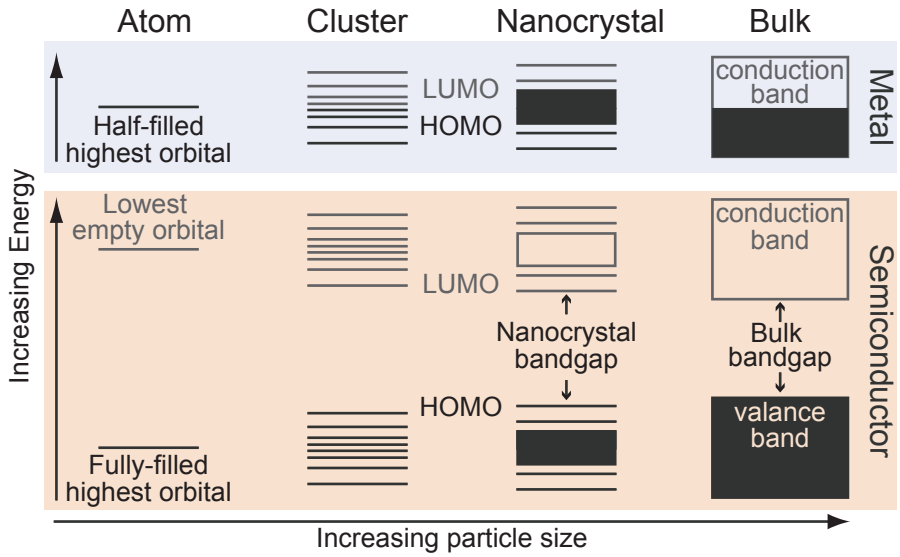

Figure 1.1. The evolution of the electronic energy levels of metals and semiconductors as particle size increases from individual atoms to the bulk [2, 13, 15].

to the electronic configuration of the corresponding cluster or bulk material. A band of states forms for each electronic orbital of the single atom that makes up the constituent building blocks [10]. While the energetic centers of the bands are determined by the atomic orbitals, the number of states within the bands are determined by the total number of atoms in the system: each atom "contributes" a single state to the band which can contain two electrons of opposite spin. Therefore, an atomic orbital which contains and even number of valence electrons leads to a filled electronic band in the bulk whereas an odd number of valence electrons leads to a half-filled electronic band. Therein lies the fundamental difference between semiconductors and metals [10]. In metals, where the highest energy individual atomic orbital is filled with an odd number of valence electrons, the highest energy electronic band is only half-filled. This half-filled band – called the *conduction band* – supports electrical conduction due to the nearby, higher energy, vacant states within the top half of the band. In contrast, the highest occupied orbital in semiconductor atoms is filled with an even number of valence electrons leading to complete filling of the top-most band – called the *valence band*. Thereby, the closest vacant state for semiconductor electrons lies in the next higher band – also referred to as the conduction band – and thus interband excitation of the electrons is required for significant electrical conductivity.

The difference in occupancy of the highest-filled band between semiconductors and metals has important consequences for their corresponding nanoparticle systems. The amount of splitting between the states in a cluster is not equal [13,15]; the states in the middle of the quasiband are less separated than those at the edges. Thus, the position of the highest occupied electronic state within this quasiband plays an important role in determining the critical particle size at which a material makes the molecular-to-bulk transition. For metals, where the highest occupied electronic level lies in the middle of the quasiband, nanoparticles assume bulk-like properties at smaller sizes than their semiconductor counterparts in which the highest occupied state lies at the edge of the quasiband. So, while metal clusters quickly become conducting with increasing size, semiconductor nanoparticles preserve molecular-like behavior of their highest occupied electronic states to notably larger particle dimensions [13]. As a

consequence, the task of deliberately tuning the *intrinsic electronic states* through fabrication or synthesis is much easier for nanoparticles derived from semiconductor materials as compared to metals [14].

This work deals with metal and semiconductor nanoscale systems on length scales which span both sides of the molecular-to-bulk transition. For the sake of clarity, the term "cluster" is explicitly used for material systems where it is assumed that discrete energy states exist and energy bands are not present at the relevant temperature. Otherwise, the less-specific term "nanoparticle" is used for material systems where discrete states are not assumed.

1.2 Metal nanoparticles and rough films

A large portion of this work studies the intrinsic optical response of semi-continuous silver films. The physical structure of these metal films (see Sections 1.2.4 and 2.4.1) consists of an aggregation of metal clusters and nanoparticles ranging from two-atom dimers to particles several-hundred nanometers in size. Illumination with visible or infrared radiation excites each of these constituent building blocks and the complex set of interactions within the film geometry give rise to an elaborate optical response [2, 7]. Here, a bottom-up approach is used to first describe the optical and electronic properties of the individual building blocks, and then to establish a qualitative understanding of how their interactions in aggregate structures can give rise to the rich optical properties of a simple metal film.

The optical response of metallic nanoparticles and clusters is extraordinarily sensitive to particle scale over a wide range of sizes [2, 15, 17–26]. In addition to the aforementioned transition from molecular-like electronic states to bulk-like bands at small length scales, the kinetics and electrodynamic response of the nearly-free electrons in the conduction band exhibit their own unique size effects. Figure 1.2 summarizes the three main size categories of metal clusters and nanoparticles and the corresponding size effects [2]. The first category contains small metal clusters with discrete, molecular-like electronic states. The electronic states become a quasicontinuous band for metal nanoparticles exceeding 2 nm in diameter. These small

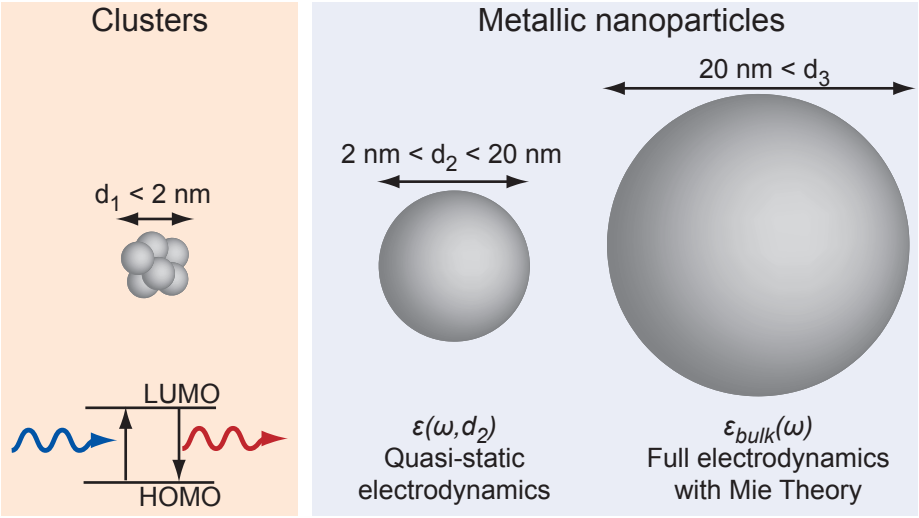

Figure 1.2. Size categories for metal nanoparticles. The assumptions and applicable theories used to understand the optical properties of a metal nanoparticle depend upon its size [2]. Small, few-atom metallic clusters have discrete electronic states. The size dependence for larger clusters with conduction electrons comes from either a size-dependent dielectric function, $\epsilon(\omega, d)$, or electrodynamic effects understandable with Mie theory.

clusters are best treated as molecules with discrete optical transitions between the HOMO and LUMO. The structural and electronic properties of these clusters are briefly discussed in Section 1.3.

This section deals with the two categories of metal nanoparticles where conduction electrons dominate the optical response. In these particles, discrete excitation of electrons between states gives way to collective excitation of the conduction electrons. The optical response of the nearly-free electrons can be adequately understood using classical electrodynamics where the quantum mechanical details of the electron kinetics are embedded into the dielectric constant of the nanoparticle. In this context, two important size regimes exists [2, 18, 19, 27]. The excited conduction electrons in metal nanoparticles with diameters between 2 nm and 20 nm are strongly affected by the nanoparticle size through effects such as scattering with the surface. These effects – termed *intrinsic size effects* – are essentially a deviation of the conduction electrons from their behavior in the bulk and are encompassed by a size-dependent

dielectric function, $\epsilon(\omega, d)$. These intrinsic size effects are the primary origin of size and shape dependence in this smaller class of metal nanoparticles.

Beyond 20 nm, the influence of the nanoparticle's surface is greatly diminished, and the motion of the electrons mimic their motion in bulk [2, 18, 19, 27]. Thus, the dielectric function for these nanoparticles assumes the morphology-independent bulk value, $\epsilon_{\text{bulk}}(\omega)$. Yet, nanoparticle systems made of, for example, gold or silver, still exhibit size-dependent optical properties at visible frequencies [2, 18, 19, 27]. In this case, the size-dependence is no longer a quantum-mechanical effect as in the intrinsic size effects, but a purely electrodynamic effect originating from the inability of the optical excitation to uniformly polarize conduction electrons in the metal nanoparticle. In brief, for the larger class of metal nanoparticles, the quasistatic approximation [28] breaks down, and the excitation of higher-order, nondipolar modes accounts for the observed size effects. Since the size effects do not reflect the intrinsic configuration of the nanoparticle, they are referred to as *extrinsic size effects*, and are fully understood for a spherical particle using Mie theory [2, 18, 19, 23].

Although a complete description of the optical response of metal nanoparticles requires simultaneous inclusion of both intrinsic and extrinsic size effects, a rich qualitative understanding that circumvents these complex issues can be obtained by considering a metal sphere, $\sim$20 nm in size, which can be adequately treated with both the bulk-dielectric constant as well as the quasistatic approximation of electrodynamics [28]. In the following sections, the bulk dielectric constant of the free electrons in a metal is described with the Drude-Sommerfeld-Lorentz model and then used to understand the optical resonance of the nanoparticle's conduction electrons within the quasistatic approximation. Modifications to the resonance due to the intrinsic and extrinsic size effects as well as particle shape are qualitatively discussed before addressing how such particles interact in aggregated configurations.

1.2.1 Drude response of a bulk metal

The dielectric function of a material, $\epsilon(\omega)$, reflects the polarization of the material that is induced in an applied electric field oscillating at a frequency, ω [10, 28]. As a macroscopic parameter, the dielectric function reflects an average over microscopic

quantities. In general a microscopic species such as a bond or free electron will be distorted under an external field and create a microscopic dipole moment, $\boldsymbol{p}$. The size of the induced dipole moment is typically linear with respect to the strength of the electric field, $\boldsymbol{p} = \alpha \boldsymbol{E}$, where α – termed the microscopic polarizability – reflects the extent of the induced distortion. The contribution of a polarizable species to a material's macroscopic polarization (i.e., the dipole moment density) is simply the product of its microscopic polarizability and its macroscopic density. In the case of noble metals such as silver and gold and their corresponding nanoparticles [2,10], the free electrons dominate the optical response at visible and infrared frequencies, so the macroscopic polarization is simply $\boldsymbol{P} = n\alpha \boldsymbol{E}$ where α is the induced polarization of a single conduction electron, and n is the density of conduction electrons. The expression for the induced polarization can then be used with relevant electrostatic definitions to obtain an expression for the dielectric function:

$$\epsilon = 1 + \frac{n\alpha}{\epsilon_0}. \tag{1.1}$$

The Drude-Sommerfeld-Lorentz model is a simple classical model used to describe the polarizability of a nearly-free conduction electron [2, 28, 29]. Under this model, the electrons are assumed to be unbound. Their motion is assumed to be restrained with a damping constant, Γ, which describes a force proportional but in opposition to the velocity of the electrons. The induced dipole moment of a single electron, $\boldsymbol{p}$ can be derived by solving the simple equation of motion of the electron with the phenomenological damping force and a harmonic driving force from the electric field, $\boldsymbol{E} = \boldsymbol{E_0} e^{-i\omega t}$:

$$m_e \frac{\partial^2 \boldsymbol{r}}{\partial t^2} + m_e \Gamma \frac{\partial \boldsymbol{r}}{\partial t} = e\boldsymbol{E_0} e^{-i\omega t}, \tag{1.2}$$

where m_e is the mass of the electron (note that the effective mass of the electron can be used to describe coupling to the ion cores), and e is the charge of the electron. The derived single electron dipole is then easily related back to the polarizability through

the relation, $\boldsymbol{p} = \alpha \boldsymbol{E}$, which can subsequently be used to express the frequency dependent dielectric function of free conduction electrons in a metal:

$$\epsilon(\omega) = 1 - \frac{\omega_p^2}{\omega^2 + \Gamma^2} + i\frac{\omega_p^2 \Gamma}{\omega(\omega^2 + \Gamma^2)}, \tag{1.3}$$

where $\omega_p = (ne^2/\epsilon_0 m_e)^{1/2}$ is the Drude plasma frequency.

The Drude-Sommerfeld-Lorentz model only considers contributions to the dielectric function from *intraband* excitations of the free-electrons in the conduction band. However, at high enough energies, *interband* transitions from lower-lying valence bands in the metal also contribute to the dielectric function [2]. For gold and silver, these contributions must be taken into account for energies larger than 2.4 eV and 3.8 eV, respectively. Despite this shortcoming, the bulk dielectric function derived from the Drude model has proven to be a good starting point for describing the optical response of bulk metals and larger nanoparticles [2, 18, 19, 30].

1.2.2 A single metal nanoparticle

For a spherical metal nanoparticle with a radius of approximately $R = 10$ nm, both the quasistatic approximation of electrodynamics and the bulk dielectric constant of the metal can be employed to intuitively understand its optical response [2, 28]. This approach assumes that the light only interacts with the free electrons in the conduction band as described by the Drude-Sommerfeld-Lorentz model. The positively charged nuclei of the nanoparticle are assumed to be stationary thus only allowing the electrons to move in response to the electric field. Finally, the quasistatic approximation neglects retardation effects and spatial variations of the electric field strength by assuming that the particle is uniformly polarized by the incident light field. In this manner, the electrostatic response of a polarizable sphere can be used to understand the optical excitation of a metal nanoparticle.

When exposed to an external electric field, $\boldsymbol{E} = \boldsymbol{E_0} e^{-i\omega t}$, the internal electric field of a polarizable sphere with the dielectric function $\epsilon(\omega)$ is

$$\boldsymbol{E_i} = \boldsymbol{E_0} \frac{3\epsilon_m}{\epsilon(\omega) + 2\epsilon_m} e^{-i\omega t}, \tag{1.4}$$

where ϵ_m is the dielectric function of the surrounding media of the sphere. Treating the sphere as a single polarizable entity as discussed above, this response can be expressed in terms of the polarizability, $\alpha(\omega)$ of the sphere:

$$\alpha(\omega) = 4\pi\epsilon_0 R^3 \frac{\epsilon(\omega) - \epsilon_m}{\epsilon(\omega) + 2\epsilon_m}. \tag{1.5}$$

From Equation 1.5, the polarizability of a particle is maximized when $|\epsilon(\omega) + 2\epsilon_m|$ is minimized. In the case of the conduction electrons in metal, the dielectric function can be negative leading to a resonance in the polarization when $Re(\epsilon(\omega)) = -Re(\epsilon_m)$.

At the resonance condition for a metal nanoparticle, the conduction electrons collectively oscillate with respect to the stationary positive ion cores in phase with the excitation field as shown schematically in Figure 1.3. Since the displacement of the electrons results in a net polarization of the surface of the metal nanoparticle, this resonance is interpreted as the *localized surface plasmon resonance* (LSPR) of the sphere [2, 18, 19, 27] and gives rise to their phenomenal optical properties such as enhanced optical extinction [2, 4, 17, 18, 21–23, 31–34], nonlinear scattering [35–41], and linear and nonlinear luminescence [42–46]. Additionally, excitation of the LSPR effectively concentrates the electric fields to the surface of the particles creating small regions where light-matter interactions can be enhanced by the presence of the

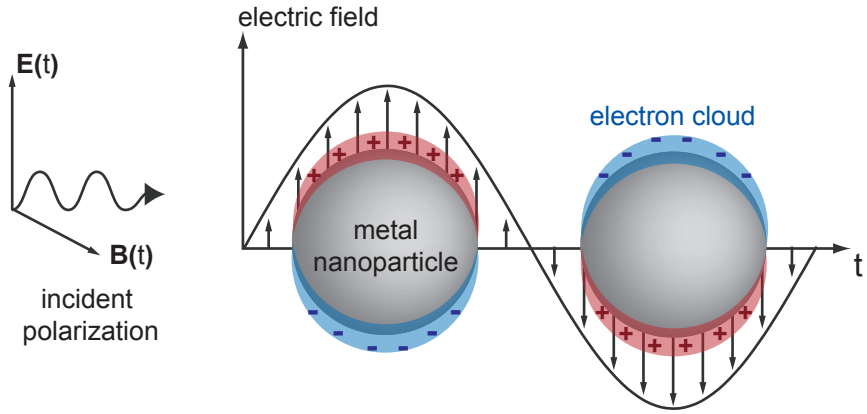

Figure 1.3. The dipolar localized surface plasmon excitation in a metal sphere in the quasistatic approximation.

nanoparticle. For the case of the single sphere, detailed calculations have shown that the enhanced electric field can be up to 10 times larger than the incident external field [47].

The simplicity in this approach is immediately evident from the lack of explicit particle size-dependence on the resonance conditions as observed in optical spectroscopy of metal nanoparticle LSPRs [4,18,22,33,34,48–52]. The observed size dependence is attributed to the previously mentioned intrinsic and extrinsic size effects. For noble metal nanoparticles, in the size regime where intrinsic size effects dominate, two general trends are observed with decreasing particle diameter. First, the plasmon resonance shifts to lower energies as the particle gets smaller [21]. Second, the width of the resonance increases reflecting a decrease in the quality factor of the plasmon mode [18]. The increased damping of the conduction electrons is attributed to stronger interactions with and scattering from the nanoparticle surface [2, 40], increased localization of the electrons in the metal [2], "spill-over" of the conduction electrons into the surrounding medium [48], reduced nearest-neighbor distances in smaller clusters [2], and most recently increased influence of lower conductivity electrons at the surface [21].

For the larger nanoparticles where the dielectric function assumes the value of the bulk material, the LSPR shifts to lower energies with increasing particle size [27], while the resonance width increases [18,31,32]. The size dependence of the LSPR for these particles originates from retardation effects where the oscillating electric field cannot polarize the particle uniformly (i.e., the quasi-static approximation breaks down). Consequently higher-order multipoles of the particle become excited leading to both the shift in the resonance position as well as the decrease in its quality factor [2, 18, 27]. Mie theory accurately encompasses the complete electrodynamic treatment of LSPRs and the observed size dependence but is limited to spherical morphologies [2].

Both solution based synthesis and complex fabrication methods such as electron beam lithography make a variety of shapes such as ellipsoids [52], rods [32,37,45,53], prisms [31, 54, 55], bowtie antennas [56], cubes [51, 52], stars [57], crescents [58], and

circular disks [52] realizable metal nanoparticle structures. Exact theoretical treatment of LSPRs in anisotropic metal nanoparticles is approached with Gans theory which extends Mie theory to cylinders and ellipsoids [2, 19, 27]. For more complex shapes, however, numerical calculation is required [17]. Figure 1.4 summarizes the primary shape effects for LSPRs in metal nanoparticles. In general, the reduced symmetry of a nanoparticle from a spherical shape increases the number of observed LSPRs, changes their quality factors, and modifies the spatial distribution of the local electric field. A qualitative understanding can be obtained by comparing an ellipsoid to a sphere [2]. While the sphere is characterized by just its radius, an ellipsoid is characterized by its size with respect to three orthogonal principal axes. Each principal axis results in a corresponding LSPR where the energetic splitting between any two modes increases with increasing aspect ratio of their principal axes [18, 52]. Consequently LSPRs are only energetically degenerate if two or more principal axes have the same size [2, 19, 27]. Furthermore, with the decreased symmetry, a specific excitation energy *and* polarization orientation are required to excite the individual nondegenerate LSPRs of the anisotropic particle [57, 59, 60]. Additionally, the quality

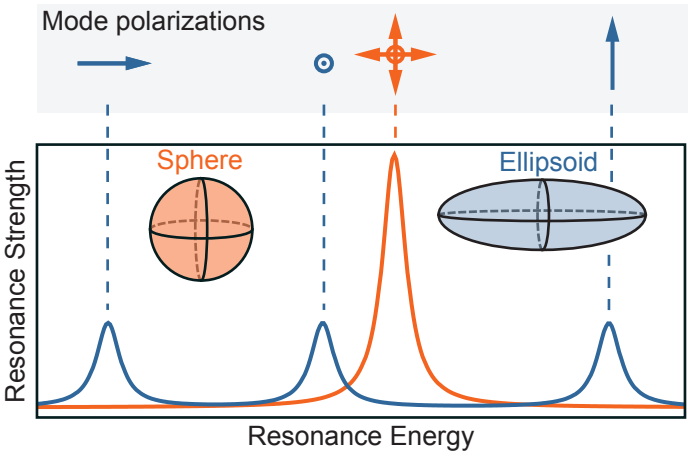

Figure 1.4. The plasmon resonance of an anisotropic ellipsoid compared to an isotropic sphere. The three different principal axes of an ellipsoid act to lift the degeneracy of the spherical plasmonic resonance. Each resonance energy and polarization for the ellipsoid corresponds to the size and orientation, respectively, of the corresponding principal axes [2, 19, 27].

factors of the LSPRs have been observed to increase for rods compared to similar sized spheres due to decreased interactions with the nanoparticle surface [32]. Finally and perhaps most importantly, careful control of the shape allows for the tailoring of the spatial distribution of the electric fields of the plasmon excitation at the nanoparticle surface [3, 17, 57]. Introduction of sharp corners and tips on the particle concentrate the electric field through the *antenna effect* leading to areas of even larger field enhancements at the apex or junctions of these features. Such a rich dependence of the optical properties of metallic nanoparticles on shapes makes them ideal candidates for customized applications as well as for studying fundamental structure-property relationships on the nanoscale.

It is worth noting that the LSPRs of metal nanoparticles can also serve as sensitive environmental sensors. In addition to their dependence on size and shape, the LSPRs of metal nanoparticles are also highly sensitive to the surrounding medium [20]. The origin of the sensitivity is found in the resonance condition of Equation 1.5 that depends on the dielectric constant of the surrounding environment [61]. Generally, as the dielectric constant increases, the LSPR modes shift to lower energies. Thus metal nanoparticles are also great candidates for sensitive detectors of local dielectric constants especially with regard to biosensing applications [4].

1.2.3 Interacting metal nanoparticles

With optical properties that are tunable by both size and shape, individual metallic nanoparticles provide an array of functionality that is widely applicable to techniques such a optical labeling and environmental sensing. Increased functionality and complexity is found when two or more of these plasmonic particles reside in spatial proximity which allows for interparticle interactions as in a semicontinuous metal film [7]. The LSPRs of two or more interacting particles can lead to strongly localized electric fields within close proximity of the multiparticle system. Consequently, under appropriate excitation conditions and geometric arrangements of the metal nanoparticles, the LSPRs of multiparticle systems can be used to significantly enhance light-matter interactions such as Raman scattering, coherent nonlinear scattering, and

material luminescence [7].

Figure 1.5 schematically illustrates the LSPR modes of the simplest multiparticle system: two interacting metal spheres separated by a distance, d. Two distinct LSPRs exist for this system depending on the linear polarization orientation of the excitation with respect to the dimer axis. For transverse polarization where the electric field is perpendicular to the dimer axis, the LSPR of the dimers is reminiscent of the mode of just a single sphere with enhanced electric fields occurring at the top and bottom (with respect to the figure) surfaces of the two spheres . The situation is much more exciting for the case of longitudinally polarized excitation where the electric field is now parallel to the dimer axis. Again, both particles are polarized in the same direction with enhanced fields at the respective surfaces. In the confined

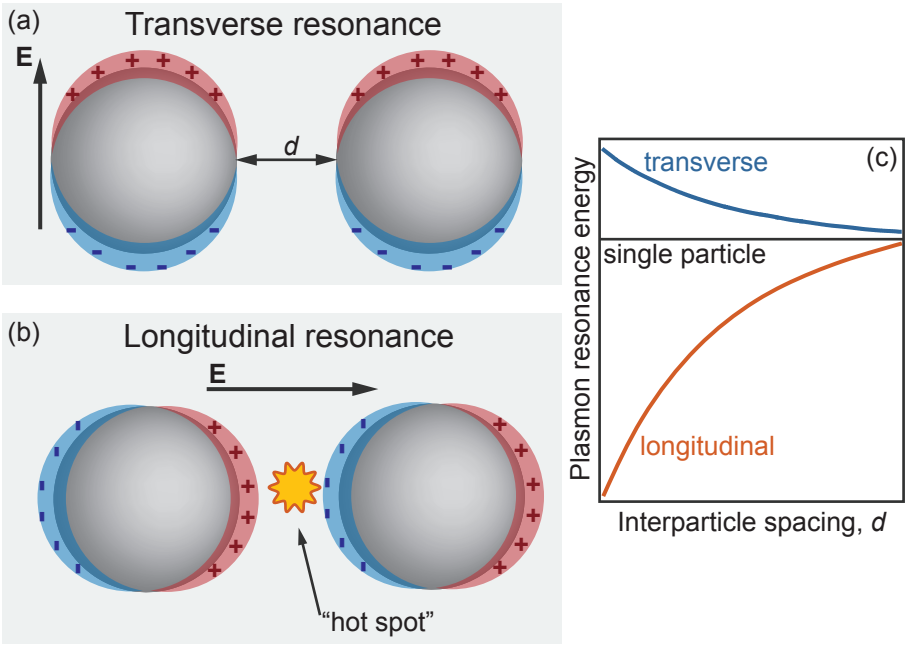

Figure 1.5. The dipolar localized surface plasmon excitations of two metal spheres in the quasistatic approximation. (a) The transverse mode is very similar to an isolated metal sphere but with a net coulombic repulsion between the two nanoparticles. (b) The longitudinal mode leads to large enhancement of the electric field and a net coulombic attraction between the two particles. (c) The separation distance of the two particles affects the resonant frequency in an opposite manner for transverse and longitudinal modes which merge to the single particle resonance at large distances [1].

space between the two particles, however, a significantly more substantial electric field is created due to the opposite charge states of the opposing surfaces that form a capacitor-like configuration. Within this confined area, the electric field can be enhanced by a factor exceeding 10^3 over the incident excitation field depending upon the interparticle distance [47]. The interparticle and single particle regions that give rise to such large enhancement of the incident electric field are often referred to as *hot spots*, and within these regions light-matter interactions can be significantly enhanced.

The interparticle coupling in the dimers and more complex systems falls into two main categories depending on the interparticle distance, d. For separations less than 10 nm at optical excitations, the interactions are dominated by near-field effects between two dipoles. In this case, the localization in the interparticle hot spot arises because the particles excite plasmons in the neighboring particles rather than re-radiating to the far-field [1, 62, 63]. At larger distances outside the near-field coupling regime, the particles interact via their scattered, dipolar far-field radiation [1, 64, 65]. The dependence on interparticle distance can be thoroughly understood with Mie theory for spherical particles or by numerical calculations for more complex shapes [1]. Both theory [1] and experiment [62, 63, 66] reveal that distance affects the transverse and longitudinal modes differently, which is attributed to opposite effects on the electron damping between the two modes [1]. For the transverse mode, the coulombic interaction between the charge distribution of the particles leads to a stronger damping force causing the LSPR to shift to higher energies compared to the single particle LSPR. In contrast, the damping force is reduced for the longitudinal LSPR of the dimer which shifts the resonance energy lower with respect to the single particle [1] as shown in Figure 1.5(c).

With improved fabrication techniques, especially in regard to lithography, a large variety of interacting nanoparticle arrays have been created. These include arrays of disks [67,68], arrays of bow-ties [56], circular arrays of particles of varying shapes [69], and complex plasmon focusing systems [70–72]. The aim of these systems is two-fold. The first goal is fundamental and aims to gain more insight and understanding of the complex resonances that can be created with these multiparticle systems [73]. The

second goal is more practical and aims at fabricating large arrays of well-defined hot spots for performing surface-enhanced spectroscopy [4]. While controlled fabrication of hot spots has the advantage of creating structures with well-defined resonances and electric field enhancements, the density of hot spots is typically quite low. In contrast to such elegant structures, however, semi-continuous metal films created by simply disrupting the deposition process create, essentially, a random array of such metal nanoparticles of various sizes resulting in both a large concentration and variety of optical hot spots.

1.2.4 Nanoparticle aggregates and random metal composites

Semicontinuous metal films are unique systems for investigating complex LSPRs as well as insulator-to-metal transitions. The conductivity of a metal film on top of an insulating substrate (i.e., glass) during deposition by sputtering or thermal evaporation develops in a semibinary manner [74]. The 2D density of the metal on the substrate can be defined through the metal filling factor. Below what is referred to as the percolation threshold, the metal film does not exhibit significant in-plane conductivity as it only consists of isolated metal islands. As the filling factor is increased, the percolation threshold is crossed, and in-plane electrical conductivity is achieved as electrons are able to move across the film via a percolation channel [74]. In addition to the complex insulating-to-conducting transition, semicontinuous films near the percolation threshold exhibit unique optical properties due to the LSPRs of their irregular shaped metal islands [7, 75] constructed of a complex array of interacting metal nanoparticles.

In fact, enhanced optical responses in semicontinuous or rough noble metal films with nanoscale structure have been actively studied since the late 1960s [76]. Primarily before significant advances in microscopy enabled the high resolution studies, enhanced scattering [76], interband luminescence [77], and nonlinear scattering [75, 78, 79] were observed from metal films with nanoscale roughness. More advanced experimental techniques, especially near-field microscopy, revealed that the enhanced optical response unequivocally arises from spatially inhomogeneous, highly localized

electric fields on the film [65, 80–87]. Similar in concept to the metal nanoparticle dimer structure, these positions of maximal field enhancement are commonly referred to as *hot spots* [7]. The hot spots observed in the near-field have also been observed in far-field microscopy studies as diffraction limited emission of enhanced linear scattering [86], nonlinear scattering such as second-harmonic generation [75, 88], and nonlinear luminescence [89].

In Figure 1.6, an image from a scanning electron microscope (SEM) of a representative silver film near the percolation threshold is shown alongside the common model invoked to theoretically study the LSPRs of the rough metal films and extended nanoparticle aggregates. In the model, the 3D space that defines the film is divided into a discrete grid of cells, which are randomly populated with either a metal or dielectric material based upon a chosen filling factor. Each metal cell is then treated as an independent dipole that is described by a dielectric function, which is typically extracted from experimentally determined values. The LSPRs are then calculated by numerically modeling the near-field dipole-dipole interactions of the metal cells

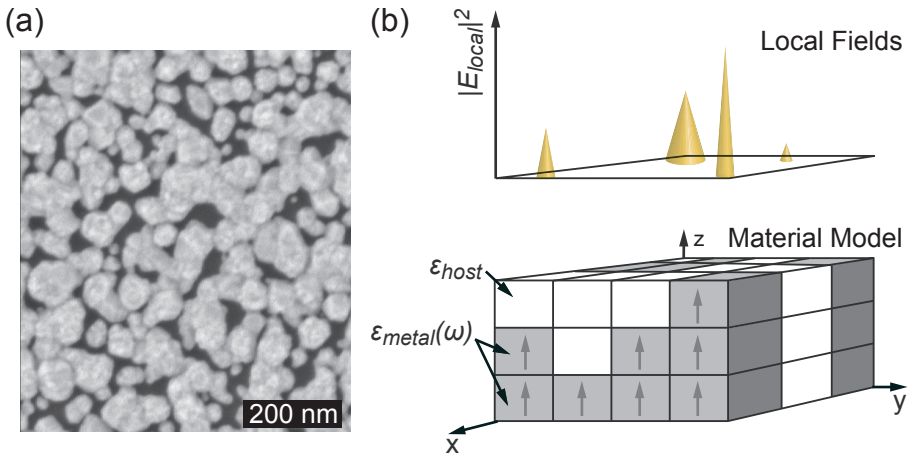

Figure 1.6. A typical example of metal aggregate film and a schematic of the model invoked to understand its optical response. (a) A SEM image of a typical semicontinuous metal film consisting of large nanoparticle aggregates used in this study. (b) The typical model used to study metal aggregates fills a divided space randomly with polarizable metal nanoparticles. By numerically calculating the interactions of the metal cells, highly localized field distributions are obtained [7, 90–93] in agreement with experimental observations [65, 80–87].

[7, 91–93]. From the numerical analysis, information on the spatial inhomogeneity of the modes [7, 91], localization length and strength of the hot spots [91], and local polarization and coherence [92] can be acquired. This theoretical approach has been widely successful in both predicting and describing the strong localization of LSPRs observed in rough metal films. For example, rough metal films are known to form fractal-like structures that have a notable degree of self-similarity in terms of either shape or roughness on length scales relevant to visible optical excitation [7]. With experimental techniques, discerning the role of self-similarity is difficult [94]. The theoretical modeling, however, clearly identifies that within the size range in which the system is self-similar, significant nearest-neighbor interparticle interactions are guaranteed. This results both in strong localization of LSPRs as well a set of LSPR energies spanning a broad spectral range [7].

The enhancement factors anticipated from rough metal films [7] are comparable to the best enhancement factors predicted from metal nanoparticle dimer systems [47]. However, the majority of surface-enhanced optical studies occurs on rough metal films. The relatively easy production techniques such as thermal evaporation as compared to electron beam lithography, inherent strongly localized surface plasmon resonances which can be excited over a broad spectral range, and the typically large density of hot spots, make semicontinuous or rough metal films ideal platforms for surface-enhanced microscopy.

1.2.5 Surface-enhanced optical processes

Single metal nanoparticles and interacting multiparticle systems such as dimers and rough metal films all generate some form of enhanced electric field due to their respective LSPRs. Within these regions termed hot spots, the electric field can be over 10^3 times higher than the incident excitation fields [7,47]. As it has been alluded to in this text and now schematically depicted in Figure 1.7, interaction of matter with the optical electric field is significantly enhanced within the confines of the hot spots [7]. For the sake of this work, the enhanced optical processes within the hot spots are classified into two categories. The first category contains processes which are

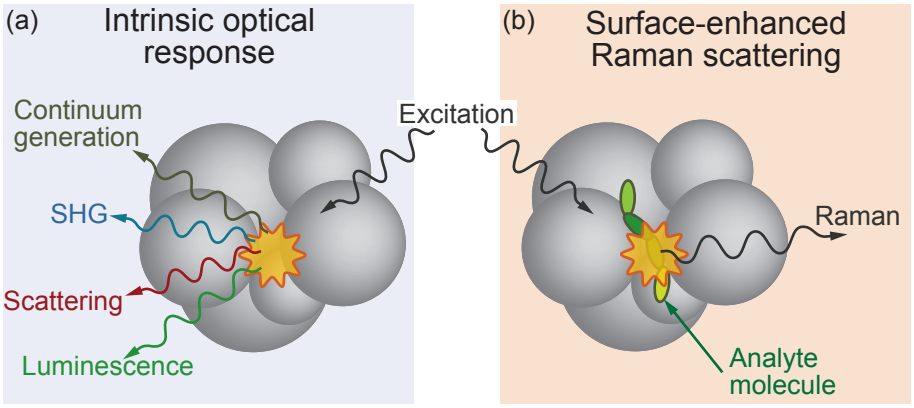

Figure 1.7. Enhanced light-matter interactions within the hot spots of metal aggregates or rough metal films are divided into two categories. (a) The intrinsic optical response from the metal nanoparticles such as linear scattering, luminescence, second-harmonic generation, or continuum generation can be strongly confined within the hot spot. (b) Light-matter interaction with an analyte material can be greatly enhanced within the hot spot as is the case in surface-enhanced Raman scattering [7, 9, 95].

intrinsic to the hot spot itself. Such processes include linear and nonlinear scattering and luminescence directly observed from the hot spot. The second category includes enhanced processes that require the presence of an analyte material within the hot spot such as Raman scattering or fluorescence.

The most well-known process which falls into this second category is surface-enhanced Raman scattering (SERS) [9, 96, 97]. Typically, Raman scattering, which is the inelastic scattering of light with vibrational modes of a system, is incredibly weak with an interaction cross-section up to 13 orders of magnitude less than fluorescence [9, 96, 97]. However, by simply placing a *single* molecule such as a conjugated polymer within the hot spot, Raman scattering from the single molecule can be observed at similar signal levels as the molecular fluorescence [98]. The Raman spectrum of a molecule is unique to its chemical structure, and enabling such molecular fingerprinting on the level of an individual molecule makes SERS perhaps the ultimate spectroscopic tool to study material systems. Accordingly SERS provides the primary motivation to study the surface-enhancement process and hot spots in overwhelming detail as was done in this work.

While the theoretical fundamentals of the LSPRs are well understood in the context of interacting metal nanoparticles, the understanding of the dynamics and chemical nature of the hot spots remains incomplete, and a number of effects in SERS, especially at the single molecule level, remain a mystery [99, 100]. SERS spectra are often accompanied by both a broad continuum background [60, 101–104] and a contamination Raman signal not associated with an analyte molecule [105]. Singe molecule SERS spectra have also been observed to significantly fluctuate in intensity [106]. And finally, many reports claim enhancement factors for the Raman signal which exceed what would be expected from the predicted electric field enhancement [107]. Thus, an additional enhancement mechanism termed *chemical enhancement* has been proposed involving the injection of excited electrons into analyte molecules which augments the *electrodynamic enhancement* effect which has been discussed here [100, 107]. Much effort has been invested in understanding these mysterious effects, but still a consensus has not been reached. The studies on the silver films and nanoparticles presented in this work elucidate important details of the intrinsic dynamic, geometric and chemical nature of the hot spots themselves. The studies provide a new set of insights into the inner workings of hot spots on a silver film that are immediately applicable to several of the persisting SERS mysteries.

1.3 Small metal clusters

The studies of semicontinuous metal films presented in this work indicate that emissive metal clusters exist with and can be photo-generated from the larger metal nanoparticles in the film as reported for similar systems [108–111]. Although with respect to SERS they seem to be a parasitic source of background emission (Chapter 4) and reduced enhancement [112], very small clusters of silver or gold atoms with sizes less than 2 nm are emerging as popular material systems for a wide variety of reasons. As discussed above, metal clusters at this length scale are primarily void of band formation and rather consist of discrete energy states (see Figures 1.1 and 1.2). From a fundamental scientific point of view, small metal clusters provide yet another opportunity to create designer systems of ultrasmall *artificial atoms* with

properties that are exceptionally sensitive to cluster size and geometry [113]. Then on more practical levels, metal clusters also show promise as highly effective catalysts for chemical reactions [114–118], or as nontoxic biolabels with small hydrodynamic radii [25, 119, 120], and can even enhance Raman scattering (without LSPRs) [121]. While these small systems exhibit a number of promising properties, they remain plagued by complex fabrication techniques, and lack a complete understanding of their structural and electronic properties.

1.3.1 Structural properties

The first fabrication and optical experimental studies of small silver clusters began with the deposition by mass-selective sputtering of silver and other metal dimers and trimers in rare-gas matrices [122,123]. Further improvement on this process involving the focusing of the ion beam during the sputtering process extended the obtainable cluster sizes to over thousands of atoms [113, 115, 116, 118, 124–127]. From these studies, *magic numbers* of atoms were identified for small clusters which resulted in geometrically and electronically stable clusters [113]. Recently, more novel techniques of generating silver clusters have also been reported by decomposing silver complexes contained in a polymer or silica matrix to form small silver clusters [120, 128–130]. Finally, photo-illumination of silver-oxide films has been conjectured to produce luminescent silver clusters [108–111]; however, a complete physical description of the resulting clusters has yet to be obtained.

Direct structural characterization of both gold and metal clusters has been limited. Several studies reported that the mass from the deposition process correlated with the measured luminescence from the clusters [122,123]. Recently, infrared vibrational spectroscopy was combined with accurate quantum chemical calculations to provide detailed insight into gold clusters consisting of less than 10 atoms [117]. Structural characterization of clusters beyond optical studies has required the state-of-the art technique of scanning transmission electron microscopy to clearly elucidate the structural configurations of a gold cluster of 309 atoms on glass [127] and a gold cluster consisting of 5 atoms embedded in a graphite matrix [131]. Thus at this point, it is

hard to draw confident and meaningful conclusions on the exact structure of these clusters aside from perhaps just the number of atoms in the cluster, especially since theoretical treatment predicts a wide range of possible structural configurations [132].

1.3.2 Electronic properties

Suffering from the same instabilities and fabrication limitations as the structural studies, investigations of the electronic properties of metal clusters remain generally inconclusive with only one exception: the electronic properties of the clusters are exceptionally sensitive to the their structural arrangement. Ultraviolet light absorption and visible light emission from silver and other coinage metal clusters were first observed in the size-selected aggregations within a rare-gas matrix [122–126, 133]. These studies established that small silver clusters less than 1 nm or 2 nm in size show substantial visible molecular-like luminescence, which is strongly dependent on the physical size and arrangement of the clusters [122, 134]. Indeed, the seminal absorption and emission studies are the key argument in the claim that observed dynamic luminescence from silver oxide films arises from the photo-reduction of the silver-oxide layers into emissive silver clusters [108–111, 135–138]. Drastic intensity fluctuations and spectral dynamics were observed in these photo-generated silver clusters and are attributed to the dynamic changes to the structure and electronic state of the emissive cluster [108, 110, 137]. While in general, the quantum yield of luminescence (the emission efficiency) decreases significantly with increasing cluster size as observed directly for gold [119], silver nanoparticle luminescence can still be seen from larger *polycrystalline* particles with domains that only consist of a small number of atoms [139]. Most recently, several studies have aimed to stabilize single cluster emission dynamics with surface passivation of the silver clusters [134,140,141].

In addition to the wide array of optical studies, the unique, structure-specific electronic properties of both metal and gold clusters arise in their exciting catalytic properties [114]. For gold, the catalytic properties of the clusters at least partly depend upon their geometric arrangement [117]. For example, it has been shown that gold clusters with less than 11 atoms are either inert if the clusters consist of

an even amount of atoms, or will react with oxygen to form gold oxide if the cluster consists of an odd number of atoms [115].

The sensitivity of the electronic properties on a cluster's physical arrangement has also been corroborated with theoretical computations. Calculated absorption spectra of silver clusters in the gas phase ranging from 2 to 8 atoms in size show drastic differences between distinct cluster structures [142, 143]. In one case, the static polarizability of small silver clusters shows even-odd oscillations with size [143] that is qualitatively reminiscent of the photo-catalytic behavior of small gold clusters [115]. The interband contribution to the imaginary part of the dielectric function was calculated for clusters ranging in size from 13 atoms to 586 atoms, and predicts that the onset of interband transitions and contributions to the dielectric function occurs at decreasing energy with increasing particle size. This calculation seems to be in contrast with experimental results which show visible luminescence from silver clusters [122, 123] and yet interband luminescence from bulk silver at 3.9 eV in the UV [144]. Thus, while theoretical studies are limited, the general trend of a strong dependence of the electronic properties on cluster size and arrangement can clearly be identified.

1.4 Colloidal semiconductor nanoparticles

1.4.1 Structural properties

Semiconductor nanocrystals typically in the size range of a few nanometers or just a few thousand of atoms fall into the transition regime between molecular clusters and bulk materials. As discussed above, the complete formation of a band structure for semiconductor materials requires larger nanocrystal sizes than in the case of their metal counterparts. Thus, semiconductor nanocrystals can serve as artificial atoms at larger length scales that enable easier fabrication and exhibit greater stability [13]. Since the electronic properties of semiconductor materials are dominated by interband transitions that are well spaced in energy [10], the effects of spatial confinement of the electrons play a critical role in the electronic properties of the materials [12, 145–147]. Consequently, the size and shape of semiconductor nanoparticles, as with metal

clusters, significantly influence the resulting electronic properties. In contrast to metal clusters, however, the fabrication techniques for semiconductor nanoparticles which enable impressive control over shapes and size are well established [14], making them ideal materials to study structure-property relationships within the cluster-to-bulk transition regime.

There are two general approaches to fabricating semiconductor nanoparticles [27, 148]. In the *top-down* approach, the general principle is to impose a structure onto a material system through either deposition or etching processes. Traditional semiconductor fabrication methods such as high resolution lithography with electrons or molecular beam epitaxy are employed to create various nanostructures. In contrast, the *bottom-up* approach seeks to guide the nanoparticle growth process beginning with the individual atoms. Colloidal synthesis is a wet-chemical nanoparticle fabrication technique where the nanostructure growth is finely tuned by controlling the synthesis reaction and has proven to be a monumentally facile and successful method for creating a wide range of both metal and semiconductor nanoparticles [11, 13, 14, 27, 149–156]. There are two general steps in the colloidal synthesis of semiconductor nanoparticles. The first step is the initial nucleation of the particle from the solvent which creates clusters of only a few atoms. Initiated by the rapid addition of a precursor to a stabilizing solvent that prevents particle aggregation, the nucleation step is typically a very fast process. The next step is the controlled growth of the particles around the nucleated seeds. This step is typically slower and requires accurate and precise control of the reaction parameters such as reactant choice and concentration, reaction temperature and solution pH to produce a mono-disperse set of crystalline particle morphologies [14, 15, 27].

Figure 1.8 illustrates several examples of possible semiconductor nanoparticle structures. The most common configuration of homogeneous nanoparticles are in the shape of spheres or rods and can consist of a wide variety of materials such as CdS, CdSe, ZnS, InP, PbSe, ZnSe, ZnO, CdTe or InAs [12, 14, 27]. Even more structural variety is attainable when the nanoparticle heterostructures are created in which one material acts as a core, and a second material acts as the shell [14]. A common

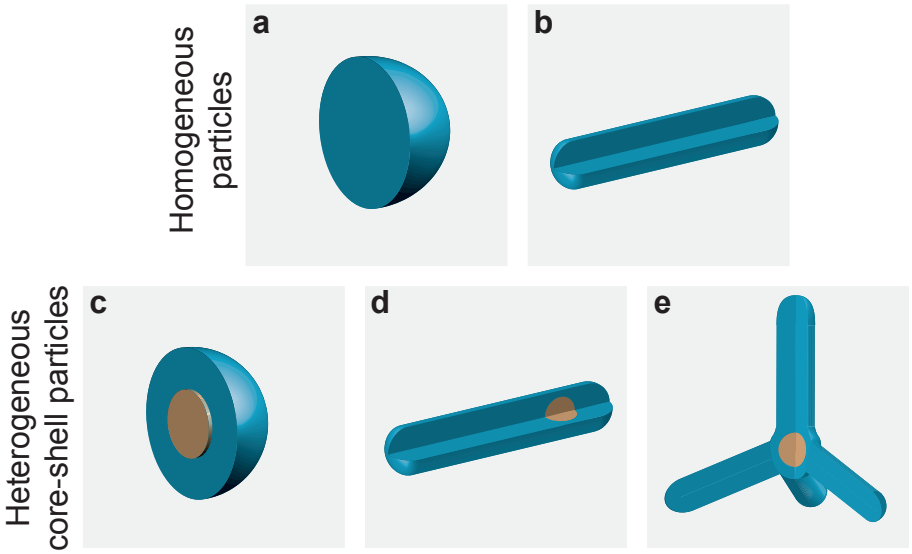

Figure 1.8. Examples of the variety of nanocrystal structures and material configurations enabled by colloidal synthesis techniques. Homogeneous CdSe nanocrystals can be grown in the shapes of (a) spheres [13, 149] or (b) rods [151], which can also be made of CdS [152]. CdS can also be used as an encapsulating shell around a CdSe core in the form of (c) spheres [150, 153], (d) rods [153, 154] or (e) tetrapods [154]. Tetrapods can also be fabricated using the two different crystal phases of CdSe [155] or CdTe [156].

combination of materials due to band gap energies that coincide with visible light energy is CdS and CdSe. This work focuses primarily on nanoparticle heterostructures that consist of a spherical CdSe core surrounded by a CdS shell. Possible CdS shells result in three nanoparticles geometries: spheres [150, 153], rods [153, 154], and tetrapods [154]. The exact structural details of the materials and heterostructures used in this work are discussed at length in Section 2.4.2.

1.4.2 Electronic properties

Semiconductor nanoparticles are unique electronic systems in large part because they merge the effects of the molecular-to-bulk transition (Section 1.1) with their bulk properties [11, 13]. A bulk semiconductor consists of a periodic arrangement of atoms which can be considered semi-infinite in extent [10]. An electron within a periodic lattice assumes a plane-wave wavefunction which must have a half-wavelength equal to an integer multiple of the lattice spacing. Whereas the lattice periodicity establishes a minimum half-wavelength on the electron plane waves the spatial extent of the crystal imposes a maximum half-wavelength on the electron plane waves. At the minimum, when the wavelength of the electron is equal to twice the spacing of the lattice (i.e., at the Brillouin zone boundary), a standing wave is formed which can assume two configurations with different energies that define the band-edge states in the material. The lower energy configuration maximizes electron density over the atomic cores in the lattice, while the higher energy configuration maximizes electron density between the atomic cores. The energy difference between these two configurations forms an energetic gap of available states for electrons in the lattice. For a semiconductor, the valence electrons fill all of the available states in the top-most valence band gap. Electrical conduction in an undoped semiconductor requires thermal energy which excites a non-negligible amount of electrons into the conduction band where a continuum of higher-lying energy states allows for efficient conduction. Similarly, at photon energies below the band gap threshold, the material is optically transparent.

Significant optical absorption only sets in for photons that exceed the band gap energy between the conduction band and the valence band [10]. Upon optical exci-

tation, an electron is promoted into the conduction band, and a vacancy is left in the sea of electrons in the valence band, which behaves as a single positively charged particle called a *hole*. Optical excitation thus creates an excited state which consists of a single electron in the conduction band and a positively charged hole in the valence band. The opposite charge of the electron and hole result in a coulombic interaction between the two particles. The strength of the interaction is primarily determined by the polarizability of the semiconductor material, and typically in semiconductors nanoparticles, the interaction is strong enough for the electron and hole to form a hydrogen-like bound state called an *exciton*. Complete relaxation of the exciton occurs when the electron and hole recombine, thus replacing the hole in the valence band with the electron from the conduction band. Upon recombination, the exciton must instantaneously release a packet of energy equal to the band gap minus the electron-hole interaction energy. Especially in direct-gap semiconductors, exciton relaxation often occurs via the emission of a photon resulting in luminescence [10].

In nanoparticles, the effects of an appreciable band gap and a filled set of valence states is convolved with the effects of carrier confinement and give rise to a unique set of optical properties [12,158,159]. The size of the exciton in a bulk semiconductor material is characterized by the average distance between the electron and hole - the *Bohr radius* - which is typically several nanometers for semiconductors [10]. When the size of a nanoparticle exceeds the Bohr radius, the dominant interaction for the electron and hole is their coulombic interaction [12]. For systems with dimensions less than the Bohr radius, increased spatial confinement of the electrons and holes results in both a forced increase in the coulombic interaction energy as well an energy associated simply with carrier confinement. The latter effect is termed *quantum confinement* and is depicted schematically in Figure 1.9. Analogous to the particle in a box model, the increased confinement increases the energy of both the highest valence state and the lowest conduction state as $1/a^2$, where a is the size of the nanocrystal. The quantum confinement effect increases the energy of the conduction band state more than the valence band state [12]. Consequently, with decreasing size, the band gap of the semiconductor nanocrystal increases. Since the coulombic

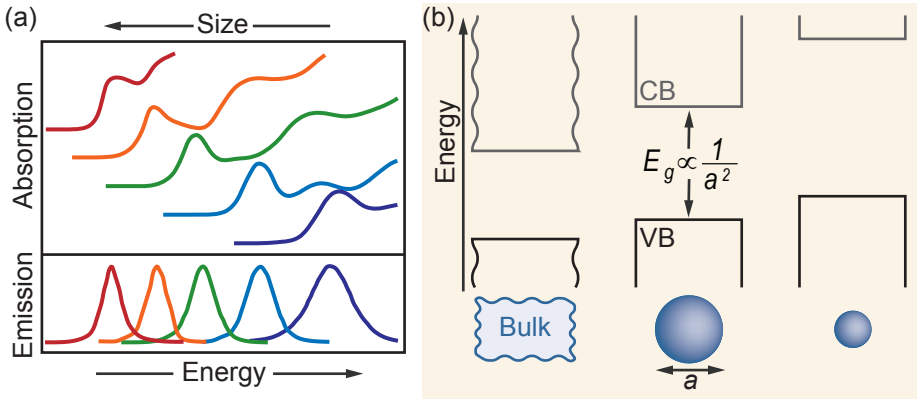

Figure 1.9. Quantum confinement in semiconductor nanocrystals is manifested in the band-edge electronic properties. (a) The onset of absorption and the luminescence shift to higher energies as crystal size decreases [157]. (b) Confinement of the highest valence band and lowest conduction band states increase their energies in analogy to a particle in the box leading to a larger band gap for smaller crystal sizes [12].

interaction scales as $1/a$, the quantum confinement effect increasingly dominates the exciton energy with decreasing particle size. For sizes near the Bohr radius of the exciton, the nanoparticles are considered to be in the *weak confinement* regime. As the confinement effect increasingly dominates for sizes much smaller than the Bohr radius, the *strong confinement* regime is entered. Perhaps the best illustration of the quantum confinement effect is in the optical absorption and emission spectra of semiconductor nanocrystals. As nanoparticles decrease in size, the band gap increases resulting in a shift of both absorption and emission spectra to higher energies [157]. The oscillator strength of the exciton transition, which can be judged qualitatively by the height of the first peak feature following the absorption onset, also increases with increasing quantum confinement [160].

The shape of a nanoparticle has important effects on the quantum-confinement as well as the corresponding optical properties. Analogous to the plasmon modes in metal nanoparticles (Section 1.2.2), it is generally accepted that a deviation in shape from an isotropic sphere will separate degenerate states in the valence band [12,158]. The splitting induced by the shape anisotropy is suspected to smear out the well-defined states leading to a less-prominent absorption spectrum for nonisotropic

shapes. Shape also plays a critical role in the emission properties [12]. As the aspect ratio of nanoparticles is increased from unity (i.e., a sphere), the luminescent emission becomes polarized [161]. Originally, this was attributed to a crossing of the valence band states induced by the particle anisotropy, but is now suspected to arise from the dielectric anisotropy of the particle and its surrounding environment [162]. The role shape plays on the interactions in a nanoparticle with multiple excitons has also been investigated [163]. This study showed that the shape of the particle carefully controls the interaction energy of the excitons. Some shapes allow for a net attractive interaction, while others result in a net repulsion between the two excitons.

1.4.3 Electronic properties of heterostructures

A semiconductor heterostructure is a single system constituted of two or more distinct semiconductor materials and is typically realized by growing one semiconductor material system on top of another (i.e., single crystalline Ge on top of single crystalline GaAs, or a CdS shell surrounding a CdSe core) [10]. Generally, the band gaps as well as the energetic position of the valence and conduction band states of the two different materials differ. For bulk heterojunctions, the alignment of the conduction and valence bands and the band gap is controlled primarily by material choice. In nanoparticles, though, the choice of material as well as the size of the constituent materials controls the relative alignment of the valence and conduction band states [147, 164].

Three band alignment schemes for semiconductor nanoparticles are identified in Figure 1.10 and can be expressed in terms of excited state carrier localization [166]. While lower energy states in the conduction band serve as wells for electrons, higher energy states in the valence band are wells for holes: electrons sink to the bottom while holes float to the top [10]. Misalignment of the conduction and valence band states will result in potential energy barriers that will localize electrons and holes to one material in the heterostructure. In a Type I configuration, both the electron and hole are confined to the same material, which has both a lower-lying conduction band state as well as a higher-lying valence band state. Strong confinement of the

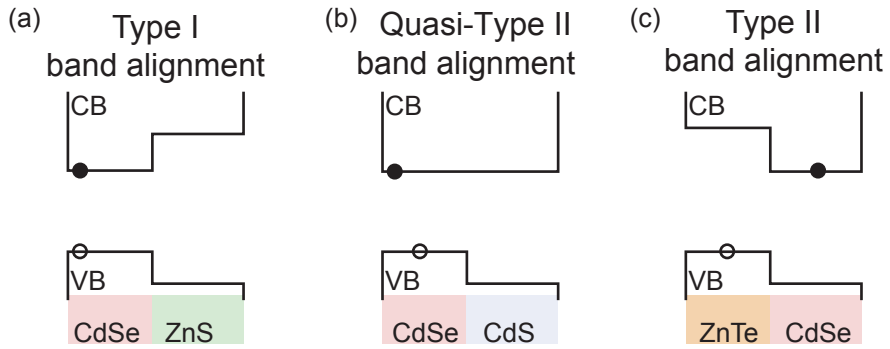

Figure 1.10. Band alignment and excited state carrier localization in heterostructure nanocrystals. The choice of materials controls the band alignment and excited state carrier localization in heterostructure nanocrystals. (a) In a Type I scheme, the valence band and conduction band states are oriented such that the electron and hole are confined in one material. (b) In a quasi-Type II scheme, either the valence band states or conduction band states align such that one carrier is localized to one material while the other carrier is delocalized over the whole structure. (c) In a Type II scheme each carrier localizes to a different material [165].

hole and electron to one material serves as an effective passivation technique for semiconductor nanoparticles [157, 166]. By enclosing a CdSe core with a ZnS shell, the hole and electron are prevented from interacting with and becoming trapped on surface defect states. Consequently, radiative recombination of the electron and hole is greatly promoted and observed as a significant increase in quantum yield [157,166]. In a Type II configuration, charge separation is promoted. One material has both lower-lying valence band and conduction band states. As a result, the electron localizes to one material while the hole localizes to another. The induced spatial separation of the electron and hole greatly reduce the probability of electron-hole recombination through radiative recombination. Finally, an interesting intermediate configuration between Type I and Type II exists [167]. While a large offset is present between the valence band states of CdSe and CdS, there is only a marginal and almost negligible offset between the conduction band states. As a result, a quasi-Type II band alignment scheme is realized where the hole strongly localizes to the core while the electron remains primarily delocalized over both materials.

The interface of the heterostructure can play an important role in its electronic

properties. In bulk heterojunctions, electrons diffuse in the valence band from one material to the other such that the Fermi level is constant across the interface [10]. This effect can establish further potential wells and barriers for electrons or holes in the conduction or valence bands, respectively, and can also apply to nanoparticle heterostructures, but is limited [157]. More importantly, the lattice mismatch between the two materials can often be substantial. For example, the lattice spacing of CdSe and CdTe differ by about 7 % while those of CdSe and CdS only differ by 4 %. As shown in Figure 1.11, lattice mismatch can result in deformation of the lattice away from the equilibrium bond lengths. In bulk heterostructures, this can lead to a lattice mismatch defect. However, nanoparticles are more deformable, and the mismatch usually results in a compression or expansion of bond lengths at the interface [157]. As a result, a strain field can be established at the interface, which can give rise to subtle barriers or wells that, as shown in Section 5, can affect excited state carrier localization within the nanoparticle.

1.5 Single particle emission dynamics

Cycling a material between an excited and ground state through absorption and then emission of a photon reveals a wealth of information about the electronic prop-

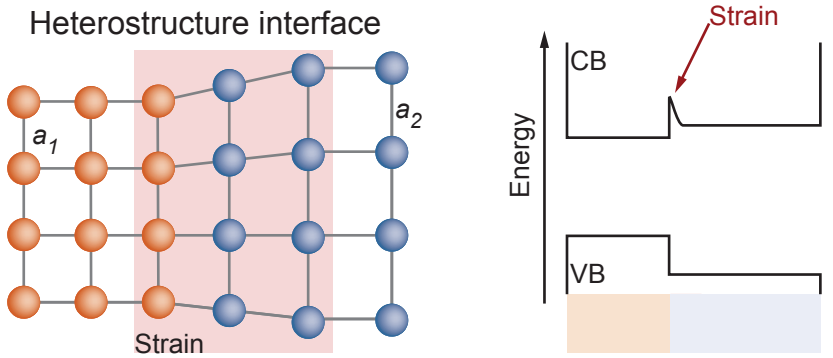

Figure 1.11. Interface effects in semiconductor heterostructures. A significant lattice mismatch between the materials in a heterostructure nanocrystal can lead to strain and defects at the interface. These interface effects can create an interfacial barrier that prevents complete thermalization of excited state carriers [157].

erties of a material system. Traditionally, this process is observed at the *ensemble* level where perhaps millions of molecules or nanoparticles undergo the excitation and emission process. In comparison to this ensemble level, the unique emission properties at the single particle level reveal the quantum nature of the emission process [168]. Unique to a single quantum emitter is a property termed *photon antibunching* which has been observed from single atoms [169], molecules [170], semiconductor nanoparticles [171,172], and metal clusters [121]. Such measurements show that these single particle systems only emit one photon at a time as would be expected from an isolated quantum mechanical system, therefore establishing the quantum mechanical nature of single particle emission: if a single particle in the excited state emits a photon it necessarily cannot emit a second photon as it has relaxed to the ground state. The established quantum nature of single particle emission leads to pronounced emission dynamics which are considered signatures of isolated single particles.

1.5.1 Blinking and spectral diffusion

The instantaneous leap between the excited state and ground state of single emitters also gives rise to striking intensity fluctuations in a quantum mechanical system that consists of two excited states with different relaxation rates [173]. In the case of single molecules, excitation occurs to the singlet excited state which subsequently relaxes to the ground state through photon emission. However, it is possible that the singlet state transitions to the triplet excited state which has a significantly weaker transition rate back to the ground state [174, 175]. As shown in Figure 1.12(a), this excursion to a state with a lower relaxation rate results in discrete jumps in emission between two distinct intensity levels: a *bright* or *on* state and a *dark* or *off* state. In semiconductor nanoparticles, similar blinking is observed [176]. In this case, the *dark* state is typically attributed to a charged nanoparticle where the exciton relaxes by giving its energy to the excess charge through Auger processes [159]. Discrete blinking is also observed from the luminescence from small silver clusters [108, 137, 177]. In this case, an emissive silver cluster is thought to transition to the dark state due to either charging or a structural change in the cluster.

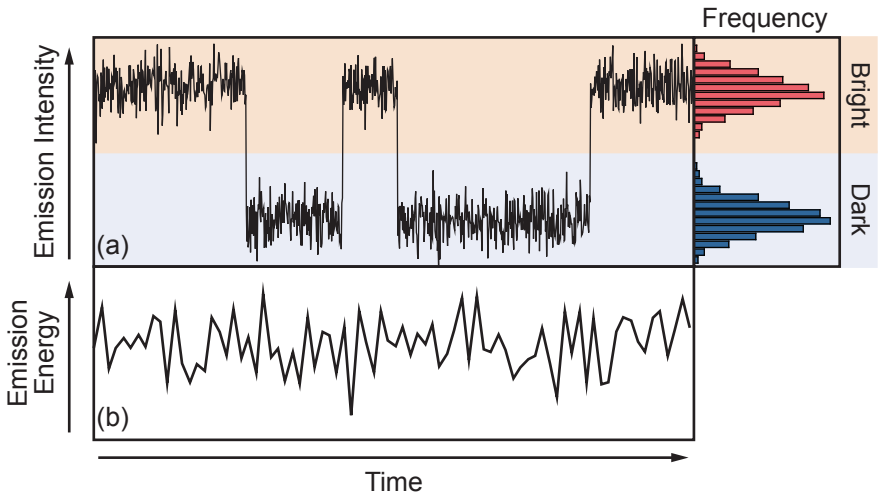

Figure 1.12. Single particle emission dynamics. Single particle or molecule emitters exhibit emission dynamics that fall into two main categories. (a) Blinking generally describes drastic fluctuations in emission intensity. (b) Spectral diffusion describes changes in the emission energy which is manifested as shifts in the luminescence spectrum.

The amount of time a single emitter spends in its bright (dark) state is considered its on (off) time. The distribution of on and off times can be obtained from the intensity traces of the single particles. Interestingly, the distribution of on and off time occurrences tends to follow a power law for single particle emitters [177–180]. A distribution of this form which spans such a wide range of time scales is indicative of very complex behavior such as diffusion governed charging events [179]. The seemingly ubiquitous occurrence of a power law distribution for the on and off times of single emitters is still an area of active interest, and its origins have yet to be completely isolated. Consequently, blinking phenomena are still actively studied for a variety of material systems.

Recently, in analogy to emission, blinking was observed in the conductance of semiconductor nanorods [181]. The current across a single CdS nanorod was shown to fluctuate between a high and low state, suggesting that the conductivity of a nanorod exhibits similar blinking as the luminescence. However, the on and off times for the current exhibited Gaussian distributions with defined averages, and thus

appear disentangled from luminescence blinking. Careful analysis of the intensity and quantum yields of semiconductor nanoparticles in the dark and bright states challenge the Auger recombination model [182] and have shown that intermediate "grey" states may exist [183]. It also seems that interactions with neighboring particles affect the blinking dynamics and on/off distributions for semiconductor nanoparticles suggesting a novel method for investigating interparticle interactions [184]. This concept has also been used to probe exciton migration and energy transfer in conjugated polymers [185].

Separate from intensity fluctuations, single emitters also display significant spectral shifts of their emission as shown in Figure 1.12(b). The effect is termed *spectral diffusion* or *spectral jitter* and has been observed in single molecules, semiconductor nanoparticles [186], and metal clusters [108]. Unlike blinking, spectral diffusion is not thought to be strictly a quantum mechanical process. Rather, its occurrence reflects the sensitivity of a single emitter to its environment and structure. For silver clusters, dynamic changes to the geometric structure of the cluster are attributed as the source of the observed spectral diffusion [108, 177]. Spectral diffusion in semiconductor nanoparticles, on the other hand, is attributed to rearrangements of local charge distributions in the surrounding environment induced by the excess excitation energy lost in the form of localized heating [187]. Local electric fields can couple to a semiconductor nanoparticle through a Stark shift, which modifies the energy of the electronic states. Thus random changes in the surrounding dielectric environment induced by thermalization of the nanoparticle can modify the energetic gap between the conduction and valence band states, changing the observed transition energy.

Antibunching, blinking, and spectral diffusion are considered unique characteristics of single particle emitters. Oftentimes qualitative observations of fluctuations serve as an indication of single particle emitters [108]. Although the blinking and spectral diffusion have the potential to illuminate the intricate details of the dynamics of a single particle emitter, the effects are often parasitic to measurements and potential applications. Thus, much effort is put into minimizing the effects. For

example, in this work measurements on single semiconductor nanoparticles were performed at cryogenic temperatures (4 K) to increase intensity and spectral stability.

1.6 Nonlinear optical response of a material

When a material is illuminated with light at naturally occurring intensity levels (i.e., solar radiation), its response is generally linear. The illumination induces a dipole with a strength that is linearly proportional to the incident electric field and leads to either linear scattering or absorption. Under sufficiently intense illumination that is typically only available with a laser source, the strength of the induced dipole can show a nonlinear dependence on the electric field [29]. At such intensity levels, materials begin to display a nonlinear optical response where two or more photons are simultaneously absorbed into virtual states of the system that subsequently relaxes by emitting a lesser number of higher energy photons, as shown in Figure 1.13.

The nonlinear response of a material is usually treated with classical electrodynamics [29, 188]. First, the incident electric field, $\boldsymbol{E}$, and the induced polarization, $\boldsymbol{P}$, at position $\boldsymbol{r}$ and at time t are expanded into their Fourier components

$$\boldsymbol{P}(\boldsymbol{r},t) = \sum_i \boldsymbol{P}(\omega_i) \text{ and } \boldsymbol{E}(\boldsymbol{r},t) = \sum_i \boldsymbol{E}(\omega_i). \tag{1.6}$$

Then a single frequency component of the polarization can be treated as a power series expansion around the incident electric field:

$$\begin{aligned} \boldsymbol{P}(\omega_i) = \; & \bar{\bar{\chi}}^{(1)}(\omega_i) \cdot \boldsymbol{E}(\omega_i) \\ & + \textstyle\sum_{j,k} \bar{\bar{\chi}}^{(2)}(\omega_i = \omega_j + \omega_k) : \boldsymbol{E}(\omega_j)\boldsymbol{E}(\omega_k) \\ & + \textstyle\sum_{j,k,l} \bar{\bar{\chi}}^{(3)}(\omega_i = \omega_j + \omega_k + \omega_l) : \boldsymbol{E}(\omega_j)\boldsymbol{E}(\omega_k)\boldsymbol{E}(\omega_l) \\ & + \ldots \end{aligned} \tag{1.7}$$

The macroscopic proportionality constants, $\bar{\bar{\chi}}$, are referred to as the material susceptibility and ultimately relate back to the microscopic polarizability of the material. The linear response of the material is encompassed by $\bar{\bar{\chi}}^{(1)}$, and the nonlinear response lies in the higher order terms in the expansion, which are only accessible with large electric fields. The most common nonlinear responses are the second-order ($\bar{\bar{\chi}}^{(2)}$) and third-order ($\bar{\bar{\chi}}^{(3)}$) responses which are typically 8 and 15 orders of magnitude weaker than the corresponding linear response ($\chi^{(1)}$) [29]. Second-order processes include

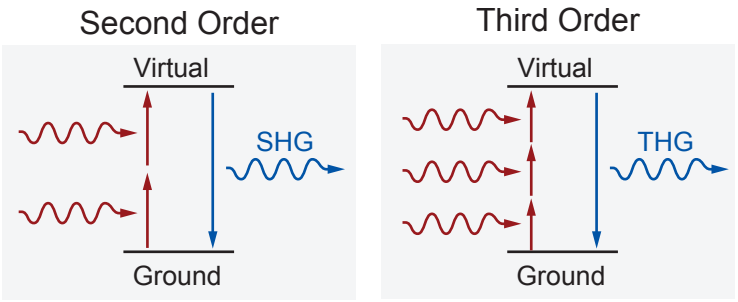

Figure 1.13. Example second- and third-order nonlinear responses of a material.

second-harmonic generation (SHG) and sum-frequency generation (SFG). In both processes, two incident photons are combined into one photon equal to the summed energy of the original photons. SHG is typically used to frequency-double light: infrared light with a wavelength of, for example, 900 nm is focused into a crystal with a strong second-order nonlinearity to produce light with a wavelength of 450 nm. Since the material polarization depends on $\boldsymbol{E}^2$, emission intensity from second-order processes typically depends quadratically on the incident illumination. So, if the intensity of the incident illumination doubles, the SHG intensity would be expected to quadruple. Similarly, an example third-order process would be third-harmonic generation (THG) where three photons are combined into one photon. Keeping with the previous example, 900 nm illumination would be converted into 300 nm, and again, since the material polarization depends on $\boldsymbol{E}^3$, the third-order emission is expected to depend cubicly on the intensity of the incident illumination.

Since both $\boldsymbol{E}$ and $\boldsymbol{P}$ are vectors, strictly speaking the proportionality constants must be tensors of increasing rank where $\bar{\bar{\chi}}^{(1)}$ is a second-rank tensor. The explicit values of the tensor components are determined by the crystal structure of the respective material. In general, even-order and odd-order nonlinear processes have important symmetry requirements. The fundamental source of the nonlinear response is the polarizability of the individual molecular bonds in a material, which can be treated in the context of the Drude model with the addition of a restoring force [29, 188]. A second-order nonlinear response as well as higher-order even responses of the bond are only possible in a noncentrosymmetric material with a restoring

force from an anharmonic potential. Thus, centrosymmetic materials (materials possessing inversion symmetry) do not have a second-order response. Third-order and higher odd-order nonlinear responses do not have such symmetry requirements and are found in most materials. For example, silver, which is studied in this work, has a face-centered-cubic (FCC) crystal structure of only silver atoms. Since the FCC crystal structure is centrosymmetric, silver does not have a *bulk* second-order nonlinear response.

In all centrosymmetric bulk systems, the inversion symmetry is broken within approximately 10 atomic layers near the surface of the material [189]. Simply, this is due to lack of material extent beyond the surface. Thus, interfaces between two materials naturally break inversion symmetry and can show an appreciable second-order nonlinear response. Surface-SHG has proven to be a valuable surface analysis tool on account of its incredible sensitivity to changes at the surface such as monolayer deposition of a polarizable material. Thus, even though *bulk* silver does not exhibit a second-order response, its surface does.

Although the nonlinear responses of a material are very weak in comparison to the linear response, both second-order and third-order responses from nanoparticle systems have been observed at the single-particle level [36]. For nanoparticles made of a centrosymmetric material, the second-order response is a highly sensitive probe of the surface properties of the nanoparticle. It turns out that for a completely symmetric spherical nanoparticle made of centrosymmetric material, the SHG arising from the surface of the nanoparticle can completely cancel out [190]. So, in principle, not only does SHG from centrosymmetic nanoparticles probe the surface nonlinearity of the particle, it also probes changes in the physical structure of the particle at unprecedented levels.

1.7 References

[1] S. A. Maier, *Plasmonics: Fundamentals and Applications*, Springer, 2007.

[2] U. Kreibig and M. Vollmer, *Optical Properties of Metal Clusters*, Springer, 1995.

[3] D. K. Gramotnev and S. I. Bozhevolnyi, Nat. Photonics. **4**, 83 (2010).

[4] J. N. Anker et al., Nat. Mater. **7**, 442 (2008).

[5] S. Lal, S. Link, and N. J. Halas, Nat. Photonics **1**, 641 (2007).

[6] W. L. Barnes, A. Dereux, and T. W. Ebbesen, Nature **424**, 824 (2003).

[7] V. M. Shalaev, *Nonlinear Optics of Random Media: Fractal Composites and Metal Dielectric Films*, Springer, Berlin, 2000.

[8] D. S. Wiersma, P. Bartolini, A. Lagendijk, and R. Righini, Nature **390**, 671 (1997).

[9] K. Kneipp, H. Kneipp, I. Itzkan, R. Dasari, and M. Feld, Chem. Rev. **99**, 2957 (1999).

[10] C. Kittel, *Introduction to Solid State Physics*, John Wiley & Sons Inc., 2005.

[11] A. L. Rogach, *Semiconductor Nanocrystal Quantum Dots: Synthesis, Assembly, Spectroscopy, and Applications*, Springer, 2005.

[12] A. Efros and M. Rosen, Annu. Rev. Mater. Sci. **30**, 475 (2000).

[13] A. P. Alivisatos, Science **271**, 933 (1996).

[14] D. V. Talapin, J. S. Lee, M. V. Kovalenko, and E. V. Shevchenko, Chem. Rev. **110**, 389 (2010).

[15] P. V. Kamat, J. Phys. Chem. B **106**, 7729 (2002).

[16] P. Yu, *Fundamentals of Semiconductors: Physics and Materials Properties*, Springer, 1999.

[17] K. L. Kelly, E. Coronado, L. L. Zhao, and G. C. Schatz, J. Phys. Chem. B **107**, 668 (2003).

[18] S. Link and M. A. El-Sayed, J. Phys. Chem. B **103**, 8410 (1999).

[19] S. Link and M. A. Ei-Sayed, Annu. Rev. Phys. Chem. **54**, 331 (2003).

[20] P. Mulvaney, Langmuir **12**, 788 (1996).

[21] S. Peng, J. M. McMahon, G. C. Schatz, S. K. Gray, and Y. Sun, Proc. Natl. Acad. Sci. U. S. A. **107**, 14530 (2010).

[22] M. A. van Dijk, M. Lippitz, and M. Orrit, Acc. Chem. Res. **38**, 594 (2005).

[23] M. A. van Dijk et al., Phys. Chem. Chem. Phys. **8**, 3486 (2006).

[24] V. Drachev et al., Phys. Rev. B **69**, 353181 (2004).

[25] J. Zheng, P. Nicovich, and R. Dickson, Annu. Rev. Phys. Chem. **58**, 409 (2007).

[26] T. Jensen, L. Kelly, A. Lazarides, and G. Schatz, J. Cluster Sci. **10**, 295 (1999).

[27] C. Burda, X. Chen, R. Narayanan, and M. El-Sayed, Chem. Rev. **105**, 1025 (2005).

[28] J. D. Jackson, *Classical Electrodynamics*, John Wiley & Sons Inc., 1998.

[29] R. W. Boyd, *Nonlinear Optics*, Academic Press, 2003.

[30] P. Nordlander, C. Oubre, E. Prodan, K. Li, and M. I. Stockman, Nano Lett. **4**, 899 (2004).

[31] K. Munechika, J. M. Smith, Y. Chen, and D. S. Ginger, J. Phys. Chem. C **111**, 18906 (2007).

[32] C. Sönnichsen et al., Phys. Rev. Lett. **88**, 077402 (2002).

[33] J. Mock, M. Barbic, D. Smith, D. Schultz, and S. Schultz, J. Chem. Phys. **116**, 6755 (2002).

[34] K. Lindfors, T. Kalkbrenner, P. Stoller, and V. Sandoghdar, Phys. Rev. Lett. **93**, 037401 (2004).

[35] G. Bachelier, I. Russier-Antoine, E. Benichou, C. Jonin, and P.-F. Brevet, J. Opt. Soc. Am. B **25**, 955 (2008).

[36] M. Danckwerts and L. Novotny, Phys. Rev. Lett. **98**, 026104 (2007).

[37] C. Hubert et al., Appl. Phys. Lett. **90**, 181105 (2007).

[38] R. Jin, J. E. Jureller, H. Y. Kim, and N. F. Scherer, J. Am. Chem. Soc. **127**, 12482 (2005).

[39] R. Jin, J. E. Jureller, and N. F. Scherer, Appl. Phys. Lett. **88**, 263111 (2006).

[40] B. Lamprecht, A. Leitner, and F. R. Aussenegg, Appl. Phys. B: Lasers Opt. **68**, 419 (1999).

[41] C. Voisin, N. Fatti, D. Christofilos, and F. Vallee, J. Phys. Chem. B **105**, 2264 (2001).

[42] M. R. Beversluis, A. Bouhelier, and L. Novotny, Phys. Rev. B **68**, 115433 (2003).

[43] A. Bouhelier, M. R. Beversluis, and L. Novotny, Appl. Phys. Lett. **83**, 5041 (2003).

[44] R. A. Farrer, F. L. Butterfield, V. W. Chen, and J. T. Fourkas, Nano Lett. **5**, 1139 (2005).

[45] K. Imura, T. Nagahara, and H. Okamoto, J. Am. Chem. Soc. **126**, 12730 (2004).

[46] H. Wang et al., Proc. Natl. Acad. Sci. U. S. A. **102**, 15752 (2005).

[47] H. Xu, J. Aizpurua, M. Käll, and P. Apell, Phys. Rev. E **62**, 4318 (2000).

[48] A. Liebsch, Phys. Rev. B **48**, 11317 (1993).

[49] B. Palpant et al., Phys. Rev. B **57**, 1963 (1998).

[50] K. Willets and R. Van Duyne, Annu. Rev. Phys. Chem. **58**, 267 (2007).

[51] L. Sherry et al., Nano Lett. **5**, 2034 (2005).

[52] Y. Sun and Y. Xia, Analyst **128**, 686 (2003).

[53] P. Mulvaney, J. Pérez-Juste, M. Giersig, L. Liz-Marzán, and C. Pecharromán, Plasmonics **1**, 61 (2006).

[54] Y. Chen, K. Munechika, and D. S. Ginger, Nano Lett. **7**, 690 (2007).

[55] Y. Chen et al., Appl. Phys. Lett. **93**, 053106 (2008).

[56] A. Kinkhabwala et al., Nat. Photonics **3**, 654 (2009).

[57] C. Nehl, H. Liao, and J. Hafner, Nano Lett. **6**, 683 (2006).

[58] J. S. Shumaker-Parry, H. Rochholz, and M. Kreiter, Adv. Mater. **17**, 2131 (2005).

[59] B. Wiley et al., Nano Lett. **7**, 1032 (2007).

[60] T. Itoh, K. Hashimoto, and Y. Ozaki, Appl. Phys. Lett. **83**, 2274 (2003).

[61] M. Miller and A. Lazarides, J. Phys. Chem. B **109**, 21556 (2005).

[62] G. A. Wurtz, J. S. Im, S. K. Gray, and G. P. Wiederrecht, J. Phys. Chem. B **107**, 14191 (2003).

[63] A. Sundaramurthy et al., Phys. Rev. B **72**, 165409 (2005).

[64] B. Lamprecht et al., Phys. Rev. Lett. **84**, 4721 (2000).

[65] S. I. Bozhevolnyi, I. I. Smolyaninov, and A. V. Zayats, Phys. Rev. B **51**, 17916 (1995).

[66] K.-H. Su et al., Nano Lett. **3**, 1087 (2003).

[67] S. Malynych and G. Chumanov, J. Am. Chem. Soc. **125**, 2896 (2003).

[68] P. Hanarp, M. Kăll, and D. Sutherland, J. Phys. Chem. B **107**, 5768 (2003).

[69] T. Jensen, M. Malinsky, C. Haynes, and R. Van Duyne, J. Phys. Chem. B **104**, 10549 (2000).

[70] L. Yin et al., Nano Lett. **5**, 1399 (2005).

[71] K. Bao, N. Mirin, and P. Nordlander, Appl. Phys. A: Mater. Sci. Process. **100**, 333 (2010).

[72] N. Verellen et al., Nano Lett. **9**, 1663 (2009).

[73] B. Luk'yanchuk et al., Nat. Mater. **9**, 707 (2010).

[74] P. Gadenne, Y. Yagil, and G. Deutscher, J. Appl. Phys. **66**, 3019 (1989).

[75] M. Breit et al., Phys. Rev. B **64**, 125106 (2001).

[76] D. Beaglehole and O. Hunderi, Phys. Rev. B **2**, 309 (1970).

[77] G. T. Boyd, Z. H. Yu, and Y. R. Shen, Phys. Rev. B **33**, 7923 (1986).

[78] G. T. Boyd, T. Rasing, J. R. R. Leite, and Y. R. Shen, Phys. Rev. B **30**, 519 (1984).

[79] C. K. Chen, A. R. B. de Castro, and Y. R. Shen, Phys. Rev. Lett. **46**, 145 (1981).

[80] D. P. Tsai et al., Phys. Rev. Lett. **72**, 4149 (1994).

[81] P. Zhang, T. L. Haslett, C. Douketis, and M. Moskovits, Phys. Rev. B **57**, 15513 (1998).

[82] S. S. Grésillon et al., Phys. Rev. Lett. **82**, 4520 (1999).

[83] V. P. Safonov et al., Phys. Rev. Lett. **80**, 1102 (1998).

[84] V. A. Markel et al., Phys. Rev. B **59**, 10903 (1999).

[85] I. I. Smolyaninov, A. V. Zayats, and C. C. Davis, Phys. Rev. B **56**, 9290 (1997).

[86] J. Beermann and S. I. Bozhevolnyi, Phys. Rev. B **69**, 155429 (2004).

[87] V. Krachmalnicoff, E. Castanié, Y. De Wilde, and R. Carminati, Phys. Rev. Lett. **105**, 183901 (2010).

[88] S. I. Bozhevolnyi, J. Beermann, and V. Coello, Phys. Rev. Lett. **90**, 197403 (2003).

[89] C. Anceau, S. Brasselet, J. Zyss, and P. Gadenne, Opt. Lett. **28**, 713 (2003).

[90] V. M. Shalaev and A. K. Sarychev, Phys. Rev. B **57**, 13265 (1998).

[91] M. I. Stockman, S. V. Faleev, and D. J. Bergman, Phys. Rev. Lett. **87**, 167401 (2001).

[92] M. I. Stockman, D. J. Bergman, C. Anceau, S. Brasselet, and J. Zyss, Phys. Rev. Lett. **92**, 057402 (2004).

[93] M. I. Stockman, Chem. Phys. **318**, 156 (2005).

[94] J. Beermann, I. P. Radko, A. Boltasseva, and S. I. Bozhevolnyi, Opt. Express **15**, 15234 (2007).

[95] M. Futamata, Faraday Discuss. **132**, 45 (2006).

[96] J. R. Lombardi and R. L. Birke, Acc. Chem. Res. **42**, 734 (2009).

[97] M. Moskovits, J. Raman Spectrosc. **36**, 485 (2005).

[98] M. J. Walter et al., Phys. Rev. Lett. **98**, 137401 (2007).

[99] N. Pieczonka and R. Aroca, ChemPhysChem **6**, 2473 (2005).

[100] A. Otto, M. Lust, A. Pucci, and G. Meyer, Can. J. Anal. Sci. Spectrosc. **52**, 150 (2007).

[101] T. Itoh et al., J. Phys. Chem. B **110**, 21536 (2006).

[102] T. Itoh et al., J. Chem. Phys. **124**, (2006).

[103] T. Itoh et al., J. Photochem. Photobiol., A **183**, 322 (2006).

[104] J. Rubim and R. Aroca, Phys. Chem. Chem. Phys. **10**, 5412 (2008).

[105] K. Domke, D. Zhang, and B. Pettinger, J. Phys. Chem. C **111**, 8611 (2007).

[106] S. Nie and S. Emory, Science **275**, 1102 (1997).

[107] W. H. Park and Z. H. Kim, Nano Lett. **10**, 4040 (2010).

[108] L. A. Peyser, A. E. Vinson, A. P. Bartko, and R. M. Dickson, Science **291**, 103 (2001).

[109] L. Peyser, T.-H. Lee, and R. Dickson, J. Phys. Chem. B **106**, 7725 (2002).

[110] M. Jacobson and K. Rowlen, Chem. Phys. Lett. **401**, 52 (2005).

[111] P. Andersen, M. Jacobson, and K. Rowlen, J. Phys. Chem. B **108**, 2148 (2004).

[112] M. J. Walter, N. J. Borys, G. Gaefke, S. Hger, and J. M. Lupton, J. Am. Chem. Soc. **130**, 16830 (2008).

[113] R. E. Palmer, S. Pratontep, and H. G. Boyen, Nat. Mater. **2**, 443 (2003).

[114] Y. Lei et al., Science **328**, 224 (2010).

[115] D. Lim, R. Dietsche, M. Bubek, G. Ganteför, and Y. Kim, ChemPhysChem **7**, 1909 (2006).

[116] D. C. Lim, R. Dietsche, G. Ganteför, and Y. D. Kim, Chem. Phys. Lett. **457**, 391 (2008).

[117] P. Gruene et al., Science **321**, 674 (2008).

[118] A. Perez et al., Int. J. Nanotechnol. **7**, 523 (2010).

[119] J. Zheng, C. Zhang, and R. M. Dickson, Phys. Rev. Lett. **93**, 077402 (2004).

[120] A. Longo et al., Nanotechnology **18**, 365701 (2007).

[121] L. Peyser-Capadona et al., Phys. Rev. Lett. **94**, 058301 (2005).

[122] W. Harbich et al., J. Chem. Phys. **93**, 8535 (1990).

[123] S. Fedrigo, W. Harbich, and J. Buttet, J. Chem. Phys. **99**, 5712 (1993).

[124] L. König, I. Rabin, W. Schulze, and G. Ertl, Science **274**, 1353 (1996).

[125] I. Rabin, W. Schulze, and G. Ertl, J. Chem. Phys. **108**, 5137 (1998).

[126] D. Ievlev, I. Rabin, W. Schulze, and G. Ertl, Chem. Phys. Lett. **328**, 142 (2000).

[127] Z. Y. Li et al., Nature **451**, 46 (2008).

[128] M. Muniz-Miranda, J. Raman Spectrosc. **33**, 295 (2002).

[129] K. D. Crawford and K. D. Hughes, J. Phys. Chem. B **102**, 2325 (1998).

[130] O. Monti, J. Fourkas, and D. Nesbitt, J. Phys. Chem. B **108**, 1604 (2004).

[131] A. Mayoral et al., Chem. Commun. **46**, 8758 (2010).

[132] D. Alamanova, V. Grigoryan, and M. Springborg, J. Phys. Chem. C **111**, 12577 (2007).

[133] L. Jensen, L. Zhao, and G. Schatz, J. Phys. Chem. C **111**, 4756 (2007).

[134] O. Bakr et al., Angew. Chem., Int. Ed. Engl. **48**, 5921 (2009).

[135] M. Jacobson and K. Rowlen, J. Phys. Chem. B **110**, 19491 (2006).

[136] T. Gleitsmann, B. Stegemann, and T. Bernhardt, Appl. Phys. Lett. **84**, 4050 (2004).

[137] C. Geddes, A. Parfenov, I. Gryczynski, and J. Lakowicz, J. Phys. Chem. B **107**, 9989 (2003).

[138] C. Mihalcea, D. Büchel, N. Atoda, and J. Tominaga, J. Am. Chem. Soc. **123**, 7172 (2001).

[139] J. Zheng, Y. Ding, B. Tian, L. Zhong, and X. Zhuang, J. Am. Chem. Soc. **130**, 10472 (2008).

[140] S. Patel et al., J. Phys. Chem. C **113**, 20264 (2009).

[141] C. M. Ritchie et al., J. Phys. Chem. C **111**, 175 (2007).

[142] V. Bonačić-Koutecky, V. Veyret, and R. Mitrić, J. Chem. Phys. **115**, 10450 (2001).

[143] J. Idrobo, S. Öğüt, and J. Jellinek, Phys. Rev. B **72**, (2005).

[144] A. Mooradian, Phys. Rev. Lett. **22**, 185 (1969).

[145] L. Brus, J. Chem. Phys. **79**, 5566 (1983).

[146] G. Einevoll, Phys. Rev. B **45**, 3410 (1992).

[147] J. Haus, H. Zhou, I. Honma, and H. Komiyama, Phys. Rev. B **47**, 1359 (1993).

[148] J. Barth, G. Costantini, and K. Kern, Nature **437**, 671 (2005).

[149] C. B. Murray, D. J. Norris, and M. G. Bawendi, J. Am. Chem. Soc. **115**, 8706 (1993).

[150] X. Peng, M. C. Schlamp, A. V. Kadavanich, and A. P. Alivisatos, J. Am. Chem. Soc. **119**, 7019 (1997).

[151] X. Peng et al., Nature **404**, 59 (2000).

[152] R. D. Robinson et al., Science **317**, 355 (2007).

[153] D. V. Talapin et al., Nano Lett. **3**, 1677 (2003).

[154] D. V. Talapin et al., Nano Lett. **7**, 2951 (2007).

[155] L. Manna, E. C. Scher, and A. P. Alivisatos, J. Am. Chem. Soc. **122**, 12700 (2000).

[156] L. Manna, D. J. Milliron, A. Meisel, E. C. Scher, and A. P. Alivisatos, Nat. Mater. **2**, 382 (2003).

[157] A. M. Smith and S. Nie, Acc. Chem. Res. **43**, 190 (2010).

[158] A. L. Efros and A. V. Rodina, Phys. Rev. B **47**, 10005 (1993).

[159] A. L. Efros and M. Rosen, Phys. Rev. Lett. **78**, 1110 (1997).

[160] T. Vossmeyer et al., J. Phys. Chem. **98**, 7665 (1994).

[161] J. Hu et al., Science **292**, 2060 (2001).

[162] C. Shan, Z. Liu, and S. Hark, Phys. Rev. B **74**, 153402 (2006).

[163] M. Saba et al., Adv. Mater. **21**, 4942 (2009).

[164] Y. Nonoguchi, T. Nakashima, and T. Kawai, Small **5**, 2403 (2009).

[165] G. Scholes, Adv. Funct. Mater. **18**, 1157 (2008).

[166] C. de Mello Donegá, Phys. Rev. B **81**, 165303 (2010).

[167] J. Müller et al., Phys. Rev. B **72**, 205339 (2005).

[168] W. Moerner and M. Orrit, Science **283**, 1670 (1999).

[169] H. Kimble, M. Dagenais, and L. Mandel, Phys. Rev. Lett. **39**, 691 (1977).

[170] T. Basché, W. Moerner, M. Orrit, and H. Talon, Phys. Rev. Lett. **69**, 1516 (1992).

[171] P. Michler et al., Nature **406**, 968 (2000).

[172] V. Zwiller et al., Appl. Phys. Lett. **78**, 2476 (2001).

[173] F. D. Stefani, J. P. Hoogenboom, and E. Barkai, Phys. Today **62**, 34 (2009).

[174] R. M. Dickson, A. B. Cubitt, R. Y. Tsien, and W. E. Moerner, Nature **388**, 355 (1997).

[175] D. A. Vanden Bout et al., Science **277**, 1074 (1997).

[176] M. Nirmal et al., Nature **383**, 802 (1996).

[177] X. Wu and E. Yeow, Nanotechnology **19**, 1 (2008).

[178] R. Verberk and M. Orrit, J. Chem. Phys. **119**, 2214 (2003).

[179] F. Cichos, C. von Borczyskowski, and M. Orrit, Curr. Opin. Colloid Interface Sci. **12**, 272 (2007).

[180] M. Kuno, D. P. Fromm, H. F. Hamann, A. Gallagher, and D. J. Nesbitt, J. Chem. Phys. **115**, 1028 (2001).

[181] H. Steinberg et al., Nano Lett. **10**, 2416 (2010).

[182] J. Zhao, G. Nair, B. R. Fisher, and M. G. Bawendi, Phys. Rev. Lett. **104**, 157403 (2010).

[183] P. Spinicelli et al., Phys. Rev. Lett. **102**, 136801 (2009).

[184] D. P. Shepherd et al., J. Phys. Chem. C **114**, 14831 (2010).

[185] H. Lin et al., J. Am. Chem. Soc. **130**, 7042 (2008).

[186] S. Empedocles, D. Norris, and M. Bawendi, Phys. Rev. Lett. **77**, 3873 (1996).

[187] T. Plakhotnik et al., Phys. Rev. Lett. **105**, 167402 (2010).

[188] Y. R. Shen, Rev. Mod. Phys. **48**, 1 (1976).

[189] Y. R. Shen, Annu. Rev. Mater. Sci. **16**, 69 (1986).

[190] J. I. Dadap, J. Shan, K. B. Eisenthal, and T. F. Heinz, Phys. Rev. Lett. **83**, 4045 (1999).

CHAPTER 2

EXPERIMENTAL METHODS

2.1 Single particle spectroscopy

Single particle analysis is the ultimate sensitivity level at which to study a material system. Single particle spectroscopy involves measuring the optical response of a single particle and has been pursued since the late 1970s [1]. Continued advancements in optical collection techniques as well as detector sensitivity have made single particle spectroscopy for a wide array of material systems an almost routine activity today. For example luminescence [2], Raman scattering [3], Rayleigh scattering [4], and nonlinear scattering [5] from single particles such as single conjugated polymers, semiconductor nanocrystals, and metal nanoparticles have been observed. In this work, single particle spectroscopy techniques are combined with time-resolved spectroscopy and electron microscopy to study semiconductor heterostructure nanocrystals and optical hot spots of semicontinuous silver films.

Even though the most applicable material properties, in a practical sense, involve the behavior at the ensemble level, there are several reasons to study materials at the single particle level [6, 7]. In ensemble-level measurement, a large population of single emitters is sampled at once, therefore providing the average single emitter behavior in the immediate presence of other particles. Thus, the intrinsic, fundamental response of the material is convoluted with disorder broadening and possible interparticle effects such as energy transfer. Polarization anisotropy at the ensemble level, for instance, is limited to measuring the emission polarization of a large collection of randomly oriented dipoles with respect to an initial excitation polarization. On the single particle level, however, the obscurity introduced by the ensemble distribution of dipole orientations is lifted as only one single dipole is probed. Thus, the degree of polarization of a single emitter can be accurately probed without the complex

consideration of the ensemble distribution. In a broad sense, single emitter spectroscopy maps out the distribution of emitter properties that yields the averages measured by ensemble techniques. Probing the distribution of properties one entity at a time enables the detection of existing subensembles of emitters with potentially favorable properties for a given application. Part of this work pinpoints the origin of the occurrence of two distinct classes of single semiconductor nanocrystals, which are identified by their optical properties [8]. Each identified class has favorable distinctive features with respect to different applications that are then correlated to the morphologies of the nanoparticles. Such information can then be utilized in fabrication techniques where a given application is targeted.

On a more fundamental level, single emitter spectroscopy probes a material system in a regime where novel effects are often observed. As already discussed in Section 1.5, single emitters display unique characteristics which are obscured in the ensemble, such as blinking, spectral diffusion, and photon antibunching. The occurrence of these effects gives unprecedented insight into the fundamental dynamics of photoexcited states. For example, single hot spot spectroscopy of semicontinuous silver films presented here showed, for the first time, that SHG emission from rough silver films exhibits stark intensity fluctuations revealing complex photodynamics of a coherent scattering process with important implications for its use in biological labeling or medical imaging [9].

Two significant challenges arise when working at the single particle level. The first hurdle to overcome is achieving suitable spatial isolation such that the collected signal is most likely to come from only one single emitter. When a far-field microscope is employed to perform the single particle spectroscopy, as in this work, this challenge equates to a spatial distribution that ensures that only one particle falls into a diffraction-limited spot, and an interparticle spacing 2 to 3 times the diffraction limit. For the semiconductor nanocrystal work presented here, such a dispersed spatial distribution of particles is obtained by deposition of dilute solutions of the nanocrystals onto a suitable substrate [8]. As shown in Figure 2.1, the appropriate dilution is identified through series of decreasing concentrations. In the regime of

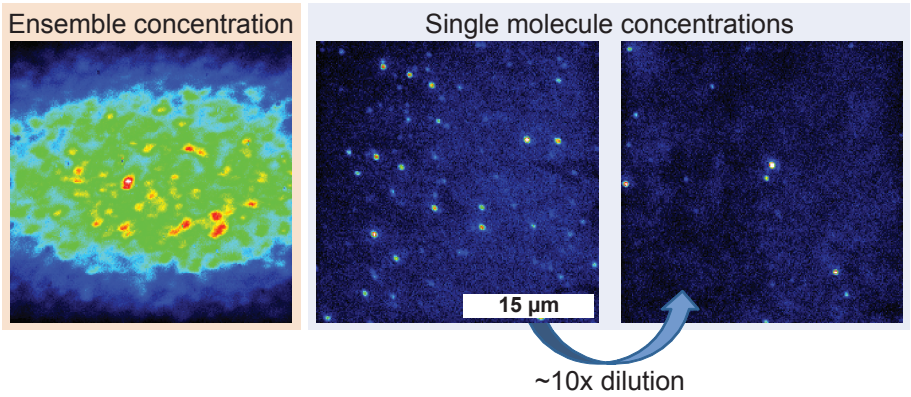

Figure 2.1. A dilution series of CdS nanorods embedded in an inert polymer matrix from ensemble concentrations down to single particle concentrations.

a dense film, the interparticle spacing is well below the diffraction limit, and many particles are stacked upon each other in a thick film. Increased dilution leads to thinner films until the limit of a one particle thick film is reached. At this point, further dilution creates a discontinuous film of discrete emission spots that get smaller and more separated with decreased solution concentrations. Finally, at the single particle limit, the discrete emission regions are well-separated, diffraction-limited spots. A definitive signature of appropriate single particle concentrations is the reduction of discrete emission spots without a reduction in the emission intensity per spot with increased dilution (see Figure 2.1). The validity of the dilution series approach is confirmed in Chapter 5 with correlated optical and electron microscopy of the same CdSe/CdS nanorods. For the hot spots on semicontinuous films, such an approach as the dilution series is not available and hot spot concentration is controlled with adequate film growth and optical excitation conditions (see Chapter 4 for more details).

The second challenge to surpass is collecting adequate emission signal from the emitter over any background signal. In this regard, the experimentalist is primarily limited by the collection efficiency of the microscope system, the sensitivity of the detector and the brightness of the single emitter (which is controlled by the emitter's optical absorption cross-section and quantum yield). In the experimental setup here

(see Section 2.6 for details), a long working-distance microscope objective is combined with a very sensitive charge-coupled device (CCD) camera. Background emission from the substrate and embedding polymer matrix are minimized by using high quality quartz or silicon substrates combined with the cleanest polymer matrix materials available. Contaminant radiation from the scattered laser excitation is reduced with high-quality interference filters. Finally, the material systems employed here are typically bright with respect to the background emission.

2.2 Time resolved spectroscopy

Time resolved spectroscopy measures how an excited state population decays, providing the excited state lifetime via the excited state optical emission. Consider a simple model of the emission from an excited fluorophore system [10]. The fluorophores relax to the ground state radiatively with the rate Γ, or nonradiatively with the rate k_{nr}. The overall decay of the excited state population is then a simple exponential decay,

$$N(t) = N_0 e^{-t(\Gamma + k_{nr})} \tag{2.1}$$

where $N(t)$ is the exited state population as a function of time, t, and N_0 is the initial population of the excited state. Since the number of relaxation events of the excited state is proportional to its population, the subsequent emission after excitation follows the same exponential decay. Time resolved spectroscopy measures both the intensity decay as well as how the emission spectrum of the excited state changes over the course of relaxation. Combining the information of the intensity and emission spectrum in the decay makes for a powerful tool, and in this work, it is used to segregate ultrafast scattering processes from slower luminescence emission from the silver films.

Time resolved photoluminescence can be measured with a streak camera. The operating principles for the streak camera are shown in Figure 2.2 [10,11]. Spectrally dispersed light is focused onto a photoelectrode which in turn emits electrons in the forward direction. The electrons are then propelled by an acceleration mesh into the streak tube. Within the streak tube, an anode and cathode are used to sweep a

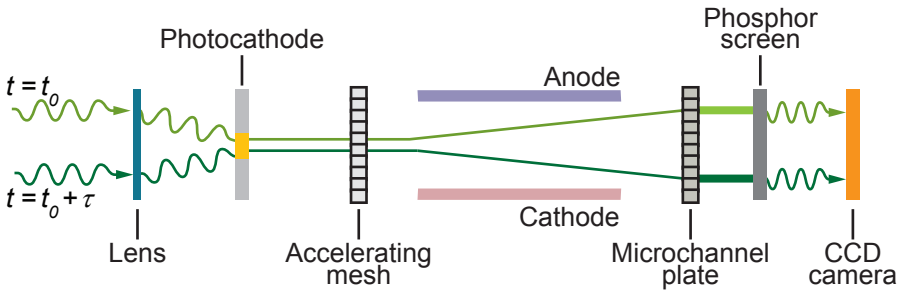

Figure 2.2. Schematic and operating principles of a streak camera.

time-dependent electric field that deflects the accelerated electrons. Since the applied electric field is time-dependent, the amount of deflection an electron experiences is correlated with the time that it was emitted from the photocathode; Electrons generated at the photocathode at later times will experience a large electric field in the streak tube and consequently, a larger vertical deflection. After passing through the streak tube, the electrons pass through a microchannel plate which multiplies the incident electrons before they strike a phosphor screen. The light generated from the phosphor screen is then imaged by a CCD camera. The image produced on the CCD camera thus contains spectral resolution in the horizontal dimension, and temporal resolution in the vertical direction. Since the decay of the excited state is measured with respect to an initial population in time resolved spectroscopy, pulsed excitation must be used, otherwise continuous excitation will continually repopulate the excited state and completely obscure the decay. A critical component to time resolved spectroscopy is synchronizing the operation of the streak camera with the excitation pulse, and complex electronics are employed to coordinate the streak system with initial arrival of the emission from the excited state.

2.3 Scanning electron microscopy

In Chapters 4 and 5, high resolution topographic images from a scanning electron microscope (SEM) are correlated to far-field microscopy images. As opposed to optical microscopy where the emission of photons from an emitter is analyzed, SEM uses an incident beam of high energy electrons to probe the emitter [12]. When compared to

photons, a beam of electrons can be focused to regions significantly smaller than the diffraction limit of light. Consequently, images obtained with an SEM easily surpass the resolution limit of optical microscopy.

A general schematic of a SEM is shown in Figure 2.3 [12]. The electrons used to probe the sample are generated in the top of the *column* by either a thermal or field-emission source and are then passed through a series of electron optics which collimate the electron beam and focus it onto the sample. Following the focusing optics are the scanning optics which can deflect the electrons such that the incident beam can be systematically rastered over a region on the sample. At each point in the raster scan, the focused electron beam interacts in three primary ways with the atoms of the sample. First, some electrons will be elastically scattered from the sample and are called *back-scattered electrons* (BSEs). Second, incident electrons can penetrate the sample, and then inelastically scatter with inner-shell electrons of the material. Termed *secondary electrons* (SEs), these lower-energy electrons can then scatter out of the sample and be detected at many points within the chamber or column. Third, the incident electrons can eject inner-shell electrons from the atom causing outer-shell electrons to relax into the vacant inner-shell states. The

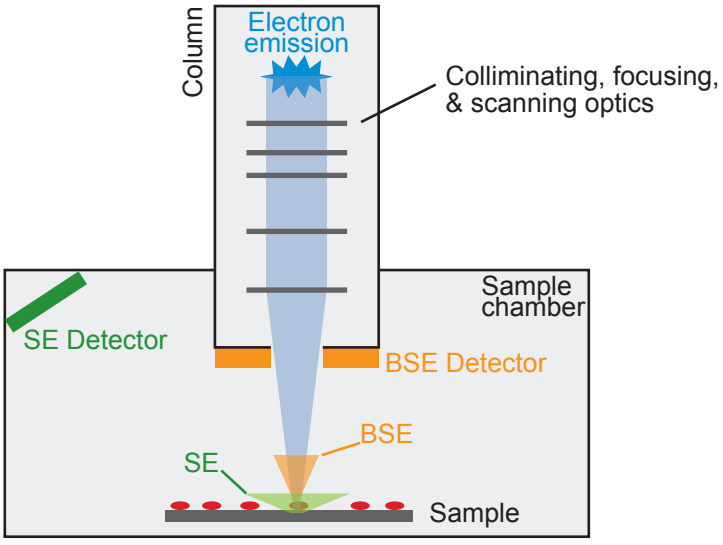

Figure 2.3. Configurational schematic of a scanning electron microscope.

relaxation process produces X-rays which can be used to determine the elemental composition of a sample. Depending on the detector, the emission of the SEs, BSEs, or X-rays is recorded at each point at which the electron beam is focused. In this manner, high resolution topographic images of a sample can be recorded. Several parameters, some of which are analogous to optical microscopy can be tuned for optimal image acquisition. These include the choice of detector, the focal length and working distance of the electron column, the scan speed and the landing energy of the incident electrons on the sample.

Since electrons are charged particles, a crucial aspect of SEM sample characterization is assuring that the sample can dissipate charge. For conducting materials on a conductive substrate, this requirement is easily met. In the case of the semiconductor nanocrystals used in Chapter 5, an n-doped silicon substrate adequately dissipated excess charge from the sample. The rough silver films were necessarily grown on an insulating substrate. Thus, characterizing the films below the percolation threshold proved challenging and required either a "low vacuum" imaging mode where the SEM chamber contained a low concentration of nitrogen which was used to avoid sample charging, or the use of a special back-scattered electron detector that enabled especially low incident electron energies (see Section 2.6.2 for more details).

Sample characterization with a SEM can be considered a nonreversible and often destructive process. Illuminating nanoparticles with a beam of high-energy electrons most likely degrades the samples. In addition, the incident electrons can interact with carbon-based contaminants and deposit what is best described as "burn marks" on a sample. In this work, SEM characterization of a sample was assumed to inflict a degree of permanent damage to the materials. Consequently, SEM measurements were *always* conducted *after* the optical characterization measurements to ensure degradation introduced by the electron beam did not affect the optically probed electronic properties.

2.4 Material systems

2.4.1 Tollens silver films

The semicontinuous metal films used in this experiment were exclusively fabricated by the Tollens reagent reaction as initially proposed for SERS substrates [13–15]. The Tollens reagent reaction is a simple wet-chemical process for depositing silver on glass that dates back to the late 19th century where it was briefly used to fabricate silver mirrors and now serves as a common reagent test for aldehydes. These Tollens films have been successfully used to probe single molecule SERS from conjugated polymers [8, 16, 17] and are of particular practical interest due to their significant SERS enhancement factors.

The synthesis process for Tollens silver films is rather simple [8]. In a clean beaker, a solution of volume V of silver nitrate ($AgNO_3$) is prepared at a concentration of $c = 0.3$ mol/l. To the silver nitrate solution, concentrated ammonium hydroxide is added drop-wise while continuously stirring until an initial brown precipitate forms. Additional ammonium hydroxide is added until the initial brown precipitate completely dissolves. To this solution, while still continuously stirring, a solution of potassium hydroxide (KOH, $c = 0.8$ mol/l) with a volume of $\frac{1}{2}V$ is added. The addition of KOH causes the formation of a second brown precipitate which is again fully dissolved with the drop-wise addition of ammonium hydroxide. The resulting clear solution, referred to as the "Tollens reagent," contains a fully dissolved silver diamine complex, $[Ag(NH_3)_2]^+$. Equal volumes of a glucose solution ($c = 0.5$ mol/l) and the Tollens reagent are mixed to initiate the reaction in which the aldehyde group reduces the silver diamine complex producing gluconic acid and free silver atoms which deposit on glass surfaces in contact with the reaction.

A typical Tollens film with a growth time of 150 s is characterized by atomic force microscopy (AFM) [18] and SEM in Figure 2.4. Both the SEM and AFM reveal the nanoscale roughness of the Tollens film. At these growth times, the Tollens films display a degree of self-similarity or fractal nature: the average roughness of the film scales with the size of the scan area in the form of a power law [15]. While such a scaling is not a traditional fractal, the self-similarity of the vertical topography of

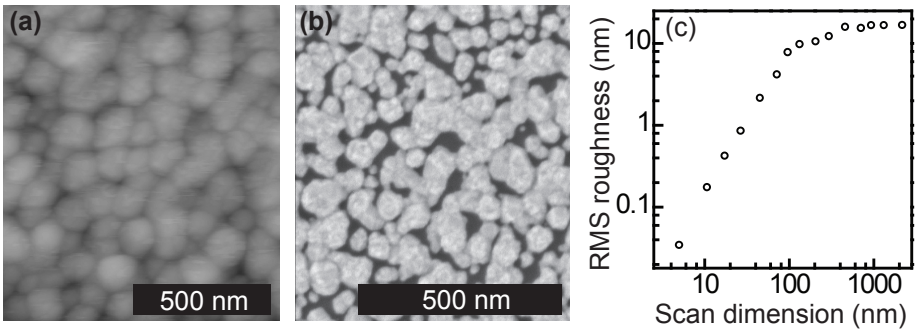

Figure 2.4. The general structure and characteristics of a Tollens film. (a) Typical AFM image of a Tollens film reveals nanoscale roughness (courtesy of S. Liu and J. M. Gerton). (b) The nanoscale roughness can also be seen under SEM. (c) Detailed analysis of the RMS roughness of a Tollens film reveals a degree of self-similarity on the nanoscale (data taken from Ref. [15]).

the Tollens films nevertheless contributes to broader resonances and stronger mode confinement of localized surface plasmons [19], as was introduced in Section 1.2.4.

2.4.2 CdSe/CdS core-shell heterostructures

In the final chapter of this work – Chapter 5 – the contribution of morphological anisotropy to the optically measured electronic properties of CdSe/CdS nanoparticles is explicitly explored. CdSe/CdS semiconductor nanocrystals possess a unique set of electronic and structural properties, which make them ideal systems to probe the role of shape on electronic properties in the nanocrystals.

All of the semiconductor nanocrystal systems used in this work were synthesized and graciously provided by J. Huang in the group of D. V. Talapin at the University of Chicago. In total, three distinct CdS morphologies were used as shells around a CdSe core which was kept to a size of approximately 4 nm in diameter. The basic optical, electronic, and structural properties have been characterized in detail in two publications of the D. V. Talapin group [20, 21] and will only be briefly reviewed in this section.

Figure 2.5 illustrates the three CdSe/CdS heterostructure morphologies used in this work alongside representative transmission electron microscopy (TEM) images and the typical electronic and optical properties of a CdSe/CdS core-shell nanocrystal

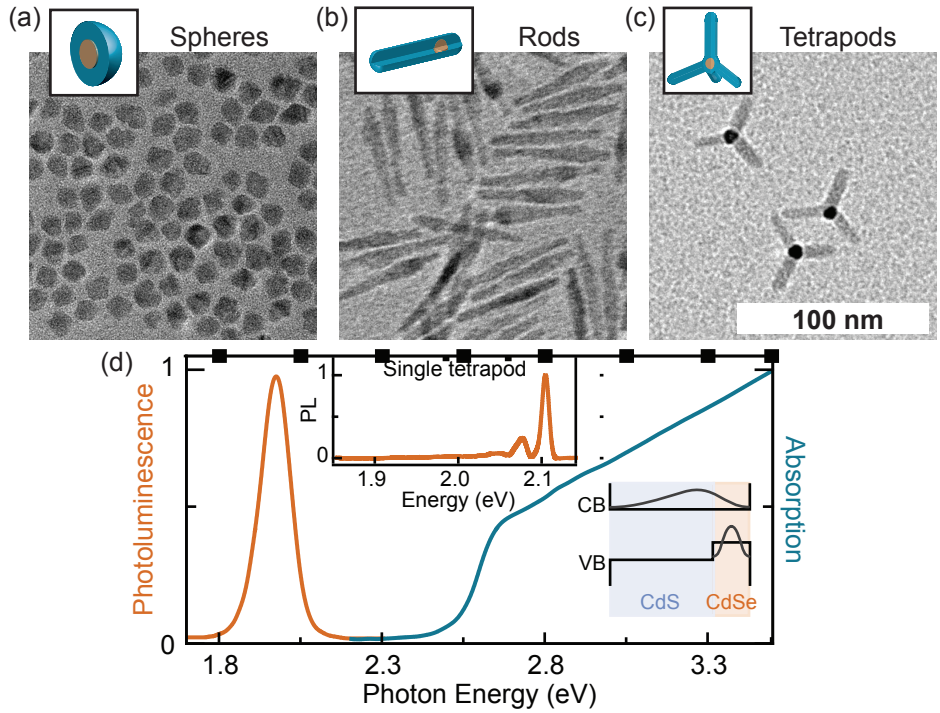

Figure 2.5. TEM characterization and optical properties of the CdSe/CdS core-shell heterostructures used in this work (TEM images provided by J. Huang). A CdS shell of (a) spherical, (b) rod, and (c) tetrapod morphologies surrounds a spherical CdSe core. (d) The conduction band states of CdSe and CdS approximately align ,delocalizing the electron over the whole nanoparticle and localizing the hole to the CdSe core. As a result, optical absorption is dominated by the CdS due to this component forming the larger physical structure, but emission arises almost exclusively from the core as is clearly observed in room temperature ensemble spectroscopy [20, 21] (ensemble spectroscopy data taken from Ref. [8]). Inset in (d), the emission of a single tetrapod at 5 K is void of the ensemble broadening in the corresponding bulk measurement and reveals coupling to the CdSe LO phonon mode, 27 meV beneath the zero phonon line at 2.1 eV [22].

system. The simplest shell shape is near-spherical, where the CdSe shell is surrounded by a roughly uniform 4 nm thick shell of CdS. Careful tuning of the synthesis conditions during the growth of the CdS shell leads to anisotropic growth in one direction providing the rod-shaped CdSe/CdS heterostructures used here [20], which are approximately 60 nm long and 6 nm in diameter. The anisotropic growth of the rod structures results in the localization of the CdSe core at typically one end of the rod. The third and final structure used is a striking tetrahedral shaped nanocrystal where the CdSe core is surrounded by a CdS shell with four arms and is referred to as a tetrapod structure. Each "arm" of the tetrapod is approximately 20 nm in length and 6 nm in diameter. For both the sphere and rod structures, the CdSe core and CdS shell both share the wurtzite crystal structures. However, the growth of the tetrapod structure requires the CdSe core to be in the zincblende cyrstal phase [21]. The zincblende crystal phase of the CdSe core provides four crystal facets with minimal lattice mismatch to the wurtzite crystal structure of CdS. Thus, CdS shell growth around a zincblende CdSe core occurs preferentially in four directions leading to the tetrapod shape [20, 21].

Although the crystal structures of the core materials are different, the ensemble characterization of the materials reveal similar electronic and optical properties [20, 21]. In panel (d) of Figure 2.5, the typical optical and electronic properties for the CdSe/CdS core-shell structures are shown. Ensemble optical measurements reveal that the absorption of the heterostructures is dominated by the CdS which has a bulk band gap of $\sim$2.6 eV while the emission is dominated by electron and hole recombination in the CdSe core which has a bulk band gap of $\sim$1.8 eV (in both the wurtzite and zincblende crystal phases) [23]. Previous single particles studies, in particular on the tetrapods and rod structures, suggested that, on average, the conduction band states between the two materials align and the reduced band gap of the CdSe results in a large offset in the valence band states [22, 24]. This electronic configuration is supported by the observed absorption and emission spectra: the strong offset in the valence band states leads to strong hole localization in the CdSe core, forcing radiative recombination of the hole and electron to occur at the band

gap energy of the CdSe core. In absorption, the CdS dominates simply because of the significantly larger amount of shell material over CdSe core material: the absorption cross-section of the shell dwarfs the absorption cross-section of the core. Because of these electronic and optical properties, the CdSe/CdS nanocrystals can be considered model light-harvesting systems where the CdS shell acts as an antenna system which absorbs light and then "funnels" the energy to the CdSe core [8].

Aside from acting as model light-harvesting systems, the CdSe/CdS nanostructures are close to ideal systems on which to perform single particle spectroscopy. First, the large shell structures provide both a large absorption cross-section as well as a very effective surface passivation for the luminescent CdSe cores. Thus, the shell absorbs a large number of photons, of which a significant portion radiatively recombine in the CdSe core giving a quantum yield of around 50 % [21]. The net result is that the large absorption cross-section and quantum yields make the heterostructures relatively bright single emitters and easy to detect at the single particle level. Although blinking can provide information on the photodynamics of a single particle, it is also a parasitic effect if long-term measurements are desired. In Chapter 5, the emission intensity and spectra of single nanocrystals is measured as a function of excitation energy. Such a measurement on a single particle takes approximately 1 hour and demands that blinking is minimized. This requirement is easily met with the CdSe/CdS core-shell nanostructures as the strong hole localization and the effective surface-passivation of the CdS shell minimize carrier trapping in surface states. Finally, the electronic properties result in a significant separation between the absorption and emission energies, making it easy to filter out scattered excitation light from the detector.

2.5 Sample preparation

2.5.1 General considerations

In this short section, the details of the sample preparation process for both the Tollens films and semiconductor nanoparticle samples are discussed. While the preparation techniques for the two materials are different, the two experiments shared

several general principles, especially and most importantly in regard to cleanliness.

The most important consideration when working on either single particle spectroscopy or single hot spot spectroscopy is cleanliness. Trace amounts of contamination arising from the sample preparation process or experimental setup can be detrimental to obtaining accurate and high-quality data. Every substrate used in this work (glass, high-quality quartz, and the n-doped silicon reference grids) went through a rigid cleaning process. About 20 substrates at a time were cleaned with the following steps [8]:

1. Sonicate in reagent grade acetone for 10 minutes.
2. Rinse with ultrapure water.
3. Sonicate in reagent grade isopropanol for 10 minutes.
4. Rinse with ultrapure water.
5. Sonicate in ultrapure water for 10 minutes.
6. Rinse with ultrapure water.
7. Sonicate in ultrapure water for 10 minutes.
8. Blow-dry with nitrogen.

The sonication in acetone, isopropanol, and ultrapure water served to remove any excess oils or films that may have been left on the substrates during the manufacturing or fabrication process.

Following these initial cleaning steps, the optically transparent substrates were coated on one side with a 100 nm aluminum mirror. The aluminum mirror blocks excitation radiation from illuminating potentially fluorescent adhesives used to contact the substrates to the cold-finger of the microscope system. If the substrates were to be used for single particle measurements on the CdSe/CdS nanocrystals, the above cleaning process was repeated to remove any contamination introduced during the thermal evaporation process.

The final step in the cleaning process used was to bake the substrates in a furnace at ∼500 ℃ for at least 30 minutes. This step aimed to remove any remaining carbon-based contamination from the surface by simply burning it off. Rigid adherence to the thorough cleaning steps presented here was always followed for all sample preparation.

2.5.2 Tollens metal films

The preparation of Tollens films utilized the exact reaction discussed in Section 2.4.1. Upon initiating the reaction by mixing the Tollens reagent and glucose solutions, a cleaned glass microscope slide[1] was immersed in the reaction causing the silver atoms to deposit on the glass slide and slowly produce a rough silver film. Upon removing the slide after the desired growth time, the Tollens film was rinsed first in warm ultrapure water, then in cold ultrapure water, and then finally blow-dried with nitrogen. The reaction kinetics and growth time (i.e., the amount of time the glass slide spent immersed in the reaction) determine the silver coverage and resulting film morphology, as shown in detail in Chapter 4. Since the kinetics depend on the temperature of the reaction, care was always taken to ensure the same reaction temperature for any comparative studies of different growth times.

Several precautions were always taken with the growth of silver films to ensure repeatability of the measurements:

- High quality silver-nitrate[2], potassium hydroxide[3], ammonium hydroxide[4], and glucose[5] were always used.
- All glassware used in the reaction was always cleaned by sonication first in a 2 % Hellmanex[6] solution followed by two sonications in ultrapure water.

---

[1] *Carolina Biological Supply*; Burlington, NC, USA; 0.2 mm thick cover slips

[2] *Sigma-Aldrich*; USA; silver nitrate, purity > 99.9999 %

[3] *Sigma-Aldrich*; USA; semiconductor grade potassium hydroxide, purity > 99.99 %

[4] *Sigma-Aldrich*; USA; 28 % ammonium hydroxide in water, purity > 99.99 %

[5] *Sigma-Aldrich*; USA; α-D-glucose, purity > 96 %

[6] *HellmaAnalytics*; Müllheim, Germany, supplied by *VWR*, USA

- The container in which the reaction was conducted was always baked at ∼500 ℃ for 30 minutes before use (and allowed to fully cool to room temperature).
- The Tollens reagent and glucose solutions were always prepared fresh and used within 15 minutes of preparation.
- The reactions were always conducted at room temperature.

Control measurements conducted over the course of this work indicated that the Tollens films were optically stable with time. Thus, Tollens films were often prepared and then stored under vacuum for later use, up to 2 weeks after preparation.

2.5.3 Single semiconductor nanocrystals

As discussed above, single particle measurements require the minimization of background signal as well as adequate interparticle spatial separation. Sample preparation is a crucial step in meeting these criteria, and the specific preparation technique here was adapted from previous single particle and single molecule studies [8].

Two types of single particle samples were prepared for this work and are illustrated in Figure 2.6. For experiments involving only optical measurement, single semiconductor nanocrystals were adequately dispersed in an inert polymer host matrix and deposited on a cleaned, aluminum-backed quartz microscope slide[7]. Zeonex[8] at concentrations of 10 mg/ml continued to prove to be an ideal host matrix [8] with minimum background emission and was used exclusively in this work. In contrast, when SEM characterization was required, the particles were deposited directly on an n-doped silicon substrate with a native oxide layer and chromium reference marks[9] without any host polymer matrix that would otherwise complicate the SEM imaging process.

Deposition of the particles on the substrates was accomplished by spin-coating a diluted solution of the particles at speeds in the range of 1000−5000 rounds per

[7] *Chemglass Life Sciences*; Vineland, NJ; 0.25 mm thick quartz coverslips

[8] *Zeon Chemicals L.P.*; Louisville KY, USA; *Zeonex 480R*

[9] Silicon reference grids supplied and fabricated by *MicroFab, University of Utah*

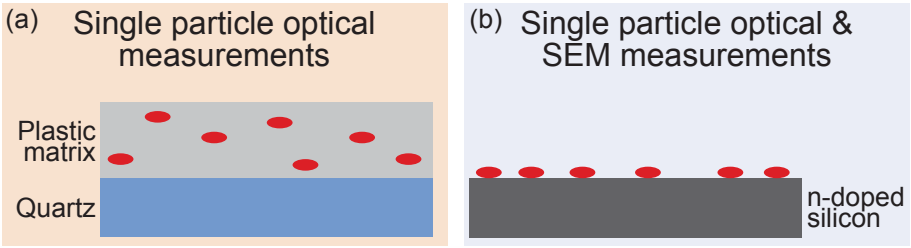

Figure 2.6. Schematic illustration of samples prepared for single particle measurements. (a) For optical measurements alone, single particles were dispersed in an inert polymer matrix on a thin quartz microscope slide. (b) For correlated optical and SEM measurements, particles were deposited directly on an n-doped conducting silicon substrate with a native oxide layer and a chromium reference grid.

minute. The spatial distribution of particles is a function of both the rotation speed of the spin-coating process as well as the concentration of the particles within the deposition solution. The diluted solutions were derived from the "mother" solution which contained a high concentration (exact concentration unknown) of nanoparticles dissolved in toluene. If the nanoparticles were to be embedded in a polymer matrix, they were progressively diluted in solutions of Zeonex dissolved into ultrapure toluene[10] at a concentration of 10 mg/ml. On the other hand, if the particles were to be deposited directly on the substrate, the nanoparticles were progressively diluted in just the ultrapure toluene. The correct concentration steps and spin-coating speeds depended on the original nanocrystal sample and had to be experimentally determined for each individual mother solution of tetrapods, rods, or spheres.

Utmost care and precautions were taken with every piece of equipment and chemical used to ensure the cleanliness of the prepared samples. In brief, containers of ultrapure toluene and matrix solutions were subjected to the same cleaning procedures as described for the substrates. Every vial used in the dilution of the mother solution was also baked out to avoid any possible contamination. Further, only noncontaminated pippettes and sterilized pippettor tips were used in the dilution and deposition processes.

---

[10] *EMD Chemicals*, USA; grade *OmniSolv*

2.6 Experimental configuration

2.6.1 Optical microscopy

The microscope system used in this work to perform the optical microscopy was designed and built as part of the Ph.D. thesis of M. J. Walter [8] with significant help at all stages of the process from the author of this work and additional support of K. J. van Schooten. The principal equipment and configuration of the microscope system is shown in Figure 2.7. A detailed discussion of all of the equipment can be found in the Ph.D. thesis of M. J. Walter [8].

In brief, samples mounted in a vertically-oriented cold-finger cryostat,[11] which was used to keep the samples under vacuum ($\sim 10^{-6}$ mbar) and optionally cool them to 4 K, were illuminated at a 60° angle with respect to the sample normal direction. The illumination source was a pulsed Ti:sapphire laser[12] (140 fs pulses produced at 80 MHz) which was tunable between 680 nm and 1080 nm. The excitation wavelength range could be extended to 340 nm - 540 nm by optionally directing the output of the laser through an autotracking SHG unit[13] which automatically adjusts the orientation of a nonlinear crystal and compensation crystal for optimum phase-matching and minimum beam-shift, respectively. Within the excitation path, achromatic $\lambda/2$ or $\lambda/4$ waveplates can be inserted to rotate the incident polarization or produce circularly polarized excitation, respectively. Following the polarization optics and the final mirror, an achromatic lens was used to focus the illumination spot to sizes as low as 20 μm in diameter on the sample. Motorized translation stages which moved the entire cryostat were then used to illuminate different regions of the sample.

Emission from the sample is collected by a large working-distance microscope objective[14] which is able to correct for aberrations introduced by the quartz window

---

[11] *Janis Research Company Inc.*; Wilmington, MA USA; model *ST-500* with the model *331S* temperature controller

[12] *Coherent Inc.*; Santa Clara, CA USA; model *Chameleon Ultra II*

[13] *APE*; Berlin, Germany; first-generation *HarmoniXX* with *Autotracker* option

[14] *Olympus America, Inc.*; Melville, NY USA; model *SLCPlanFl, 40x, NA=0.55, infinity corrected, corrective collar 0-2.6 mm*

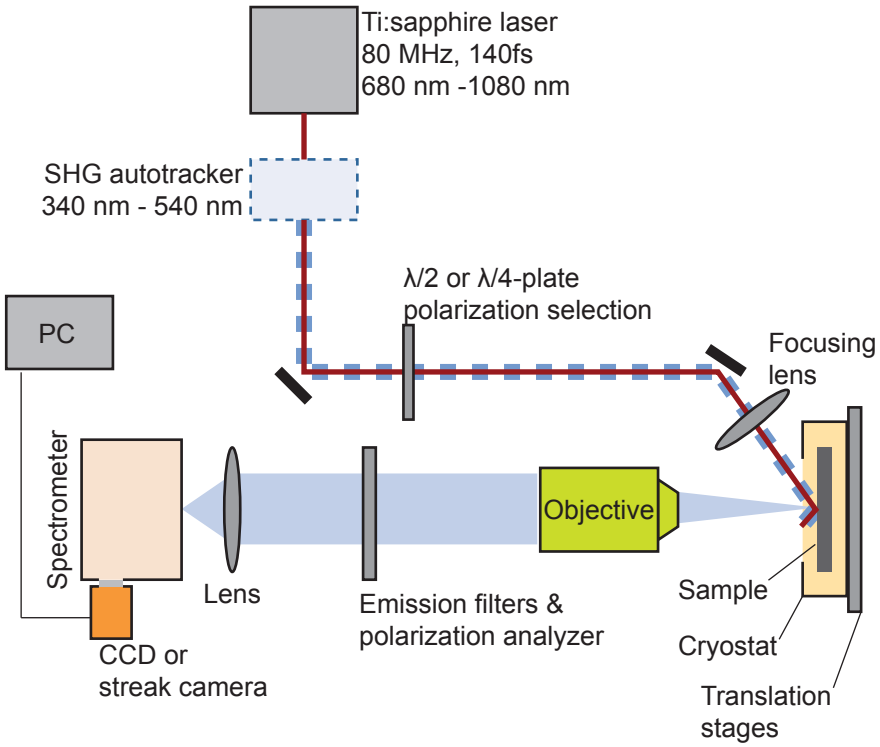

Figure 2.7. Experimental setup.

of the cryostat. The infinity-corrected beam from the microscope objective was then passed through high-quality interference filters with large extinction coefficients[15] which isolated the emission signal by blocking scattered excitation radiation. Optionally, a linear polarization filter could be placed in the emission path following the objective to selectively analyze a single polarization orientation. For single particle spectroscopy measurements, the filtered emission was imaged onto the entrance of an imaging spectrograph[16] which could either directly image or spectrally disperse the light onto a cooled CCD camera[17] operating at $-30\,^{\circ}\mathrm{C}$. For time resolved spectroscopy, the emission was directed around the single-particle imaging spectrograph and then focused onto a separate imaging spectrograph[18] which was attached to a streak camera.[19] For both systems, the data acquisition simply involved recording the image projected on the CCD camera as discussed in detail in Section 2.2 for the streak camera, and in Chapters 3 and 4 for the imaging and spectroscopy modes of the single particle microscope.

Experimental automation was possible for the single particle measurements. As part of the lab development the author, in conjunction with K. J. van Schooten, developed a LabView application capable of automating almost every aspect of the single particle microscope. Its primary functionality was to systematically acquire data after tuning the emission polarization analyzer and the excitation laser parameters, such as the wavelength, power and polarization. The microscope automation program served as a crucial time-saving tool, especially for the excitation-energy dependence measurements conducted in Chapter 4 and 5 and the polarization anisotropy measurements

---

[15] *Chroma Technology Corporation*; Bellows Falls, VT USA; and *Semrock, Inc.*; Rochester, NY USA

[16] *Princeton Instruments / Acton*; Trenton NJ, USA; model *SpectraPro SP-2556 Imaging Spectrograph; 500 mm focal length* with a mirror or ruled grating *ARC-1-015-500*, 6868 mm^2, 150 G/mm with 500 nm blaze wavelength

[17] *Princeton Instruments / Acton*; Trenton, NJ USA; model *CoolSNAP:HQ2*

[18] *Bruker Optics, Inc.*; Billerica, MA USA; model *250IS SureSpectrum* imaging spectrograph; 250 mm focal length a ruled grating, 50 G/mm with 600 nm blaze wavelength

[19] *Hamamatsu Corporation*; Bridgewater, NJ USA; model *C5680*

conducted in Chapters 3 and 4.

2.6.2 Electron microscopy

The SEM measurements were conducted on two nearly identical SEMs at different locations. Both SEMs used were the NovaNano Field Emission SEM systems produced by FEI. The SEM measurements on the Tollens films presented in Chapter 4 were conducted on a NovaNano system at the University of Utah[20] using a backscattered electron detector. The Tollens films were imaged at a working distance of 5.4 mm, at magnifications ranging from 60 kx to 1500 kx, with a beam current of 29 pA and with an electron beam voltage of 5.5 kV with beam deceleration enabled to minimize the landing energy of the electrons. Although the "high-vac" mode of the chamber was ultimately used, similar operating parameters in "low-vac" mode were explored for the Tollens film and also provided quality images. The SEM measurements on the CdSe/CdS nanorods were conducted on a NovaNano SEM system at the University of Chicago[21] using a secondary electron detector. Each nanorod was imaged with a working distance of 3.5 mm, at a magnification of 160 kx, with an electron beam current of 5.6 pA operating at a voltage of 5 kV.

2.7 References

[1] S. Weiss, Science **283**, 1676 (1999).

[2] W. E. Moerner and L. Kador, Phys. Rev. Lett. **62**, 2535 (1989).

[3] S. Nie and S. Emory, Science **275**, 1102 (1997).

[4] K. Munechika, J. M. Smith, Y. Chen, and D. S. Ginger, J. Phys. Chem. C **111**, 18906 (2007).

[5] R. A. Farrer, F. L. Butterfield, V. W. Chen, and J. T. Fourkas, Nano Lett. **5**, 1139 (2005).

[6] W. Moerner and M. Orrit, Science **283**, 1670 (1999).

[7] J. R. Lakowicz, *Principles of Fluorescence Spectroscopy*, chapter 23, pages 757–795, Springer, 2006.

[20] *FEI*; Hillsboro, OR USA; model *NanoNova FEG-SEM 630* using the *VCD* BSE detector

[21] *FEI*; Hillsboro, OR USA; model NanoNova FEG-SEM 200 using the *through-lens* SE detector

[8] M. J. Walter, *Light-harvesting in single conjugated polymer chains and semiconductor nanocrystals*, PhD thesis, University of Utah, 2009.

[9] N. Hodas, (private communication).

[10] J. R. Lakowicz, *Principles of Fluorescence Spectroscopy*, chapter 4, pages 757–795, Springer, 2006.

[11] *Instruction Manual for the Hamamatsu Corporation C5690 Streak Camera.*

[12] J. Goldstein, *Scanning Electron Microscopy and X-ray Microanalysis*, Springer, 2003.

[13] Y. Saito, J. J. Wang, D. A. Smith, and D. N. Batchelder, Langmuir **18**, 2959 (2002).

[14] Y. Saito, J. Wang, D. Batchelder, and D. Smith, Langmuir **19**, 6857 (2003).

[15] Z. J. Wang, S. L. Pan, T. D. Krauss, H. Du, and L. J. Rothberg, Proc. Natl. Acad. Sci. U. S. A. **100**, 8638 (2003), Tollens SERS.

[16] M. J. Walter et al., Phys. Rev. Lett. **98**, 137401 (2007).

[17] M. J. Walter, N. J. Borys, G. Gaefke, S. Hger, and J. M. Lupton, J. Am. Chem. Soc. **130**, 16830 (2008).

[18] AFM images kindly provided by Sue Liu and Jordan Gerton.

[19] V. M. Shalaev, *Nonlinear Optics of Random Media: Fractal Composites and Metal Dielectric Films*, Springer, Berlin, 2000.

[20] D. V. Talapin et al., Nano Lett. **3**, 1677 (2003).

[21] D. V. Talapin et al., Nano Lett. **7**, 2951 (2007).

[22] J. Müller et al., Phys. Rev. B **72**, 205339 (2005).

[23] O. Madelung, editor, *Semiconductors - Basic Data*, Springer, 1996.

[24] C. Mauser et al., Phys. Rev. B **77**, 153303 (2008).

CHAPTER 3

INTERMITTENCY IN SECOND-HARMONIC RADIATION FROM PLASMONIC HOT SPOTS ON ROUGH SILVER FILMS

Rough silver films are known to exhibit surface-enhanced optical processes, the most renowned of which is surface-enhanced Raman scattering (SERS). In addition to amplifying the local electric field to extents enabling single-molecule SERS, the localized collective oscillations of conduction electrons are also known to enhance nonlinear optical processes. In this chapter, the nonlinear microscopy of rough silver films reveals that the emission comes from discrete hot spots and consists of a stable, spectrally broad band and fluctuating second-harmonic generation. The pronounced fluctuations of the second-harmonic generation are reminiscent of blinking from single quantum emitters but unexpected as the nonlinear emission arises from coherent scattering process, which do not involve metastable states.

This chapter is reprinted from a paper published in 2009 as a "rapid communication" by *Physical Review B* in volume 80, on page 161407. Subsequently, it was highlighted in the "research highlights" section of *Nature Physics* in volume 5 on page 779. The manuscript was coauthored by Manfred J. Walter and John M. Lupton.[1] Subheadings for the text are inserted here for structural clarity and are not part of the published manuscript.

---

[1]N. J. Borys, M. J Walter, and J. M. Lupton; Intermittency in the second-harmonic radiation from plasmonic hot spots on rough silver films; Physical Review B 80, 161407 (2009).

3.1 Abstract

Surface enhancement of electromagnetic fields in plasmonic hot spots formed on rough silver films enables the observation of second-harmonic generation (SHG) from single metal nanoparticles. Nonlinear light scattering from these particles exhibits blinking in analogy to luminescence from single quantum dots, molecules and atoms; and fluctuations in single molecule surface-enhanced Raman scattering. Hot spots also display multiphoton white light emission besides SHG. In contrast to SHG, white light emission is stable with time, demonstrating that it is not the plasmonic field enhancement which fluctuates but the nonlinear polarizability ($\chi^{(2)}$) of the emitting species.

3.2 Introduction

Temporal fluctuations in the response of a nanoscale light source to an incident optical field provide intricate information on the physics of the system and its surroundings. Common examples of fluctuations include blinking in the light emission of single atoms [1, 2] molecules [3], or quantum dots [4]. While strong fluctuations in the emission of nanoscale objects can be understood in terms of saturation processes in two-level systems, it is not immediately obvious whether size limitations should impact quasiclassical nonlinear light scattering such as second-harmonic (SH) generation (SHG). We probe the nonlinear response of individual metal nanoparticles by amplifying the local electric (optical) field in the hot spot of a rough silver film [5, 6]. Nonlinear optical characterization of plasmon-mediated surface enhancement has attracted particular attention because of the increasing use of surface-enhanced Raman scattering (SERS), the most prominent application of plasmonic field amplification [7–12]. Fluctuations in single molecule SERS have been reported [9, 11, 12], which are thought to arise from changes in the interaction of the analyte molecule with the regions where largest field enhancement occurs–the hot spots. The same mechanism which enhances Raman scattering can also be probed by SHG [9,13–17] and nonlinear optical processes such as multiphoton luminescence and stimulated Brillouin scattering which lead to spectral continuum emission (CE) [5,18].

Using these nonlinear responses, we distinguish between the nonlinear susceptibilities $\chi^{(2)}$ and $\chi^{(3)}$ of a small particle in a hot spot. Whereas the $\chi^{(3)}$ response appears constant with time, $\chi^{(2)}$ exhibits strong temporal fluctuations reminiscent of blinking in single quantum emitters.

3.3 Experimental

We examined the nonlinear optical response of silver nanoparticle films which have previously allowed reproducible single molecule SERS spectroscopy [19,20]. The silver films are grown in a solution-based Tollens silver mirror reaction on glass, leading to fractal silver nanoparticle arrangements approximately 30 nm thick [19]. Figure 3.1 summarizes the main optical characteristics of such a silver film. A scanning electron micrograph of a sample illustrates the distribution of positions and sizes of nanoparticles in the right-hand inset of panel C. The film is mounted in high vacuum ($\sim 10^{-6}$ mbar) beneath a fluorescence microscope objective (numerical aperture 0.55) and excited under wide-field illumination at an angle of $\sim 30^{\circ}$ by infrared radiation from a tunable Ti:sapphire laser (80 MHz, 140 fs pulse length, ~ 1560 kW/cm^2 cw intensity). Figure 3.1(A) illustrates a typical emission pattern from the metal film under excitation at 1070 nm. Spatially discrete emission is observed as diffraction-limited bright spots. Placing a slit over the image (dashed lines in A) and directing the light through a spectrometer enables emission spectroscopy (B), spatially resolved along the vertical axis of the microscope image. The image in B and the graph in C show the corresponding spectrum of the bright spot in panel A, which appears broad with a narrow peak superimposed at 535 nm (the spectrum is truncated at 660 nm by a short-pass filter). The peak arises from SHG of the incident 1070 nm radiation whereas the broad emission results from CE [20]. Within the excitation densities under consideration, SHG and CE depend nonlinearly on excitation intensity as shown in the left-hand inset of panel C.

3.3.1 Results and discussion

Metal films constitute nonlinear optical materials where the second-order response is due to the structural and field discontinuities present at the surface [6], which

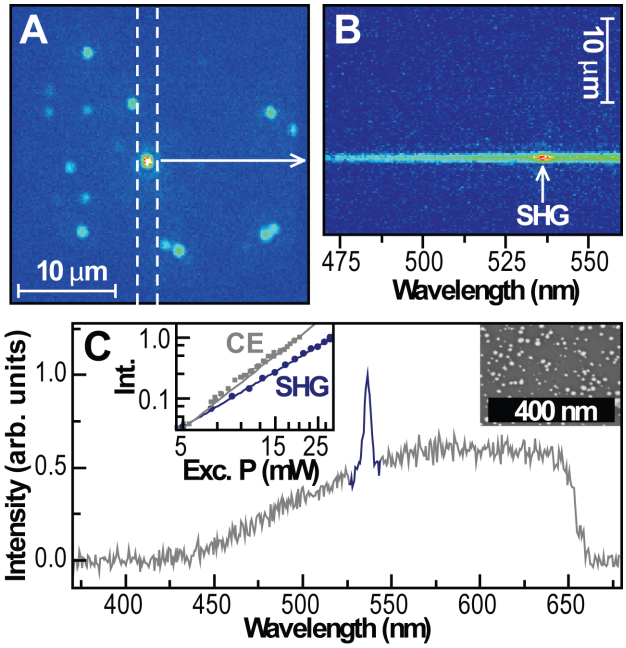

Figure 3.1. Nonlinear optical emission from a fractal silver nanoparticle film. (A) Real-space image of surface-plasmon localization and hot spot emission (seen as diffraction-limited spots) under pulsed excitation at 1070 nm. Placing a slit in the image (dashed lines) and dispersing the light through a spectrometer provides spatially resolved spectral information along the vertical axis (B). (C) Hot spot emission spectrum, truncated at 660 nm by a short-pass filter. The spectrum consists of a broad CE and a narrow peak at half the excitation wavelength which is due to SHG. A scanning electron micrograph of a typical nanoparticle sample is shown in the inset, as are the nonlinear excitation power dependencies of CE ($\propto I^{2.6}$, gray) and SHG ($\propto I^2$, blue/black).

break inversion symmetry as required for a $\chi^{(2)}$ process. SHG resulting from this nonzero interface $\chi^{(2)}$, which has been shown to occur from metal clusters as small as 1 nm [21, 22], can be enhanced by surface roughening [5]. A particle exhibiting SHG must coincide spatially with a plasmonic hot spot. Consequently, the density of optical hot spots in Fig. 3.1(A) is over 10,000 times lower than the density of silver nanoparticles seen in the inset of Fig. 3.1(C).

To probe the origin of nonlinear hot spot emission, we vary the polarization planes of the exciting laser and the detector in Figs. 3.2(A) and 3.2(B), respectively. Both excitation and emission show a high degree of linear polarization (a more complete characterization of the polarization state is provided in the supporting information (Section 3.5). In excitation, the intensity modulation of the SHG line follows that of the broad white light background. This demonstrates that both CE and SHG report on the same enhanced incident field since a hot spot will only couple to the light field of a certain polarization. However, the hot spot radiates at a different wavelength so that the polarization in emission does not report on the plasmonic enhancement, but rather on the orientation of the electronic polarization created within the hot spot. The dipolar nature of the spot emission suggests the polarizable species is situated within the hot spot which couples to the enhanced fundamental excitation field. We therefore propose that both SHG and CE arise from a small silver particle located within the hot spot region of large field enhancement, as sketched in Fig. 3.2(C).

It is important to note that $\chi^{(2)}$ of nanometer-sized metal particles actually increases with decreasing particle size due to the growing contribution of quantum chaotic rather than purely electrodynamical effects as the surface to bulk ratio rises [22]. This increase in nonlinear response counteracts the decrease of overall SHG due to the reduction in number of atoms involved [22]. In conjunction with the electric-field enhancement due to the hot spot we can therefore detect SHG from single nanometer-sized metal particles. In contrast, much larger particles, which may have significantly greater $\chi^{(2)}$, will not fit into a plasmonic hot spot and therefore appear mute in the experiment. Evidence for the presence of a small silver particle as the polarizable species in the hot spot comes from a striking spatial anticorrelation

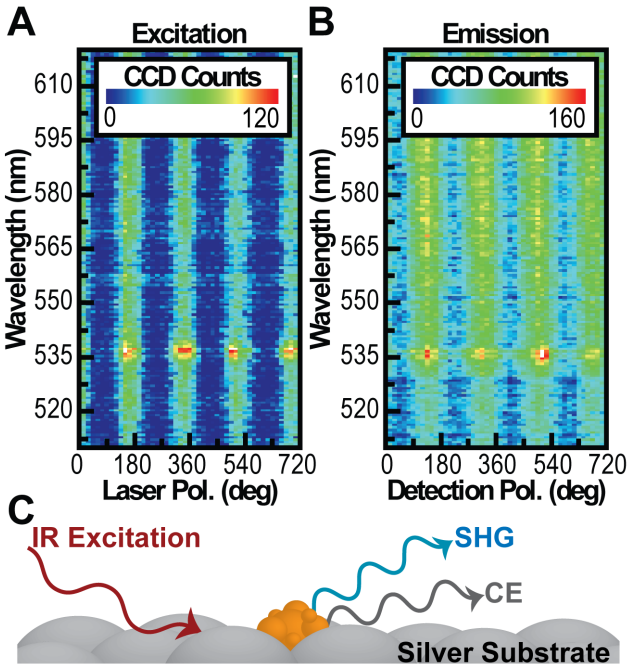

Figure 3.2. Spectrally resolved polarization anisotropy of the excitation and emission of single hot spots. (A) Modulation of the polarization of the exciting laser leads to a periodic change of both CE (broad) and SHG (537 nm) intensity (5 s time resolution). (B) The emission of the hot spot is dipolar, following a similar modulation as in excitation. (C) CE and SHG must arise from the same hot spot. We propose that the two nonlinear optical phenomena originate from a small particle located within the hot spot.

between single molecule SERS and CE [20]. We recently demonstrated that SERS preferentially occurs from hot spots which do not exhibit CE, suggesting a physical difference between hot spots responsible for CE and SERS [20]. As CE and SHG indicate the presence of a small metal particle at the focus of the hot spot, a likely origin of the SERS-CE anticorrelation is absorption of the locally enhanced optical field by the interstitial metal particle. If a particle is present in the hot spot, a single molecule will simply not fit into it: single molecule SERS cannot occur.

Remarkably, $\chi^{(2)}$ (SHG) and $\chi^{(3)}$ (CE) processes display very different physical characteristics. Figure 3.3 illustrates the temporal evolution of single-particle SHG and CE. Whereas CE is virtually constant with time, displaying two subtle jumps at 200 and 1080 s along with a gradual decrease in intensity due to photodegradation, the SHG peak fluctuates strongly in intensity. The fluctuations are reminiscent of blinking of single quantum systems [1–4], suggesting microscopic temporal variations in $\chi^{(2)}$ of the optically active nanoparticle in the hot spot. Clearly, it is not the field enhancement of the hot spot which is changing, as this would give rise to correlated intermittency of SHG and CE.We note that photoexcitation of rough silver films is known to lead to the formation and photomodification of emissive silver nanoclusters [23, 24]. The occasional jumps to higher CE intensities most likely arise from two-photon-induced growth of the silver particle in the hot spot which increases the bulk volume and thus $\chi^{(3)}$.

$\chi^{(2)}$ fluctuations do not appear to be sensitive to external perturbations. The fluctuations are not modified by temperature (between 5 and 300 K), pressure (up to atmospheric pressure), and hot spot density (controlled by the growth time of the SERS substrates). The independence of the phenomenon on pressure and temperature, and the lack of correlation between CE and SHG fluctuations, rather suggests that it is not a physical rearrangement of material in the hot spot which gives rise to SHG blinking. In addition, we did not observe any systematic change in fluctuations over an order-of-magnitude increase in excitation intensity. We conclude that the polarizable species in the hot spot must experience random variations in $\chi^{(2)}$, but not in $\chi^{(3)}$.

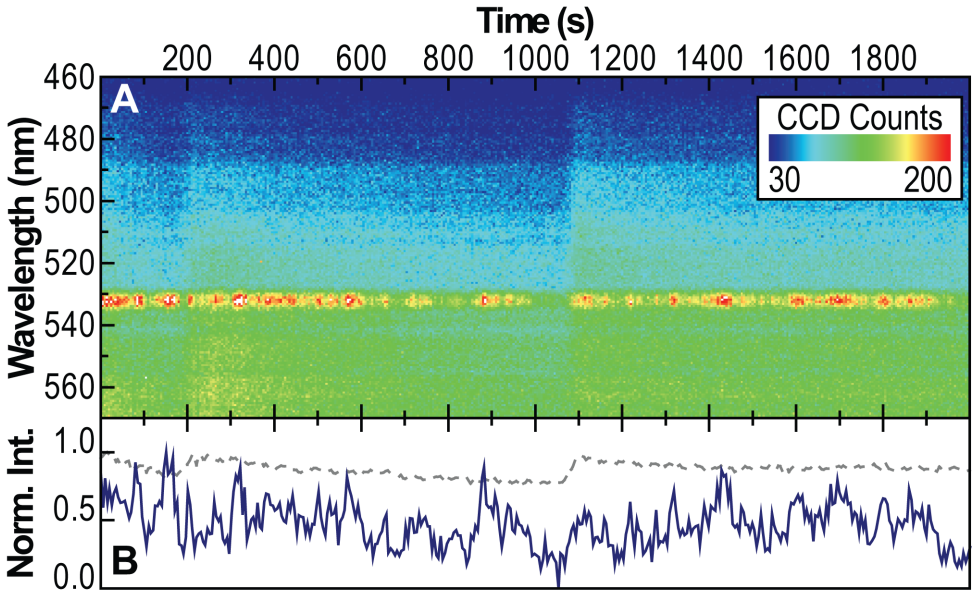

Figure 3.3. Temporal fluctuations of SHG from a single hot spot. (A) Emission trace recorded with 5 s resolution, showing that the SHG peak at 532 nm is not constant in intensity with time, reminiscent of blinking in the emission of single molecules or nanoparticles. (B) Temporal evolution of the SHG (blue/ black) and CE (gray) intensity from the same hot spot.

In contrast to $\chi^{(3)}$, $\chi^{(2)}$ only arises in materials of broken inversion symmetry. Bulk silver has a face-centered-cubic lattice with inversion symmetry. Consequently, the dipolar $\chi^{(2)}$ response of the silver nanoparticle is limited to surface SHG originating from only a few atomic layers of the silver particle where inversion symmetry is broken. On the other hand, $\chi^{(3)}$ should have significant bulk contributions. Due to the large surface to bulk ratio and the presence of discrete electronic states, small metal clusters are prone to charging, which can impact the optical [25] and transport [26] properties. Indeed, metal nanoparticles do not display purely metallic behavior on nanometer length scales, as evidenced by the absence of plasmon resonances, and may even exhibit molecular-like electronic structure with discrete rather than continuous metallic states. [25] A possible scenario for the origin of SHG blinking lies in spontaneous changes in the local charge distribution within or in the vicinity of the radiating particle. These changes will lead to a fluctuation of both the magnitude and the polarization of SHG (surface sensitive), while leaving the CE (bulk sensitive) virtually unchanged. Support for this proposition of a temporally varying charge distribution which controls $\chi^{(2)}$ comes from considerations of polarization-resolved SHG blinking. Figure 3.4 illustrates the fluctuations in hot spot emission intensity for simultaneous detection parallel and perpendicular to the polarization plane of excitation. The transient reveals uncorrelated fluctuations in the two polarization planes of the SH radiation (marked by the shaded regions in panels A and B). No strong polarization fluctuations are observed in CE (C and D). We conclude that the effective components of the $\chi^{(2)}$ tensor vary independently with time, suggesting a local rearrangement of static polarization without physical movement of the particle (which would affect CE). Localized charges on or in the vicinity of the emitting particle could account for this effect. A complete characterization of the SHG polarization state in the framework of Stokes parameters is given in the supporting information (Section 3.5) and demonstrates further subtle fluctuations in the SH radiation while the CE remains constant in time.

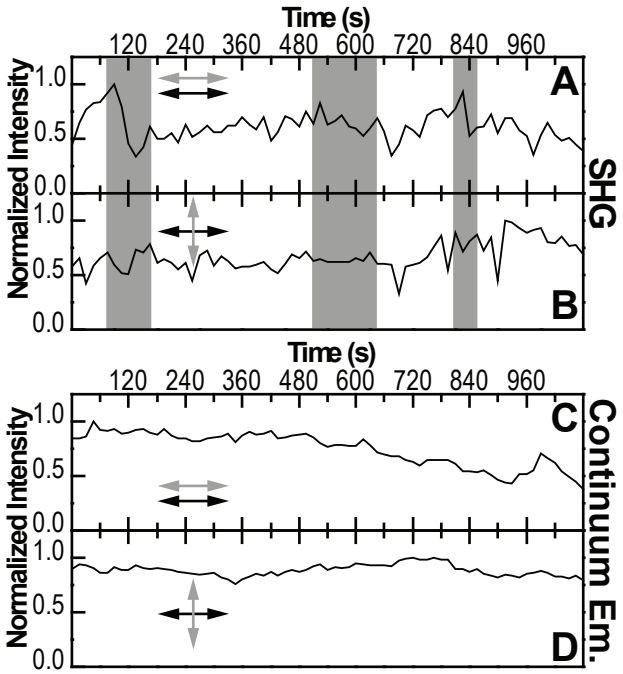

Figure 3.4. Polarization dependence of SHG intermittency and CE from a single hot spot. The parallel (A) and orthogonal (B) polarization components of SHG with respect to the incident laser polarization (black arrows) are only weakly correlated, particularly in the shaded regions (measurement resolution 10 s). The simultaneous CE does not display any substantial fluctuations in either polarization channel (C and D), besides a gradual intensity decay due to photodegradation. A complete analysis of the polarization state is given in the supporting information (Section 3.5).

3.4 Summary

SHG offers a powerful microscopic technique to image processes at interfaces [6]. As the method is applied to ever smaller objects, it is critical to realize that the nonlinear optical response can exhibit discreteness and intermittencyin analogy to blinking in luminescence [1–4]. The conceptual difference to luminescence blinking lies in the fact that luminescence requires real states, whereas scattering involves virtual levels. As such, intermittency in nonlinear light scattering constitutes an unexpected phenomenon. The observation of temporal fluctuations in spatially discrete surface-enhanced SHG illustrates that the intrinsic $\chi^{(2)}$ of a nanostructure such as a nanoparticle cannot be meaningfully quantified although it can be readily detected.

3.5 Supporting information

3.5.1 Introduction

In order to provide a more detailed analysis of the polarization of the SHG and CE from the sample, we determined Stokes parameters for several isolated hot spots. In this supplementary information the fundamentals of Stokes parameters are outlined, details on the measurement technique are provided, and the results of three individual nonlinear hot spots are discussed.

In the case of the first hot spot presented here, both SHG and CE were strong enough to analyze, and the emission of both is shown to be linearly polarized with very similar Stokes parameters. The second hot spot discussed emits predominantly SHG, and it is verified that the SHG is linearly polarized. The final hot spot analyzed emitted analyzable levels of SHG and CE. For this hot spot, the measurement shows the CE to be linearly polarized as expected but yields meaningless and unphysical values for the Stokes parameters for the SHG. The unreasonable Stokes parameters for the SHG arise from the $\chi^{(2)}$ variation and subsequent polarization fluctuations over the course of the measurement and serve as a further example of the inherent complexity of using SHG to accurately characterize nanoscale systems.

3.5.2 Stokes parameters

An electromagnetic plane wave with a defined polarization can be mathematically represented as:

$$\boldsymbol{E}(t) = E_x \cos(\omega t)\hat{\boldsymbol{x}} + E_y \cos(\omega t + \delta)\hat{\boldsymbol{y}} \tag{3.1}$$

where δ is the phase difference between the X and Y components of the polarization.

The Stokes formalism quantitatively describes the polarization state of light for states ranging continuously from completely polarized to completely unpolarized. The method defines four parameters, S_0, S_1, S_2, and S_3. These parameters are referred to as the Stokes parameters and completely characterize the polarization state. The parameters are often treated, although not in a strict mathematical sense, as a four-vector and are defined as follows for a plane wave [27]:

$$\begin{pmatrix} S_0 \\ S_1 \\ S_2 \\ S_3 \end{pmatrix} = \begin{pmatrix} E_x^2 + E_y^2 \\ E_x^2 - E_y^2 \\ E_x E_y \cos(\delta) \\ E_x E_y \sin(\delta) \end{pmatrix}. \tag{3.2}$$

Each Stokes parameter represents a different polarization contribution to the overall polarization state. S_0 is a measure of the total intensity of the plane wave. S_1 describes the amount of light that is linearly polarized in the vertical or horizontal plane. S_2 then describes the amount of light that is linearly polarized at $45°$ or $-45°$ to the horizontal. Finally, S_3 describes the amount of light that is left-handed (LH) or right-handed (RH) circularly polarized.

Following from the above definitions, the Stokes parameters are constrained such that

$$S_0^2 \geq S_1^2 + S_2^2 + S_3^2. \tag{3.3}$$

If the analyzed light is completely polarized (linearly or circularly), the equality of Equation 3.3 holds. Furthermore, the Stokes parameters can be used to express the degree of polarization, P, of the analyzed light:

$$P = \frac{(S_1^2 + S_2^2 + S_3^2)^{1/2}}{S_0},\ 0 \leq P \leq 1. \tag{3.4}$$

Following from Equation 3.3 $P = 1$ for completely polarized light (again linearly or circularly); and for completely unpolarized light, $P = 0$. If the light is partially polarized, the value of P falls between the values 0 and 1.

3.5.3 Measurement technique

The measurement technique and setup used is referred to as a rotating wave plate Stokes' polarimeter [28] and is described in detail in [27]. The experimental setup used is pictured in Figure 3.5. Since Stokes parameters are measured in reference to a specific coordinate system, one system must be defined. In the measurements discussed here, the coordinate system is fixed such that the emitted sample radiation is traveling in the positive z-direction, and the x-axis is defined with the polarization axis of the linear polarizer which is aligned parallel to the horizontally polarized

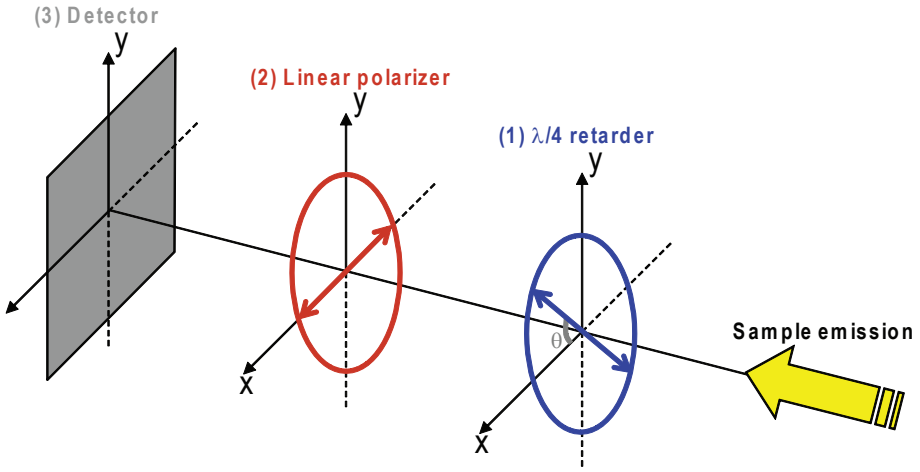

Figure 3.5. Schematic sketch of the experimental setup for determining the Stokes parameters in emission. Light from the sample travels from right to left and passes through (1) a $\lambda/4$ retarder (Newport achromatic zero-order Quartz-MgF_2 wave plate) mounted on a rotation stage such that its fast axis (marked on the figure) can be rotated with respect to the x-axis of the system. Then the light passes through (2) a linear polarizer (Newport high precision linear polarizer) with its polarization axis fixed parallel to the excitation laser. Finally, light intensity is measured by a detector (3) which is a CCD (Princeton Instruments) fixed to an imaging spectrometer.

excitation laser. Positive x- and y-directions are chosen such that a right-handed coordinate system is used.

To measure the Stokes parameters with the described setup, the intensity of the emitted light reaching the detector, $I(\theta)$, is recorded as a function of the angle between the x-axis and the fast axis of the $\lambda/4$ retarder, θ . This method has the advantage of always measuring the same polarization at the detector which eliminates the need to correct for any polarization dependence of the detector. In terms of the Stokes parameters of the sample emission, the intensity at the detector is [27]:

$$I(\theta) = \frac{1}{2}\left[\left(S_0 + \frac{S_1}{2}\right) + \frac{S_1}{2}\cos(4\theta) + \frac{S_2}{2}\sin(4\theta) - S_3\sin(2\theta)\right]. \tag{3.5}$$

One method of extracting the Stokes parameters is by fitting Equation 3.5 to the measured data. Additionally, it is worth nothing that Equation 3.5 is a truncated Fourier series. Consequently, the values of S_0, S_1, S_2, and S_3 can be isolated and extracted with a simple Fourier analysis [28]:

$$
\begin{aligned}
S_0 &= \frac{1}{\pi}\left[\int_0^{\pi} I(\theta)\,d\theta - 2\int_0^{2\pi} I(\theta)\cos(4\theta)\,d\theta\right] \\
S_1 &= \frac{4}{\pi}\int_0^{2\pi} I(\theta)\cos(4\theta)\,d\theta \\
S_2 &= \frac{4}{\pi}\int_0^{2\pi} I(\theta)\sin(4\theta)\,d\theta \\
S_3 &= -\frac{2}{\pi}\int_0^{2\pi} I(\theta)\sin(2\theta)\,d\theta.
\end{aligned} \tag{3.6}
$$

All of the Fourier analysis integrals are calculated using the trapezoidal integration method [29]. Using the Fourier analysis instead of fitting to Equation 3.5 is advantageous because it does not require exact alignment of the $\theta = 0$ position of the fast axis of the $\lambda/4$ retarder with the polarization axis of the linear polarizer; since the Fourier analysis integrates over an integral number of periods of the integrand, a constant offset of θ from 0 does not affect the results.

All of the Stokes parameters reported here are normalized such that S_0 is equal to 1. Furthermore, whenever the raw data are compared to Equation 3.5 in the figures, the data are also normalized by S_0 in the same manner.

To verify the accuracy of the system, the polarization of the excitation laser was analyzed for a variety of different cases. Figure 3.6 shows the test case where a linear

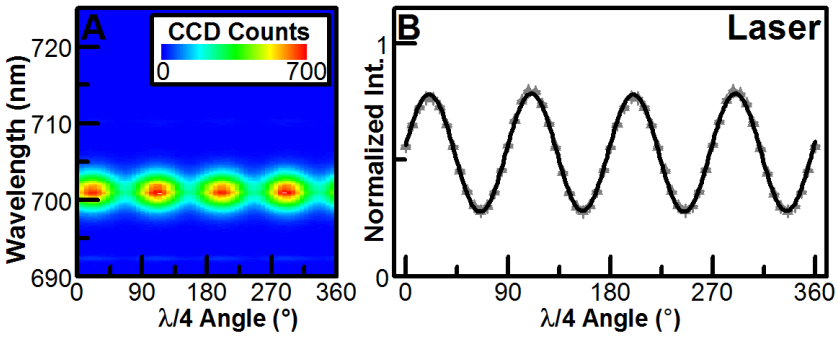

Figure 3.6. Stokes characterization of the linearly polarized excitation laser oriented ~45° above the positive x-axis. The raw data (A) are shown alongside the normalized peak heights (B) overlaid with a plot of Equation 3.5 with the extracted Stokes values from the Fourier analysis.

polarizer was used in conjunction with the horizontally polarized laser to generate linearly polarized light oriented at 45° with respect to the positive x-axis. Panel A shows the raw data, while Panel B shows the extracted peak heights of the laser intensity as a function of the $\lambda/4$ orientation overlaid with Equation 3.5. The S_0, S_1, S_2, and S_3 values used were extracted with the Fourier analysis.

The calculated Stokes parameters from the Fourier analysis are $S_0 = (1.000 \pm 0.001)$, $S_1 = (0.126 \pm 0.001)$, $S_2 = (0.999 \pm 0.002)$ and $S_3 = (0.005 \pm 0.001)$. These results agree well with the expected $(1, 0, 1, 0)$ results. The deviation of S_1 from 0 is attributed to slight misalignment of the initial linear polarizer resulting in a slight deviation of the laser polarization away from the assumed orientation. The ability to accurately measure a variety of polarization states such as horizontally polarized light as well as LH and RH circularly polarized light was also verified.

3.5.4 Stokes parameters of CE and SHG from a single hot spot

Shown in Figure 3.7 is the Stokes characterization measurement of a hot spot that emits both SHG and CE. 3.7a shows the raw data where it is immediately clear that the SHG and CE both modulate a similar manner with respect to the $\lambda/4$ retarder orientation. 3.7b and 3.7c show the CE and SHG intensities, respectively, as a function of the $\lambda/4$ retarder orientation angle. Comparing 3.7b to 3.7c confirms that the SHG and CE have very similar dependence on the orientation of the $\lambda/4$ retarder. Using Fourier analysis to calculate the Stokes parameters and degree of polarization for both the CE and SHG yields the results in Table 3.1.

Table 3.1. The Stokes parameters of a hot spot emitting CE and stable SHG.

Stokes Parameter	**CE**	**SHG**
S_0	1.00 ± 0.01	1.00 ± 0.06
S_1	-0.44 ± 0.02	-0.36 ± 0.10
S_2	0.78 ± 0.02	1.07 ± 0.10
S_3	0.37 ± 0.01	0.11 ± 0.05
P	0.97	1.13

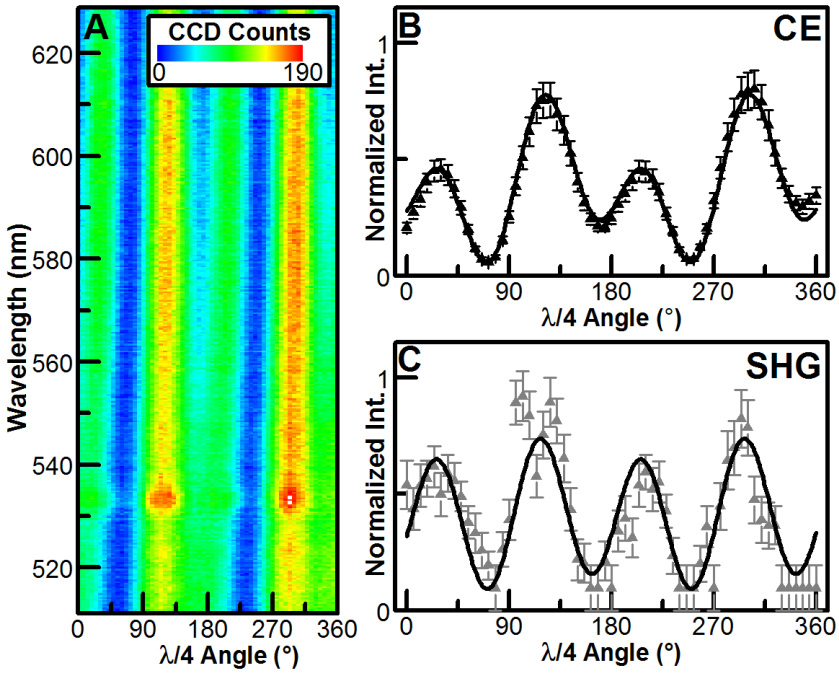

Figure 3.7. Stokes characterization of CE and SHG from a silver nanoparticle hot spot emitting both SHG and CE. The raw data (A) are shown alongside the extracted CE (B) and SHG (C) intensities. Overlaid in (B) and (C) are the plots of Equation 3.5 with the Stokes parameters calculated from the Fourier analysis of the CE and SHG signals, respectively.

There is reasonable agreement between the Stokes parameters and the degree of polarization of the SHG and the CE signals. We attribute the disagreement in the S_2 and S_3 values of the SHG and CE to the difference in the signal to noise ratio. A fit to the SHG curve using the Stokes parameters from the CE is almost statistically indistinguishable from the fit using the SHG Stokes parameters from the Fourier analysis. Within the limits of the measurement, we therefore conclude that in this case the SHG and CE are both, to a large degree, linearly polarized in the same direction. The Stokes parameters for both SHG and CE are essentially the same which further supports our assertion that the SHG and CE arise from the same species.

3.5.5 Stokes parameters of SHG hot spot with minimal CE emission

Figure 3.8 shows the Stokes characterization results of a nonlinear hot spot that predominantly emits SHG. Again, 3.8a shows the raw data of the characterization, and 3.8b resolves the SHG peak height as a function of the $\lambda/4$ retarder orientation angle. It should be noted and can be observed from the raw data in 3.8a that the hot spot also emits a very weak CE signal. However, the CE signal is too weak to accurately analyze. From the Fourier analysis method, the Stokes parameters for the SHG are reported in Table 3.2.

Shown as the solid line overlaying the data points in 3.8b is Equation 3.5 plotted with the aforementioned parameters indicating reasonable agreement of the curve with the data. The resulting polarization of this hot spot calculated with Equation 3.4 is $P = 0.89$ which, along with the Stokes parameters themselves, further verifies

Table 3.2. The Stokes parameters of a nonlinear hot spot emitting only stable SHG

Stokes Parameter	**SHG**
S_0	1.00 ± 0.03
S_1	-0.30 ± 0.05
S_2	-0.81 ± 0.05
S_3	-0.22 ± 0.05

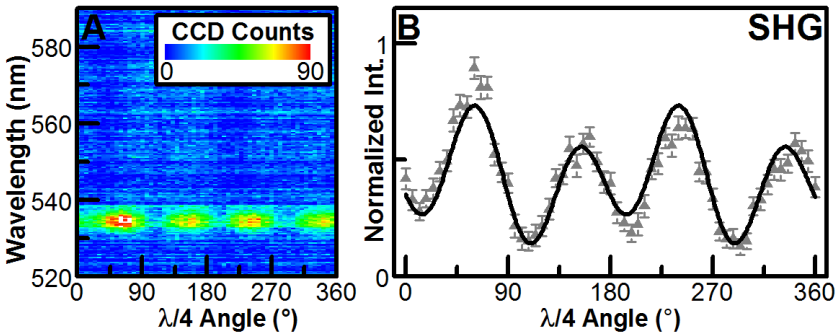

Figure 3.8. Stokes characterization of a nonlinear hot spot emitting predominantly SHG. The raw data (A) are shown with the extracted SHG intensities (B). Overlaid in (B) is the plot of Equation 3.5 with the Stokes parameters calculated from the Fourier analysis of the SHG intensity.

that SHG from the hot spots is primarily linearly polarized.

3.5.6 Extraction of unphysical Stokes parameters for SHG due to fluctuations

Shown in Figure 3.9 is the Stokes characterization measurement of a nonlinear hot spot that is exhibiting both SHG and CE. The integrated CE shown in figure 3.9b shows a clear modulation with the $\lambda/4$ retarder. Additionally, an SHG peak can be accurately detected and analyzed for each orientation of the $\lambda/4$ retarder. The SHG intensity is shown in Figure 3.9c. Fourier analysis of the CE and SHG intensities gives the Stokes parameters in Table 3.3. The Stokes parameters for the CE yield a polarization of $P = 0.81$ indicating, as expected, that the CE is linearly polarized. On the other hand, the Stokes parameters for the SHG yield unphysical results if the polarization state of the SHG is assumed to be static over the course of the measurement. The unreasonably large value of S_1 results in an abnormally large and unphysical polarization value $P = 1.53$.

As previously noted, for each $\lambda/4$ orientation the SHG intensity can be accurately measured. Furthermore, the CE result is consistent with the previous two hot spots discussed. Consequently, the unphysical result cannot be attributed to an error in the calculation or the measurement. Rather, the unphysical result arises because, in

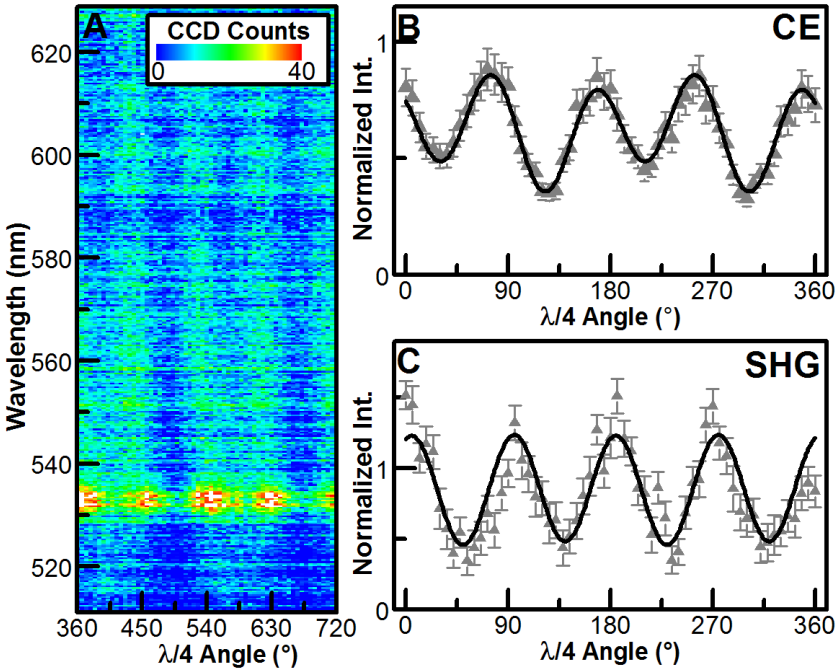

Figure 3.9. Stokes characterization of a nonlinear hot spot emitting both SHG and CE under the case where the SHG is fluctuating. The raw data (A) are shown as well as the extracted CE (B) and SHG (C) intensities. Overlaid in both (B) and (C) is a plot of Equation 3.5 with the respective Stokes parameters extracted from the Fourier analysis.

Table 3.3. The Stokes parameters of a nonlinear hot spot emitting CE and fluctuating SHG.

Stokes Parameter	CE	SHG
S_0	1.00 ± 0.02	1.00 ± 0.07
S_1	0.49 ± 0.03	1.42 ± 0.12
S_2	-0.63 ± 0.03	0.57 ± 0.12
S_3	-0.14 ± 0.01	0.03 ± 0.06

general, the polarization of the SHG fluctuates due to the $\chi^{(2)}$ fluctuations as shown in Figure 3.4. Such fluctuations will adversely affect attempts to accurately characterize the SHG emission because during the course of the analysis where the emission state is expected to remain constant, the state actually fluctuates. Consequently, inaccurate or even unreasonable characterization values (Stokes parameters) become a significant hurdle to reliably using SHG as a nanoscale characterization method.

3.6 Acknowledgments

We are grateful to the Petroleum Research Fund Grant No. 46795 and the National Science Foundation Grant No. 0748473 for financial support, as well as to the David & Lucile Packard Foundation. We thank R. Polson for assistance in acquiring the SEM image.

3.7 References

[1] R. J. Cook and H. J. Kimble, Phys. Rev. Lett. **54**, 1023 (1985).

[2] W. Nagourney, J. Sandberg, and H. Dehmelt, Phys. Rev. Lett. **56**, 2797 (1986).

[3] T. Basché, S. Kummer, and C. Bräuchle, Nature **373**, 132 (1995).

[4] M. Nirmal et al., Nature **383**, 802 (1996).

[5] V. M. Shalaev, *Nonlinear Optics of Random Media: Fractal Composites and Metal Dielectric Films*, Springer, Berlin, 2000.

[6] Y. R. Shen, Nature **337**, 519 (1989).

[7] M. Moskovits, *Surface-Enhanced Raman Scattering: Physics and Applications*, pages 1–18, Springer, Berlin, 2006.

[8] S. Nie and S. R. Emory, Science **275**, 1102 (1997).

[9] K. Kneipp et al., Phys. Rev. Lett. **78**, 1667 (1997).

[10] J. N. Anker et al., Nat. Mater. **7**, 442 (2008).

[11] A. Weiss and G. Haran, J. Phys. Chem. B **105**, 12348 (2001).

[12] H. X. Xu, E. J. Bjerneld, M. Kall, and L. Borjesson, Phys. Rev. Lett. **83**, 4357 (1999).

[13] A. M. Moran, J. Sung, E. M. Hicks, R. P. Van Duyne, and K. G. Spears, J. Phys. Chem. B **109**, 4501 (2005).

[14] C. Anceau, S. Brasselet, J. Zyss, and P. Gadenne, Opt. Lett. **28**, 713 (2003).

[15] A. Bouhelier, M. Beversluis, A. Hartschuh, and L. Novotny, Phys. Rev. Lett. **90**, 013903 (2003).

[16] M. I. Stockman, Chem. Phys. **318**, 156 (2005).

[17] S. I. Bozhevolnyi, J. Beermann, and V. Coello, Phys. Rev. Lett. **90**, 197403 (2003).

[18] P. Zolotavin et al., Chem. Phys. Lett. **457**, 342 (2008).

[19] Z. Wang, S. Pan, T. D. Krauss, H. Du, and L. J. Rothberg, Proc. Natl. Acad. Sci. **100**, 8638 (2003).

[20] M. J. Walter et al., Phys. Rev. Lett. **98**, 137401 (2007).

[21] J. I. Dadap, J. Shan, K. B. Eisenthal, and T. F. Heinz, Phys. Rev. Lett. **83**, 4045 (1999).

[22] O. A. Aktsipetrov, P. V. Elyutin, A. A. Nikulin, and E. A. Ostrovskaya, Phys. Rev. B **51**, 17591 (1995).

[23] C. D. Geddes, A. Parfenov, I. Gryczynski, and J. R. Lakowicz, J. Phys. Chem. B **107**, 9989 (2003).

[24] L. A. Peyser, A. E. Vinson, A. P. Bartko, and R. M. Dickson, Science **291**, 103 (2001).

[25] P. V. Kamat, J. Phys. Chem. B **106**, 7729 (2002).

[26] A. Zabet-Khosousi and A. A. Dhirani, Chem. Rev. **108**, 4072 (2008).

[27] D. Goldstein, *Polarized Light*, Marcel Dekker, Inc., New York, 2003.

[28] C. Flueraru, S. Latoui, J. Besse, and P. Legdendre, IEEE Trans. Instrum. Meas. **57**, 531 (2008).

[29] W. H. Press, S. A. Teukolsky, W. T. Vetterling, and B. P. Flannery, *Numerical Recipes in C: The Art of Scientific Computing*, Cambridge University Press, New York, 1992.

CHAPTER 4

SURFACE-ENHANCED LIGHT EMISSION FROM SINGLE HOT SPOTS IN FRACTAL SILVER NANOPARTICLE FILMS

The rough silver films produced from the Tollens reagent reaction are forefront candidates for providing facile and reproducible single molecule surface-enhanced Raman scattering (SERS). Despite their recent successes, however, SERS analysis using these and similar metallic systems is still plagued by contamination, a broad background signal, and strong fluctuations. In this chapter, the *intrinsic* optical properties of the Tollens mirrors are comprehensively studied using linear and nonlinear optical excitation. Consideration of the obtained properties leads to a physical model of the optical hot spots with significant relevance to improving the understanding and quality of SERS measurements that utilize silver at visible to infrared excitation energies.

This chapter was coauthored with John M. Lupton and was submitted to the Journal of the American Chemical Society in early February of 2011.

4.1 Abstract

The optical properties of fractal silver films grown using the Tollens silver mirror reaction enable highly reproducible single molecule surface-enhanced Raman scattering (SERS). These characteristics are a result of the nanostructure morphology which supports strongly localized surface plasmon polariton excitations that dramatically enhance the incident electromagnetic field in nanoscale regions called hot spots. Besides SERS, the local field amplification enhances an array of other linear and nonlinear optical effects such as silver luminescence, and second-harmonic and continuum generation. By varying film growth conditions, we establish that the

intrinsic linear and nonlinear responses qualitatively correlate with film morphology in the same manner as reported for SERS. We probe the polarization anisotropy, polarization memory, power dependence, emission spectra, excitation wavelength and temperature dependence, blinking, spectral diffusion, and emission decay dynamics of both hot spot species. Striking similarities and important differences exist between linear and nonlinear excitation: for example, the anisotropy distributions in excitation reveals a common surface enhancement process, whereas contrasting photodynamics clearly differentiate the two emission processes. Nonlinear hot spots do not blink, whereas linear hot spots exhibit strong blinking. We propose that the results can be understood by considering structure formation beyond the dimensions resolvable with scanning electron microscopy: the larger particles give rise to the surface enhancement phenomena, and smaller particles and clusters lead to the diverse emission properties. The existence of such silver clusters in a hot spot immediately impacts SERS, since it effectively blocks all other surface amplification processes, such as SERS of an analyte molecule, leading to spatial anticorrelation between light generation and SERS. Applications of the intrinsic optical response for SERS as well as high-resolution transmission microscopy are discussed.

4.2 Introduction

Fractal arrangements of silver nanoparticles are uniquely posed to enhance the coupling of light and matter to such an extent that Raman scattering from single molecules becomes possible [1–15]. Single molecule surface-enhanced Raman scattering (SERS) is the ultimate analytical technique in that one individual molecule can be identified at a time by its unique vibrational fingerprint. The greatest strength of single molecule SERS is also its most significant drawback: amplification of the incident light field is both local and nonspecific, so that minuscule concentrations of contaminants in the vicinity of the analyte can significantly perturb the far-field spectroscopic signal [6, 9]. Although highly reproducible single molecule SERS has been demonstrated, most recently with applications to the field of organic electronics [10, 11], widespread exploitation of these high levels of surface enhancement

requires a precise understanding of both the nature of nanoparticle aggregates and the underlying linear, and nonlinear, optical response [16–22]. A fractal film that enhances the incident light field [18–20, 23, 24, 24, 25] to enable single molecule SERS will also amplify other optical phenomena [26]. For example, metal nanoparticles and clusters are known to luminesce [27–42], an effect that can be dramatically increased by the surface enhancement phenomenon [29, 43, 44]. In addition, the increased excitation fields lead to a pronounced magnification of the nonlinear optical response [16–20, 45, 46], which gives rise to spatially discrete emission of white light from regions of the aggregate film with particularly large surface enhancement [25]. These emissive regions are often referred to as hot spots [20, 24, 25, 47, 48].

Although the optical properties of metal films have been investigated for decades [26, 49–51], advances in experimental techniques – in terms of both fabrication and characterization – continuously yield new surprises. Obvious questions arising from the study of the optical properties of metals address the relation between different optical features: a bulk metal film, such as gold, can exhibit extremely weak fluorescence [52, 53], but also support surface plasmon polaritons which enable the propagation of light energy through the metal [54]. How does the fluorescence observed relate to the characteristics of the plasmons? How do linear optical processes, such as fluorescence, relate to nonlinear processes such as second-harmonic generation (SHG)? In addition to fundamental questions in the physics and chemistry of the light-matter interaction, these extraordinary enhancement phenomena arising from plasmonic excitation in metals have significant relevance to the life sciences, materials science, and analytical chemistry through SERS and other novel applications [55]. For example, we recently demonstrated that the extraordinary stability in nonlinear light emission can be exploited in a new form of optical transmission microscopy, in which silver nanoparticles serve as subdiffraction beacons of spectrally broad light [56]. Thus, close inspection of the optical properties of nanostructured metals is not only merited but required: the greater the overall pool of information available that describes the complete optical characteristics, the more likely substantial advances in actual applications will be made.

Silver nanoparticle mirrors, based on the Tollens reagent reaction, are particularly facile in their fabrication [57] yet remarkably versatile in their ability to reveal single molecule Raman scattering [58–60], especially at cryogenic temperatures [10, 11]. Previously, we provided unambiguous evidence for the occurrence of single molecule SERS by correlating the spectral dynamics of single molecule luminescence with the resonance enhancement in SERS [11]. In a following study, we demonstrated that a surprising spatial anticorrelation exists between positions on the nanoparticle substrate from which nonlinear light emission is observed, and those locations at which high-resolution single molecule SERS occurs at visible excitation [10]. Such an anticorrelation serves as a potential quality screening technique for SERS substrates. However, the relationship between the intrinsic optical response of the Tollens silver films and their SERS properties have yet to be comprehensively studied or established, thus limiting a thorough understanding of how results obtained from the intrinsic optical response connect back to SERS. In this article, we thoroughly investigate the intrinsic linear and nonlinear emission observed from rough silver films. Our foremost aims are to relate morphological features to these far-field optical signatures, and then to assess the resulting implications for SERS. This approach promises to dramatically simplify sample characterization. First of all, we are able to qualitatively correlate the surface morphology, as determined by scanning electron microscopy (SEM), with the density and intensity of discrete emission spots observed under pulsed IR and visible radiation illumination of the sample. We thereby establish a relationship to surface enhancement for both processes. We then pick a specific morphology, and probe a large set of emission properties of both the linear and nonlinear hot spots, documenting the similarities and differences between the two species. The properties probed include single hot spot excitation power dependence; single hot spot emission and excitation polarization anisotropy; single hot spot emission spectra; excitation wavelength dependence; single hot spot blinking and spectral diffusion; emission decay; and finally, temperature dependence. The linear and nonlinear emission show striking similarities due to common excitation pathways and significant differences due to distinctly different emission processes. Detailed and inclusive consideration of

the host of emission properties for both processes leads us to a physical model that may have important implications for SERS.

The physical model of silver nanoparticle films that has evolved from our considerations is based on smaller, luminescent silver nanoclusters [27, 32, 37, 61–63] being situated within plasmonic hot spots. These nanoclusters can emit either by excitation through linear absorption to an electronic state or by nonlinear scattering from a virtual state [64]. Importantly, when a nanocluster sits within a plasmonic hot spot, enhancement of the light-matter interaction with nearby molecules is effectively blocked [10]. The silver cluster has a larger polarizability than the adjacent molecule and may therefore absorb a significant amount of the radiation from the hot spot in addition to potentially modifying its chemical nature. Under nonlinear excitation, this enhancement attenuation is suspected to lead to the spatial anticorrelation between single molecule SERS and white light emission [10]. Thus the linear and the nonlinear optical response of single hot spots in fractal metal films may ultimately provide a route to extrapolating physical information on the arrangement of matter within the hot spots at nanometer length scales, beyond what is presently detectable with high-resolution scanning electron microscope (SEM) techniques. After reviewing the key experimental features of our experiment, we compare the elementary optical properties of silver nanoparticle hot spots under linear and nonlinear excitation. We then develop the hypothesis of emissive silver clusters, discuss their implications for SERS, and conclude that optical microscopy helps illuminate our understanding of these remarkably complex forms of matter. New analytical routes are then suggested for improving the applicability, versatility, and understanding of SERS techniques, especially at the single molecule level.

4.3 Experimental

Tollens substrates were fabricated following the procedure described by Saito *et al.* [57] and Wang *et al.* [58]. Briefly, a silver nitrate-based reagent solution and a glucose solution were separately prepared in ultrapure water. The two solutions were then mixed together causing the glucose to reduce the reagent and deposit

silver on any glass surfaces in contact with the reaction. Cleaned glass cover slips were immersed in the reaction for a set duration (typically between 45 s and 300 s, depending on desired surface coverage) to allow macroscopically uniform deposition of silver on the entire substrate. The samples were mounted in a microscope cryostat at room temperature, under a vacuum of $\sim 10^{-6}$ mbar. Performing the experiments under vacuum drastically enhances photostability, which is crucial for time, power, wavelength and polarization dependent studies. In contrast, as far as we are aware, most prior investigations into the linear and nonlinear optical effects of these intriguing materials were performed under atmospheric conditions. A tunable pulsed Ti:Sapphire laser (140 fs pulse length, 80 MHz repetition rate) operating at the fundamental (between 680 nm and 1080 nm) or the second harmonic (340 nm to 540 nm) was used as the excitation source. The laser light was focused to a spot approximately 40 μm in diameter, incident at an angle of $\sim 30^{\circ}$ with respect to the substrate normal. Similar to traditional dark-field microscopy [65], light was collected in the normal direction of the sample using a long working-distance microscope objective lens (numerical aperture 0.55), passed through an appropriate set of filters to block scattered excitation light, and then analyzed with a 50 cm imaging spectrograph attached to a back-illuminated charge-coupled device (CCD) camera. Time-resolved emission decay measurements were conducted with a Hamamatsu streak camera with $\sim$4 ps resolution operating in synchroscan mode at a repetition rate of 80 MHz.

Optical hot spots are observed from the silver substrates both under pulsed excitation in the IR [25], or under pumping in the visible to UV spectral region [34]. In the case of IR excitation, short-pass emission filters were chosen to observe the light radiated from the sample at higher energy than the excitation. Under visible/UV excitation, long-pass filters were employed to monitor the emission at energies *below* the excitation. Figure 4.1 displays a typical dataset recorded from a Tollens silver mirror. Panel a) shows a real-space microscope image of the light emission from the mirror under excitation at 912 nm (10 W/cm^2 c.w. intensity). Light emission from discrete spots is observed on a dark background. The spots are diffraction-limited as indicated by the circular patterns surrounding them. Closing the slit of the

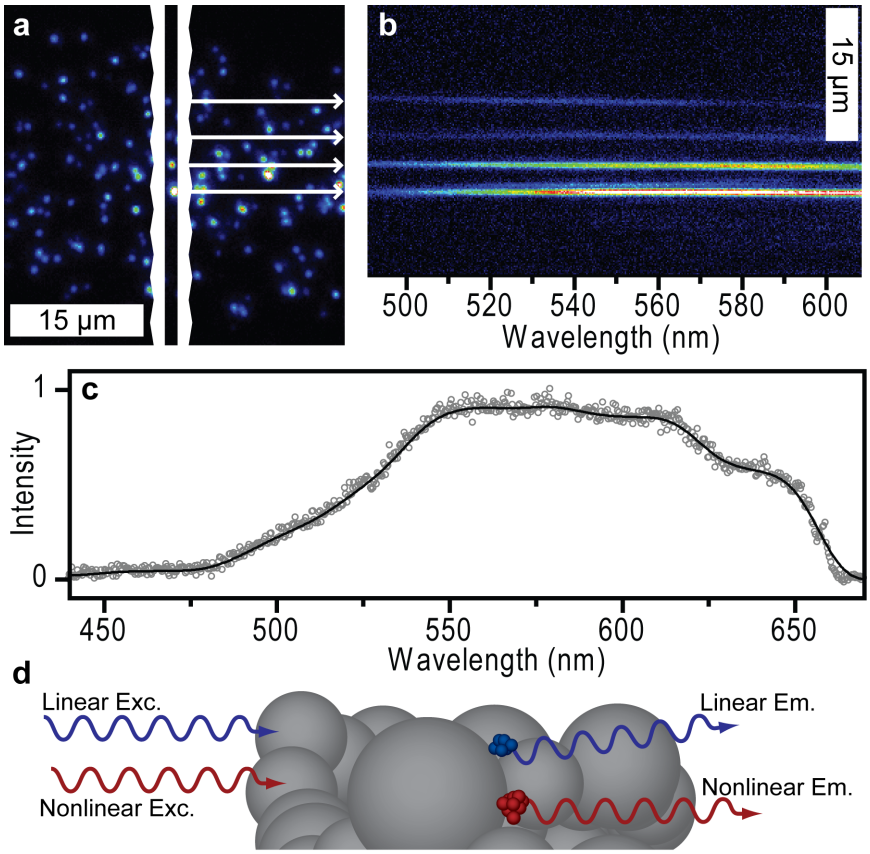

Figure 4.1. Optical spectroscopy of single hot spots formed on rough silver films. a) In this case, under illumination with pulsed IR radiation from the laser at 912 nm, discrete diffraction-limited spots are observed under the optical microscope. The corresponding spectrum of a spot can be resolved by closing a slit (white markers) onto one of the spots and dispersing the radiation in a spectrometer as shown in panel b). The vertical spatial information in the microscope image is retained. c) The corresponding spectrum of a single hot spot emitting at higher energies than the excitation energy. d) Observation of light emission from the silver film requires both an enhancement process of the interaction with the incident and radiated electromagnetic field, provided by collective surface plasmon resonances of the metal nanoparticles in the rough silver film; and the presence of a polarizable species within this hot spot. We propose that a small silver cluster sits within the plasmonic hot spot, giving rise to the emission observed.

spectrometer so that only one bright spot is present in the space confined by the horizontal dimension of the slit, and dispersing the light on a suitable grating in a monochromator, allows the emission spectrum of the single spot to be recorded. While the horizontal positional information is lost, the vertical information is retained, as illustrated in panel b). Panel c) displays a typical hot spot emission spectrum. The spectrum is cut off at 650 nm due to the short-pass filter employed to remove the incident IR laser. A broad, virtually featureless spectrum is observed, which drops to zero just below 450 nm. This emission is often referred to as white light continuum, as it covers the entire visible spectrum [66]. Under certain conditions the second harmonic of the incident laser radiation is observed due to surface-enhanced SHG [20, 25, 50, 67–71]. We have recently reported on the unique characteristics of hot spot SHG from Tollens substrates, most importantly the remarkable observation of SHG blinking [72]. In this contribution we will be focusing on the properties of the white light continuum. It remains to be noted that the total spectral intensity of the SHG peak at most accounts for 1 % of the entire emission spectrum under the excitation conditions considered here.

The Tollens films are thought to be fractal in nature with regard to their root mean square roughness [58] and contain arrangements of silver particles down to length scales at which the silver ceases to be metallic. Such small silver clusters can exhibit molecular-like electronic characteristics [27, 64, 73]. In this article we will summarize evidence for the role of discrete species whose interaction with the light field is enhanced by adjacent nanoparticle aggregate plasmons. It is illustrative to picture the arrangement of ever smaller nanoparticles as shown in Figure 4.1d). We stress that this figure remains a conjecture, which is not straightforward to test; present preparation techniques do not allow for controlled placement of miniscule emissive metal clusters of the size of a few tens to hundreds of atoms in self-similar nanoparticle aggregates of varying dimensions.

4.4 Results

4.4.1 Optical hot spots: the effect of surface coverage

We begin by discussing the elementary optical properties of a series of Tollens silver mirrors grown with different reaction times. Figure 4.2 summarizes six different substrates of growth times ranging from 45 s to 270 s. From left to right a photograph of the mirror is shown, followed by a SEM image, and the fluorescence microscope images under linear (456 nm) and nonlinear multiphoton (912 nm) excitation. Note that the luminescence images were not all recorded at the same detection intensity level. Under illumination from a standard incandescent light, the photographs show that as the growth time increases, the silver mirror changes color and becomes more metallic: for short growth times, the film appears gold-brownish. Bright spots in the photographs arise from particularly strongly reflecting regions on the substrate, possibly areas with accelerated nucleation of silver. As the growth time increases, the surface coverage increases, as seen in the SEM images. Whereas nanoparticles down to 2 nm in size can be made out in the 45 s substrate, the particles begin to fuse with increasing incubation time, leading to larger and larger structures. Nevertheless, small particles of a few nanometers in diameter can still be made out up to a growth time of 225 s.

The maximum enhancement of the electric field occurs at interstitial sites between different nanoparticles [74]. As the density of nanoparticles increases, the number of interstitial sites consequently rises, until the particles begin to fuse. From this perspective, the density of interstitial sites in the 270 s substrate is comparable to that in the 45 s substrate. The density of optical hot spots for both the emission observed under one and under multiphoton excitation clearly scales with this density of interstitial sites, as seen in the third and fourth column of the figure. Typically, we observe significantly more background in the microscope images under one-photon excitation than under multiphoton pumping. However, the fact that the occurrence of optical emission hot spots depends so clearly on substrate coverage provides the first indication that both linear and nonlinear light emission arise from a surface enhancement effect, involving collective nanoparticle plasmon excitations.

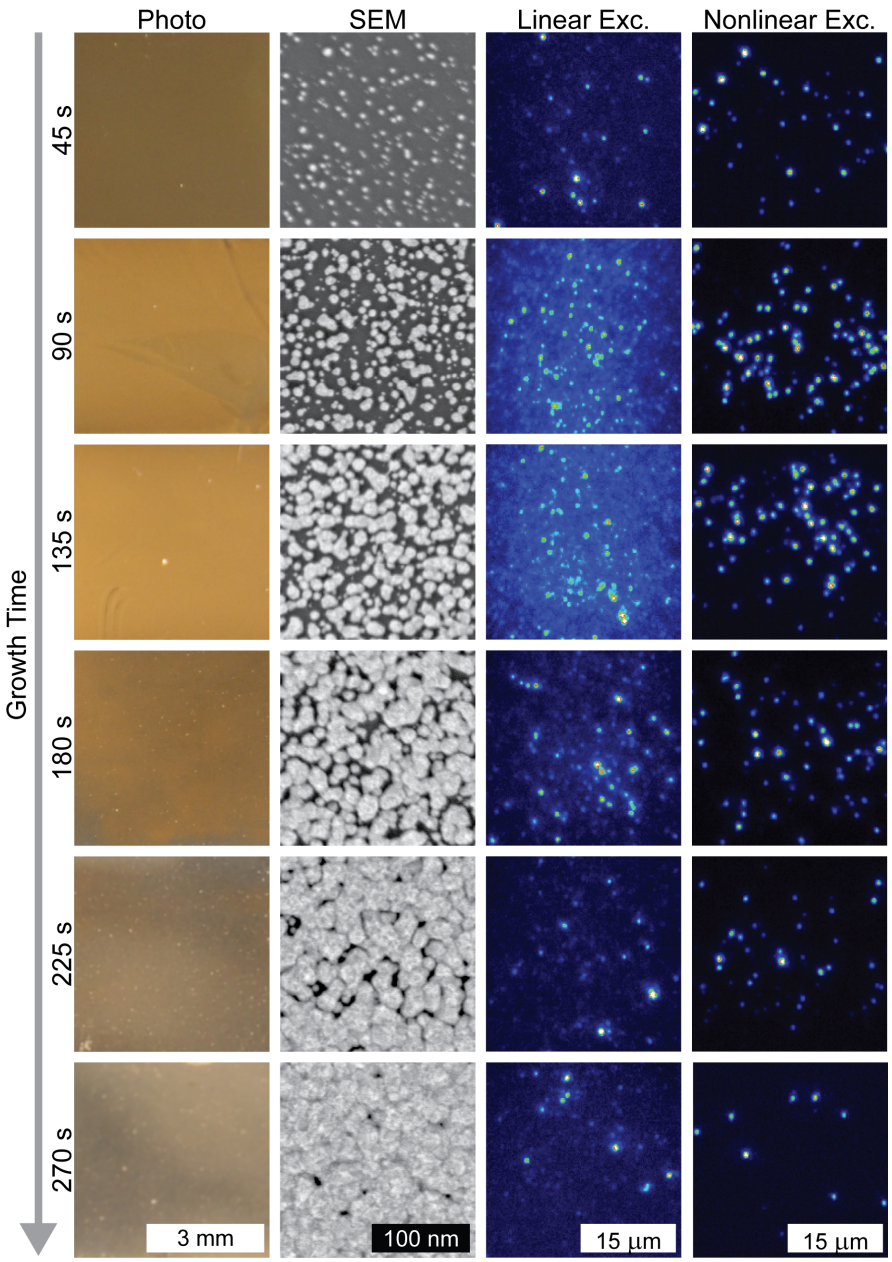

Figure 4.2. Influence of growth time on silver nanoparticle substrates for SERS. A series of Tollens substrates is shown, as a function of reaction time in the silver nitrate solution, as seen by eye (photograph); under the SEM; in the optical microscope under linear excitation at 456 nm; and in the microscope under nonlinear excitation at 912 nm. As the surface coverage increases, the film becomes more metallic and looks like a silver mirror for >225 s reaction time. The hot spot density scales nonmonotonously with surface coverage, but appears to be related to the density of voids between nanoparticles at longer growth times.

4.4.2 Enhancement phenomena in nanoparticle hot spots

The dependence of SERS intensity on growth time of Tollens substrates has been reported previously, displaying a rise as surface coverage increases, followed by a subsequent decrease [60]. Here, we compare the coverage-dependent SERS intensity reported in Ref. [60] to the average linearly and nonlinearly excited emission intensity in Figure 4.3. The main figure shows a dependence of enhancement factor (normalized to the 45 s substrate) on reaction time on a logarithmic scale. The inset gives the enhancement on a linear scale, normalized to the maximum intensity observed. The average intensity presented here is equivalent to the hot spot density multiplied by the average hot spot emission intensity.

Over the substrate growth times considered, the SERS intensity varies by approximately an order of magnitude, as does the one-photon excited hot spot luminescence. Remarkably, the SERS intensity and the one-photon luminescence follow virtually the same dependence on growth time, as seen more clearly on the linear scale in the

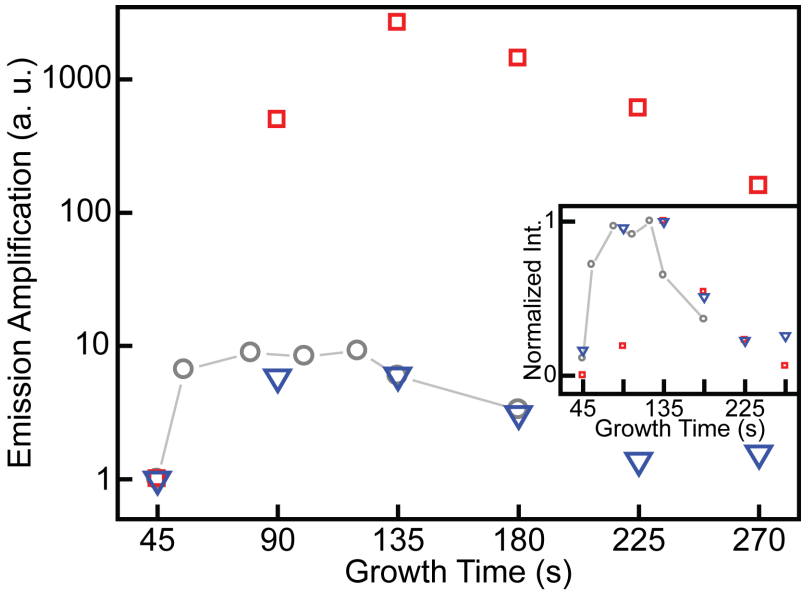

Figure 4.3. Dependence of surface enhancement on Tollens mirror growth time shown on a logarithmic scale and a linear scale (inset) for the multiphoton induced light emission (squares), one-photon induced light emission (triangles), and SERS (circles, data taken from Ref. [60]).

inset. This striking agreement between the linear emission and SERS indicates that the one-photon hot spots do indeed relate to a surface enhancement effect [34,43] and are not simply a consequence of isolated silver clusters, or even impurities, fluorescing [27, 75]: the light emission of silver under one-photon excitation is enhanced by plasmonic hot spots, as is SERS. Accordingly, analysis of the spectra and decay dynamics confirm that the linearly excited emission arises from a combination of SERS from carbon, and fluorescence from small, photogenerated silver clusters (see below). It appears that both processes experience the same surface-enhancement mechanism.

In contrast, the multiphoton excited emission increases by a factor of ∼3000, which greatly exceeds the enhancement seen in the linear excitation processes. Because of the superlinear dependence of multiphoton absorption on excitation intensity (see below), increased enhancement of nonlinear processes over those that are linear is expected if the strength of the fields in the hot spots increases with growth time. For example, if the excitation field within a hot spot doubles, the emission intensity for a linear optical process would be expected to double. But for nonlinear processes where the absorption cross-section depends upon the incident intensity, a superlinear dependence is anticipated. The microscopy shows that the increase in nonlinearly excited emission is not solely due to an increase in hot spot population (i.e., density of interstitial sites). Thus the field strength within the nonlinear hot spots must increase by at least an order of magnitude as growth times are increased from 45 s to 135 s; the hot spots get "hotter." The increase in linearly excited emission is a result of both an increase in the number of hot spots and the strength of the excitation fields within those hot spots.

We note a discrepancy between the increase in surface-enhancement between the linear and nonlinear processes: the difference in excitation power dependence cannot fully account for the difference in linear and nonlinear emission as a function of surface coverage. As discussed below, the excitation mechanism for both emission processes appears to be the same surface-enhanced effect, so we speculate that the origin of this difference does not simply lie in the underlying nature of linear and nonlinear

excitation hot spots. It is likely that the discrepancy arises due to differences in the emissive species that are situated within the hot spots and their corresponding excitation thresholds, although another possible origin for the discrepancy is an excitation wavelength dependence of the increase in enhancement with respect to surface coverage.

4.4.3 Power dependence of optical hot spots

Figure 4.4 displays the excitation power dependence of the light generated by two single representative hot spots, under excitation at 456 nm (a) and 912 nm (b). Inset in the respective panels are histograms of the power dependence exponents of 100 linear and 100 nonlinear hot spots as determined by the slope in a log-log plot of the individual curves. The power dependence was not recorded in a continuous ramp of excitation density but under upward and downward variations in power in order to reduce the effects of any photoinduced modifications. Reflecting a uniform linear power dependence, the linear hot spots have an average exponent of 0.97 with the distribution of exponents tightly grouped around the average. The majority of the linear hot spots have a linear emission intensity dependence on excitation power.

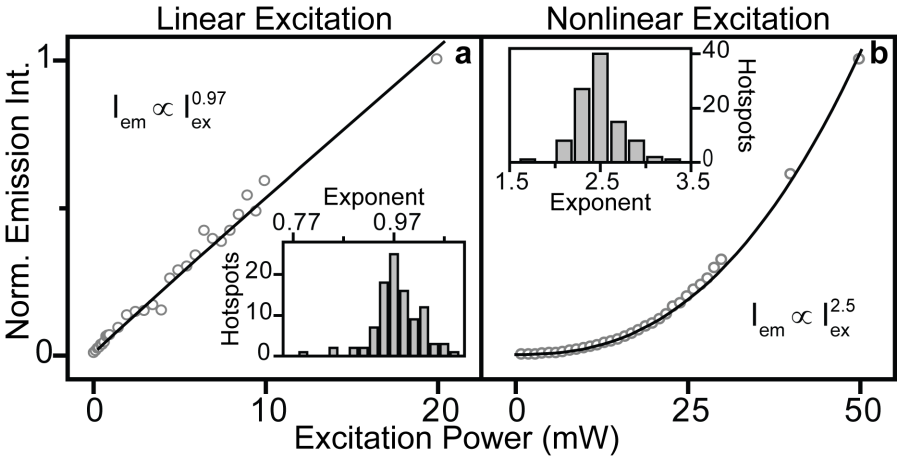

Figure 4.4. Power dependence of the light emission from a single hot spot under excitation in the UV (a) and excitation in the IR (b). The insets show the distributions of power-law exponents of the power dependence extracted for 100 linear and 100 nonlinear hot spots.

On the other hand, the average power dependence exponent of 100 nonlinear hot spots is 2.5 (inset) in accordance with a multiphoton process being responsible for excitation. However, unlike the 100 linear hot spots, the distribution of power dependence exponents of the nonlinear hot spots spans a much broader set of values. For hot spots with a cubic power dependence, the excitation process must be dominated by three-photon absorption while a purely quadratic power dependence indicates the excitation process primarily involves the absorption (or scattering) of two photons. Therefore, we conclude that the average nonlinear hot spot emission is excited by a combination of two- and three-photon processes. The substantial spread of the exponent distribution reflects the variation of this combination from hot spot to hot spot.

4.4.4 Polarization dependence and polarization memory of optical hot spots

Substantially more information on the absorption and emission processes of the linear and nonlinear hot spots can be gained by addressing the extent of their emission polarization and their dependence on excitation polarization. For example, a single optical transition dipole, such as that arising in an individual molecule, will exhibit both linearly polarized emission and linearly polarized excitation, meaning that emitted photons lie within a certain plane of polarization, and excitation photons must be in a particular plane of polarization to be absorbed. Although the excitation fields within the hot spots are anticipated to have a defined polarization state [19, 70], it is not immediately obvious whether or not the subsequent emission following the linear or nonlinear excitation processes is polarized.

To probe the emission polarization of the linear and nonlinear hot spots, we measure the modulation of the detected intensity as a function of the rotation angle of an analyzer placed within the detection path as depicted in the schematic in the top of Figure 4.5. Panels a) and d) display the modulation of representative single hot spots under linear and nonlinear excitation, respectively. Both traces show moderate modulation between a minimum and maximum value that fits a cosine-squared dependence on polarizer angle following Malus's law. The extent of

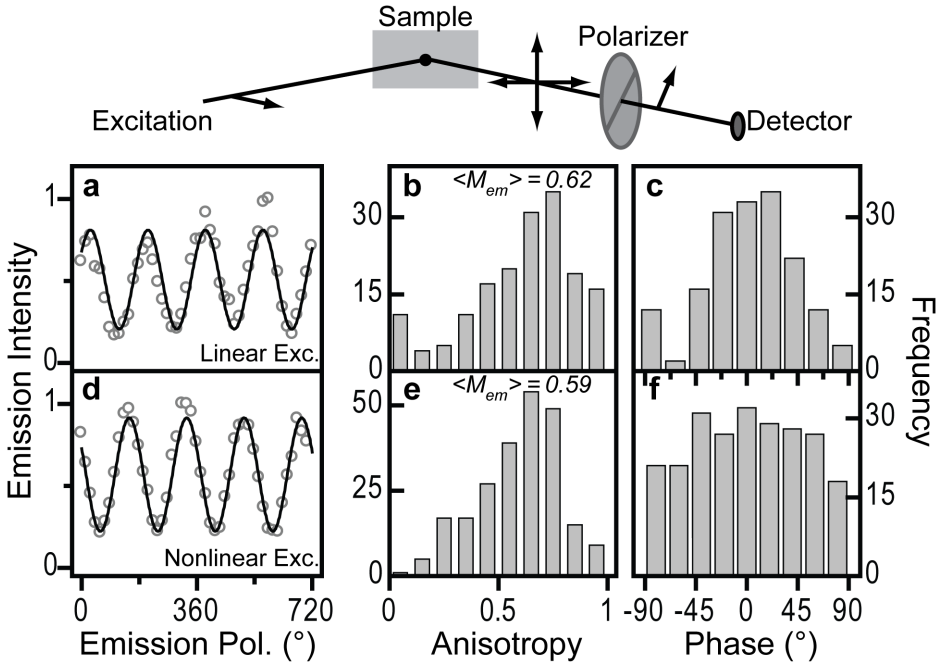

Figure 4.5. Polarization anisotropy of the light generated by single hot spots. The emission intensity is modulated by rotating a polarizer in the detection pathway of the microscope under one-photon (a) and multiphoton (d) excitation. The solid lines show cosine-squared functions. The polarization anisotropy M_{em} describes the degree of modulation of the light intensity. Histograms of M_{em} for 168 hot spots under one-photon (b) and 234 hot spots under multiphoton (e) excitation each scatter widely but represent very similar distributions. The phase of the cosine-squared fit represents the polarization angle of maximal emission relative to the excitation polarization, i.e., provides a measure of the polarization memory. Distributions for the linear (c) and nonlinear hot spots (d) reveal that the linear hot spots weakly prefer an emission polarization corresponding to the excitation polarization (i.e., exhibit a polarization memory) while the nonlinear emission dipoles are effectively oriented randomly with no memory of the excitation polarization.

the intensity modulations can be quantified using the polarization anisotropy value $M = (I_{\max} - I_{\min})/(I_{\max} + I_{\min})$ where $M = 1$ denotes a linearly polarized emitter, and $M = 0$ corresponds to a nonpolarized emitter. The anisotropy values were extracted for single hot spots by fitting the cosine-squared dependence of the intensity modulations with $I(\alpha) \propto 1 + M\cos(2(\alpha - \varphi))$, where α is the analyzer angle, and φ, the phase angle, is the polarization angle of the electric field that corresponds to maximum emission intensity. In our experimental setup, $\varphi = 0°$ corresponds to horizontal polarization (parallel to the optical table).

Panels b) and e) show the extracted emission polarization anisotropy values of 168 linear and 234 nonlinear hot spots. Remarkably, both distributions look very similar: they scatter widely and both have an average emission polarization anisotropy of $M_{\text{em}} = 0.7$. Clearly from panels a) and d), the modulated intensity does not drop to 0, and from the histograms in b) and e) the emission from the linear and nonlinear hot spots is only moderately polarized for the majority of hot spots. However, the extensive similarity between the anisotropy distributions underlines that the radiation, both linear and nonlinear, couples to the far field following the same pathway, which most likely begins with a single emitting dipole within the hot spot. We attribute the depolarization of the emission to the local scattering environment of the rough metal film [34].

Further information is found in the distributions of the phase angle of the cosine-squared fits shown in panels e) and f). This angle describes the orientation of the projection of the emission dipole onto the plane of the analyzer. In contrast to the anisotropy distributions, there is a slight difference in the phase angle distributions between linear and nonlinear excitation. It appears that the linear emission dipoles weakly prefer the 0° orientation which corresponds to the polarization of the excitation laser. On the other hand, the nonlinear phase angles are distributed equally across all possible orientations. While the exact nature of this discrepancy in polarization memory is not known, it provides the first indication that the single emission dipoles resulting from either linear or nonlinear excitation are different.

A similar single hot spot analysis was conducted with respect to excitation po-

larization. In this case, the hot spot emission intensity was recorded as a function of the linear polarization orientation of the excitation laser, which was rotated with a $\lambda/2$ wave-plate in the excitation path as shown in the schematic in Figure 4.6. Representative linear and nonlinear hot spots in panels a) and d), respectively, show substantial modulation between a minimum and maximum intensity as the excitation polarization is rotated. However, a drastic difference in the functional form of this modulation is clearly identified. Whereas one-photon excited emission follows the same cosine-squared dependence in absorption as seen in emission, the nonlinear emission displays a much more narrow response to the orientation of the excitation polarization, which is adequately described with a $\cos^4$-dependence. Such an enhanced response is expected from the coupling of a single dipole with nonlinear excitation power dependence to linearly polarized excitation.

Just as with the analysis of the emission polarization, the excitation polarization anisotropy, M_{exc}, can be extracted at the single hot spot level for both species. Panels b) and e) display histograms of the anisotropy values for 247 linear and 238 nonlinear hot spots, respectively. Whereas the values scatter widely for linear excitation and increase in frequency as M_{exc} approaches unity, virtually all hot spots under nonlinear excitation display completely polarized excitation with emission dropping to the sensitivity limit of the microscope at a certain polarization. The average M_{exc} value is found to be 0.76 for one-photon excitation and 0.97 for multiphoton excitation indicating that both linear and nonlinear hot spots strongly prefer a certain orientation of the excitation polarization.

Analogous to the emission polarization anisotropy, the phase of the modulation describes the excitation polarization orientation that results in maximum hot spot emission. The distributions of phase angles for linear (panel c) and nonlinear (panel f) hot spots clearly show that both hot spot species are preferentially excited with horizontally polarized light (0°). Because of our wide-field illumination configuration, horizontal polarization equates to a completely *p*-polarized illumination where the electric field component normal to the metal film is maximized. Consequently, the linear and nonlinear hot spots are brightest when the normal component of the

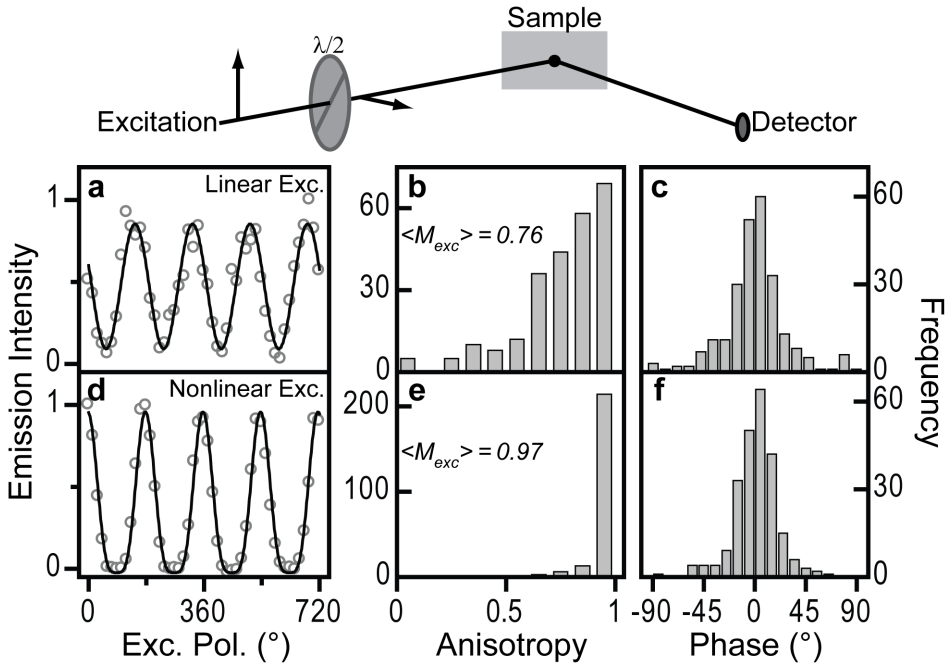

Figure 4.6. Polarization anisotropy of the excitation of single hot spots. Modulation of the emission intensity by rotating the plane of polarization of the incident laser under one-photon (a) and multiphoton (d) excitation. The solid lines show a cosine-squared (a) and a $\cos^4$ function (b), respectively. The histograms of the polarization anisotropy in excitation, M_{exc}, each differ strongly between 247 hot spots under one-photon excitation (b) and 238 hot spots under multiphoton excitation (e). (c), (f) Histograms of the phase angle of the cosine-squared (or $\cos^4$) fit functions, showing a preference for all hot spots to light up at the same excitation polarization angle. This distribution suggests a universal excitation mechanism for both processes, involving surface plasmon polaritons. Note that a random distribution of dipolar absorbers, such as single molecules, would exhibit a uniform flat distribution of phase angles.

excitation field is strongest. The spread of the phase angle distribution is attributed to the surface roughness that leads to a distribution of surface-normal vectors. As elaborated in the discussion section, this distribution strongly suggests that both excitation processes are a result of surface-enhanced excitation through localized surface-plasmon modes.

4.4.5 Single hot spot emission spectra

Single hot spots exhibit spectral properties reminiscent of those of single molecules [76]: the emission varies substantially from spot to spot as different elements of the inhomogeneously broadened ensemble are probed. Figure 4.7 displays a set of one-photon emission spectra, recorded from 9 different hot spots on a substrate under excitation by the femtosecond laser at 456 nm. The spectra differ substantially from one to another, but generally reveal two distinct characteristics: a broad, weakly-structured band spanning the visible spectrum from ∼460−650 nm; and at least one narrow peak around 500 nm which most likely arises from Raman scattering since its position shifts with excitation wavelength. In fact, close inspection

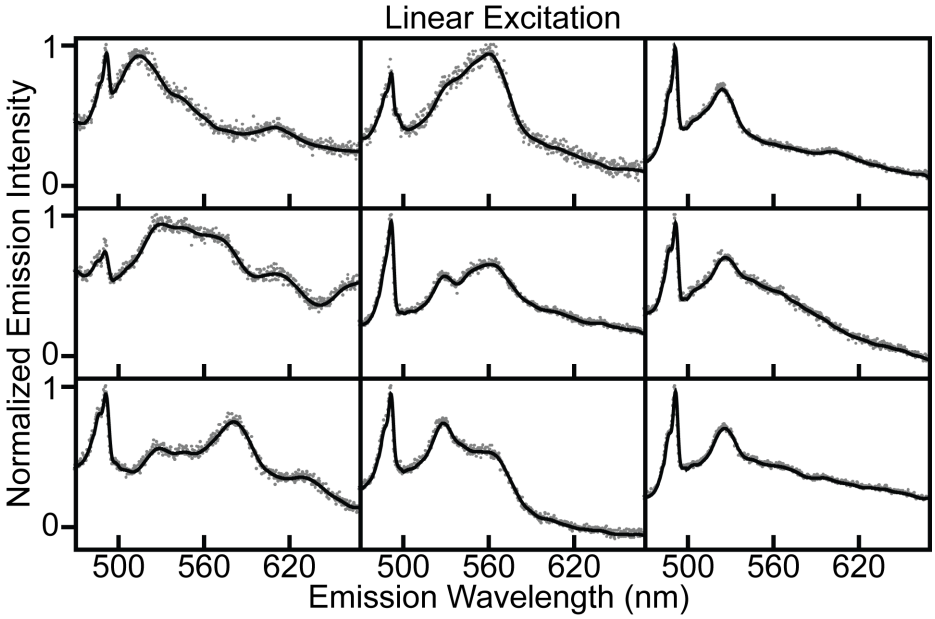

Figure 4.7. Representative spectra of 9 different single hot spots under linear excitation.

reveals that the peak carries some substructure and most likely arises from multiple vibrations, offset by 1,380 cm^{-1} and 1,590 cm^{-1} from the exciting laser. The spectral width of these Raman lines is representative of the spectral width of the pulsed laser illumination. Further structure is observed in most spectra at 3,000 cm^{-1} and 4,500 cm^{-1}. These vibrational modes are in excellent agreement with the first and second harmonic vibrations of carbon contamination [77]. We suspect that the presence of such carbonic species is primarily due to atmospheric exposure as it has also been observed on evaporated silver films where carbon compounds are not involved in the silver deposition and growth process [78]. Note that due to the strong fluctuations in emission, we were not able to piece together multiple spectra of the same spot with different center wavelengths of the monochromator, thereby limiting the overall spectral range shown in the figure to the range of the spectrometer (140 nm).

Under multiphoton excitation, in contrast, narrow spectral features are not observed. Figure 4.8 displays a selection of 9 single hot spot spectra, recorded under excitation at 912 nm. For this measurement, two individual spectra were fused

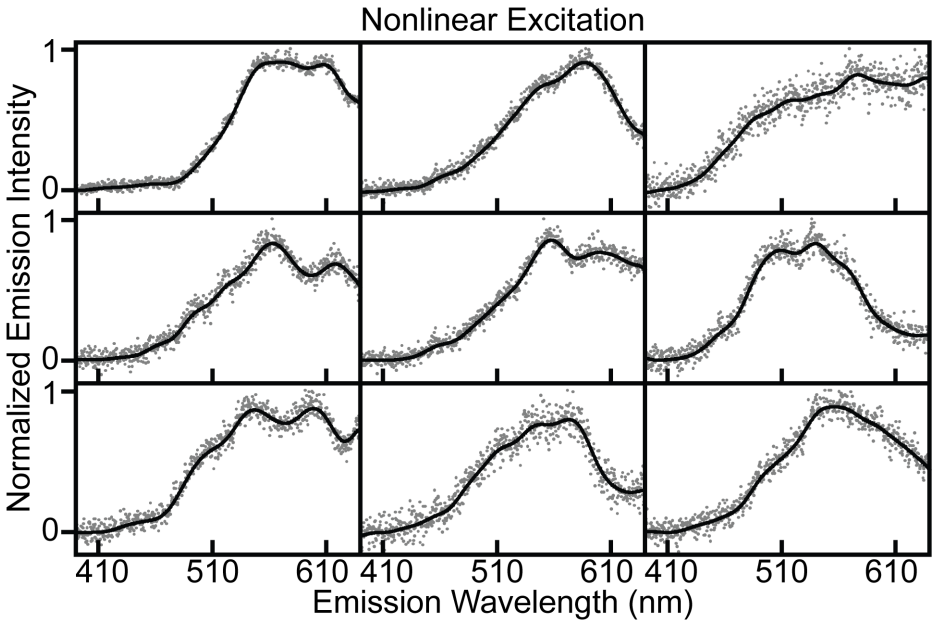

Figure 4.8. Representative spectra of 9 different single hot spots under nonlinear excitation.

together for different center wavelengths of the spectrometer, leading to a total spectral range of 220 nm. This approach was possible because the single hot spot spectra do not fluctuate with time (see below). Although these multiphoton spectra clearly differ from the single-photon case and are generally broader, the diversity in emission characteristics is comparable. A couple of protrusions are typically observed in the broad spectra, but at different wavelengths for each spot. Some spectra appear to peak within the spectral range considered; others extend further into the IR, peaking beyond 700 nm. There are distinct differences in the onset wavelength of the spectra: some hot spots emit radiation at and above 410 nm, other spectra do not set in until 490 nm. Some spectra reveal a very subtle peak at half the excitation wavelength, characteristic of SHG. We generally find that the SHG peaks are more intense for shorter silver mirror growth times and longer excitation wavelengths.

The fact that the emission spectra under one- and multiphoton excitation differ demonstrates that both emission phenomena have distinct origins: multiphoton emission is not simply due to multiphoton absorption and subsequent luminescence from a silver cluster, but must involve fundamentally different processes.

4.4.6 Excitation wavelength dependence of optical hot spots

In nanostructured metal films, the occurrence of a plasmonic optical hot spot in a given location depends crucially on the relation between the wavelength of the incident light and the size and arrangement of the nanoparticles involved. The localized plasmon modes are very sensitive to the initial excitation conditions [17–19, 79]. Consequently, different hot spots should appear at different excitation wavelengths, and the range of excitation wavelengths that excite a hot spot should be restricted. As the emission from nonlinear excitation is more sensitive to the field strength within the hot spot, one may also expect that the wavelength dependence is more restricted for spots showing multiphoton excitation than for spots arising from one-photon excitation. Figure 4.9 contrasts the two cases.

For one-photon emission in panel a), the excitation wavelength is tuned in 20 nm steps from 400 nm to 500 nm and back down again, while recording the hot spot luminescence on the same sample region. As noted above, this linear emission is

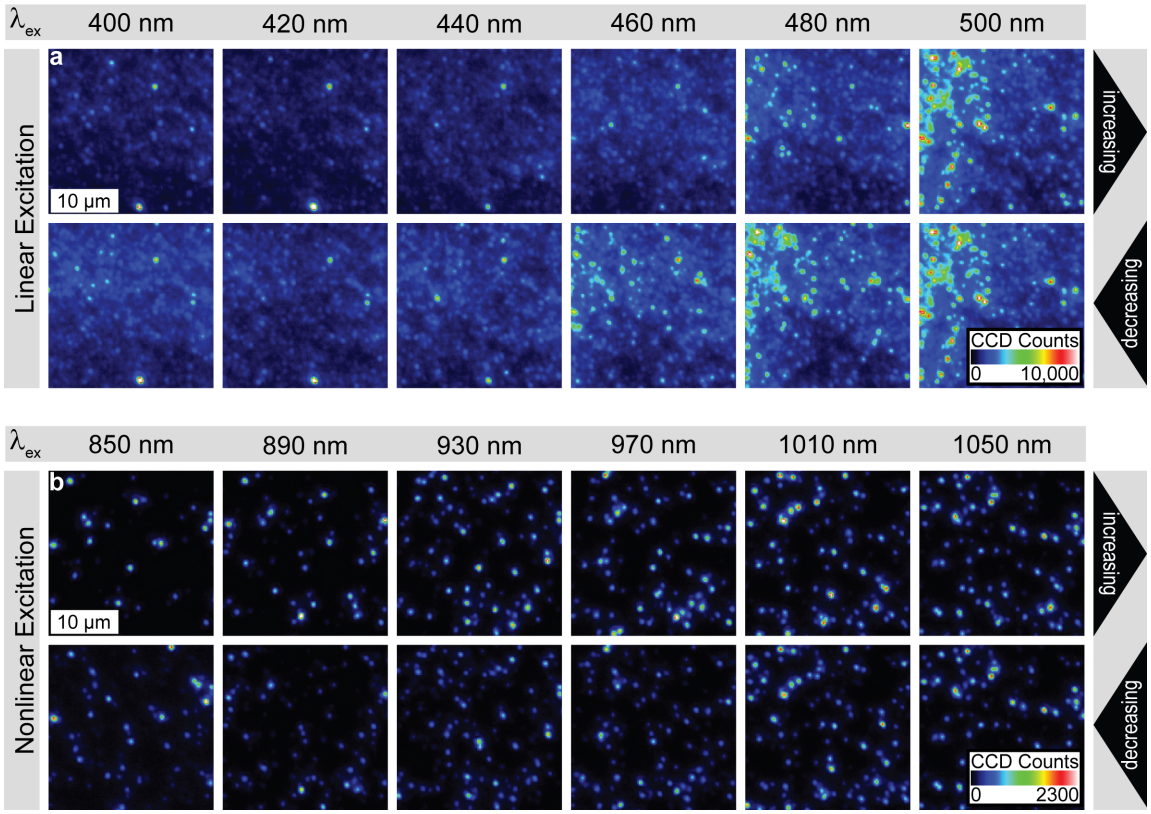

Figure 4.9. Excitation wavelength dependence of images of single hot spots under linear (a) and nonlinear excitation (b). The wavelength is scanned up and down while the same sample area is considered. The patterns are reproducible upon upward and downward sweeps of the excitation, and change more strongly with wavelength under nonlinear than under linear excitation.

generally accompanied by a significant background, which appears to increase with increasing wavelength. Quantitative comparisons of the microscope images recorded at different excitation wavelengths are further complicated by the fact that these hot spots exhibit substantial temporal fluctuations – blinking [28, 34]. In addition, the background luminescence under one-photon excitation increases with exposure time, an effect particularly pronounced under femtosecond laser excitation in the UV (i.e. femtosecond one-photon excitation) [23, 75]. The growth of the background over exposure time is visible in the emission of the two 400 nm excitation images in Fig. 4.9a. Nevertheless, the experiment is reproducible upon consecutive sweeps of the laser wavelength: the hot spot distributions in the upper and lower panels of Fig. 4.9a) appear virtually identical.

As the excitation wavelength is raised, the number of spots observed increases. Indeed, it appears that single hot spots only respond to a restricted range of excitation wavelengths. While a large number of hot spots appear only for an excitation wavelength range spanning ∼60 nm, a couple of hot spots lack narrow resonances: the spot seen in the upper right hand corner of the image at 400 nm is discernible at all excitation wavelengths. Generally, the observed spots tend to become brighter for longer excitation wavelengths which is attributed to increased collection of SERS from contaminants on the surface. Since a 515 nm long-pass filter was employed to record the images, the Raman modes that are Stokes shifted by $\sim 1,600$ cm^{-1} and $\sim 3,000$ cm^{-1} with respect to the excitation laser only contribute to the detected intensity for excitation wavelengths above 476 nm and 446 nm, respectively. This effect may also contribute to the apparent reduction in the spatial discreteness of the images and associated increased background at longer excitation wavelengths.

The situation for multiphoton excitation is shown in panel b), for which a wavelength range of 200 nm was considered in 40 nm steps. Here, the hot spots are seen in the image without a background. During the measurement, occasionally new hot spots appear due to photochemical modification of the silver film, but no blinking is observed (see below). Consequently, the spot density in the upper row of the images (increasing wavelength) is slightly lower than the density at the corresponding

wavelength in the downward sweep. Although the overall spot density approximately doubles between 850 nm and 1050 nm excitation, different spots are found to light up at different wavelengths. Nevertheless, the average spot brightness remains roughly constant and thus independent of wavelength. The multiphoton hot spots exhibit signatures of narrow spectral resonances characteristic of increased sensitivity to plasmonic enhancement in the excitation process, whereas one-photon hot spots only display a weak dependence on excitation wavelength.

4.4.7 Blinking and spectral diffusion of single hot spots

One of the biggest surprises when comparing one- and multiphoton emission from Tollens silver films arises from consideration of the temporal emission dynamics on the timescale of seconds. Figure 4.10a) shows a series of images of a single hot spot under linear excitation recorded at different times. Strong fluctuations are observed in the intensity of this diffraction limited light spot in agreement with earlier observations on related silver-based materials systems [27, 28, 34]. The variations in intensity are reported in the graph in panel a), which shows switching events in the luminescence that are similar to blinking from single molecules and quantum dots [80]. The red circles in the trace indicate the times at which the exemplary images were recorded. Panel b) shows a similar measurement for a hot spot under multiphoton excitation. In this case no discrete switching in the emission intensity is observed: the intensity merely follows a gradual decay arising from a photomodification process.

These initial observations regarding the stability of the fluorescence intensity are mirrored in considerations of the dynamics in the emission spectra of single hot spots. Figure 4.11 compares the temporal evolution of one- and multiphoton emission spectra in a two-dimensional representation of emission wavelength as a function of time, where the emission intensity is encoded in color. The measurements were performed over a timescale of 30 minutes. The one-photon emission spectrum in panel a) displays strong fluctuations in intensity, accompanied by dramatic changes in the actual spectrum. Several peaks are observed in the spectra, and the relative intensities of these peaks appear to vary with time. Large bursts of narrower peaks, marked in

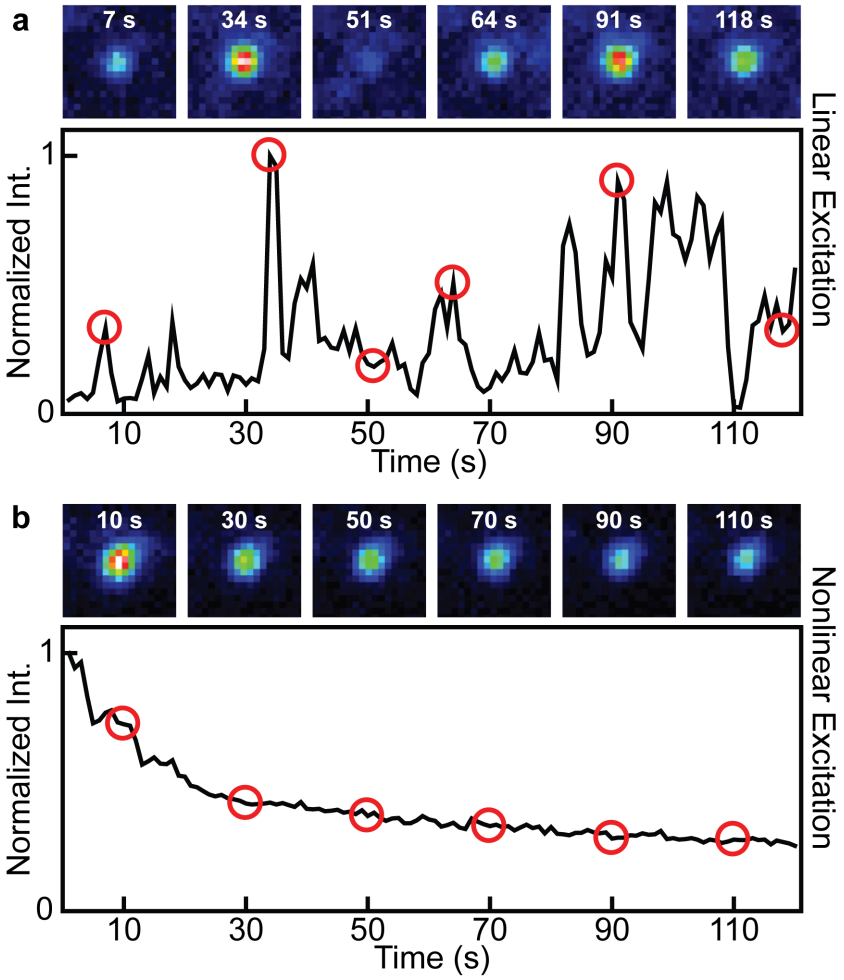

Figure 4.10. Temporal dynamics of the light generated by one single hot spot under linear (a) and nonlinear (b) excitation. Image series of the diffraction-limited hot spot (image region 3×3 μm^2) are shown above. Whereas one-photon excitation gives rise to strong blinking, single hot spot emission under multiphoton excitation appears stable with time besides a small gradual decay in intensity.

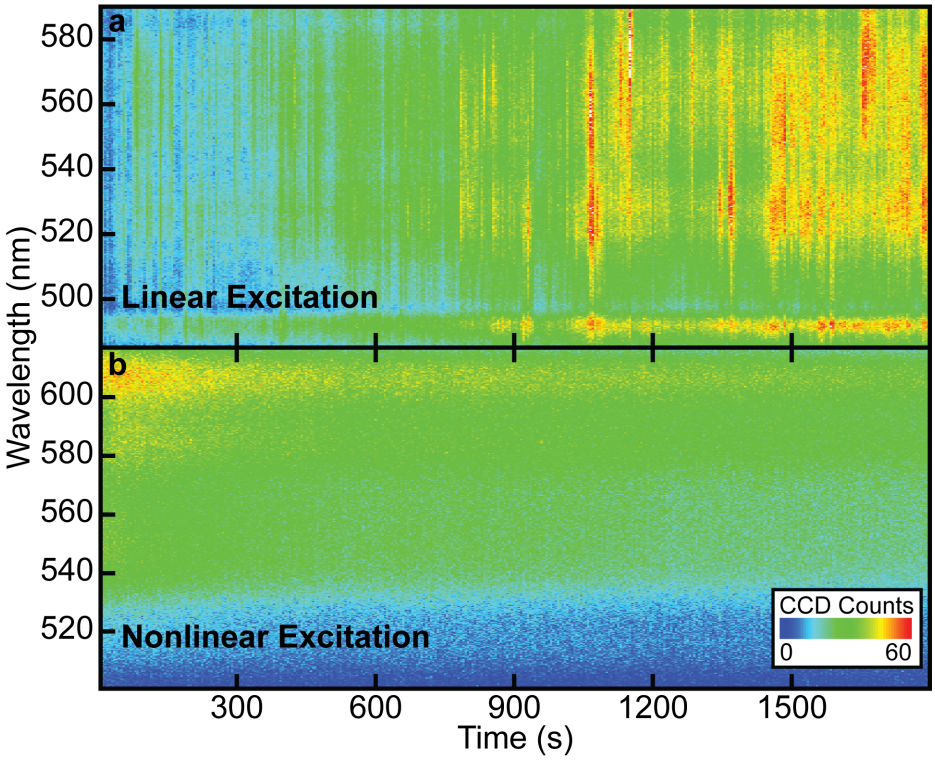

Figure 4.11. Spectral fluctuations in the emission of a single hot spot under linear (a) and nonlinear (b) excitation.

red, are seen to be superimposed on a broader continuum spectrum. The most distinct features around 490 nm can be assigned to the 1,350 cm^{-1} and 1,580 cm^{-1} Raman bands (see above). While these modes appear constant in wavelength, the other peaks around 525 nm (3,000 cm^{-1}) and 560 nm (4,000 cm^{-1}) show more pronounced fluctuations. Occasionally, entirely new peaks appear in the spectrum, such as at time $t = 1,155$ s (at 580 nm) and at $t = 1,665$ s (at 575 nm). Both of these sporadic peaks correspond to a $\sim$2,100 cm^{-1} Raman mode. Although these narrow spectral features are suspected to originate from Raman scattering, it is not straightforward to rule out the presence of multiple emission centers within one diffraction-limited hot spot. If such different emission centers have distinct emission spectra, then fluctuations in intensity of the indistinguishable emitters could give rise to the spectral variations observed.

The multiphoton luminescence in panel b) exhibits precisely the opposite behavior. The emission spectrum remains absolutely unchanged over time, bar a slight overall decay in emission intensity. Very occasionally, a sudden increase in emission is observed (not shown), which may provide an indication of photochemical activation of emission [81]. This stability of multiphoton excitation makes nonlinear optical hot spots particularly interesting as nanoscale optical white light beacons for high-resolution transmission microscopy [56].

4.4.8 Time-resolved light emission from hot spots

To fully unravel the significant differences between emission from Tollens SERS substrates under linear and nonlinear excitation, an investigation of the temporal emission decay dynamics is required. Maintaining spectral resolution makes such studies prohibitive on the level of single hot spots since the overall emission intensity is weak and the spectrum is generally broad. We therefore consider the time resolved luminescence from an ensemble of hot spots, as summarized in Figure 4.12. Panel a) displays a streak camera image of the time-resolved luminescence of the silver film: the emission spectrum is plotted against time in a color-coded two-dimensional representation. Two interesting observations can be made: first, the immediate

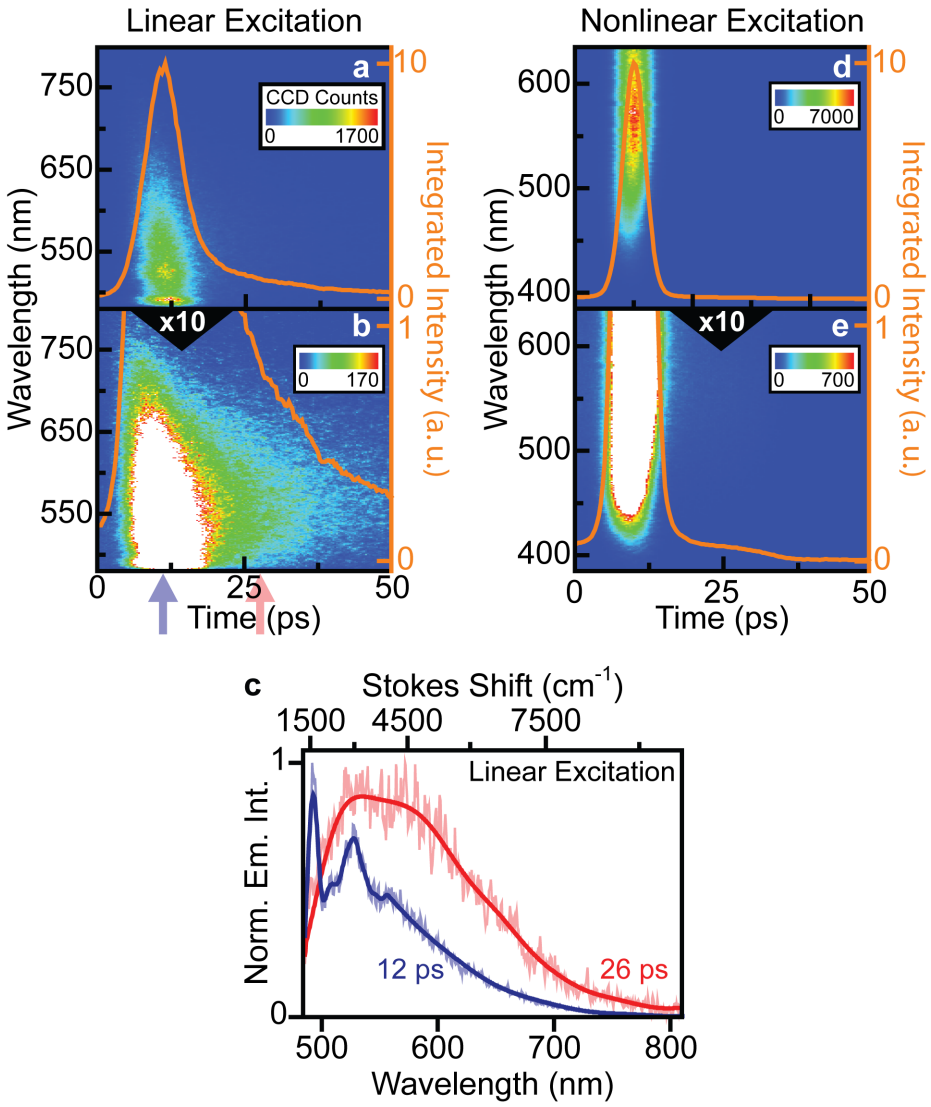

Figure 4.12. Time and spectrally resolved emission from a rough silver film (180 s growth time) under linear (a,b) and nonlinear (d,e) excitation. The orange lines show the evolution of the spectrally integrated intensity as a function of time. Note that the raw data are shown; the exciting laser pulse arrives at 12 ps (linear excitation) and 14 ps (nonlinear excitation). Panels (b), (d) display the same time-resolved spectra magnified by a factor of 10 in intensity to reveal the longer-lived decay of the luminescence in the case of linear excitation. Nonlinear excitation leads only to quasi-instantaneous light emission with no discernible transient. c) Normalized prompt (12 ± 2 ps, red) and delayed (26 ± 2 ps, blue) spectra found under linear excitation.

(prompt) emission spectrum contains significant substructure on top of a broad background; second, the emission intensity (orange line) does not drop to zero within the time resolution of the experiment (approximately 4 ps). The lack of comparable substructure on top of the broad background in the delayed emission reveals that the overall emission spectrum changes significantly with decay time. The phenomenon is exemplified in panel b), where the intensity color-scale is adapted to amplify the delayed luminescence by a factor of 10, revealing luminescence decay over a time-scale of 150 ps. The luminescence intensity decay does not appear to be exponential.

Panel c) compares the prompt light emission under one-photon excitation with the delayed emission (blue), recorded between 5 and 25 ps (red). The prompt emission exhibits two narrow peaks at ∼490 and ∼530 nm, superimposed on a broad background. These narrow peaks are shifted from the exciting laser by 1,500 cm^{-1} and 3,000 cm^{-1}, respectively. Our earlier assignment of these peaks to Raman scattering from contaminants (such as carbon residue) is further confirmed since they only appear in the instantaneous emission [49]. The broad background, on the other hand, is not instantaneous and has an observable decay, which indicates that it is luminescent in nature, in contrast to an ultrafast scattering process. The important implications of these results in regards to the broad background commonly observed in SERS are elaborated on in the next section.

The situation is rather different under multiphoton excitation, as shown in panel d): here, all of the emission occurs instantaneously, within the time resolution of the measurement. As discussed above, no relevant substructure is observed in the emission spectrum, except for the SHG peak which can be identified under certain conditions. Panel e) displays a magnification of the multiphoton response of the Tollens film by a factor of 10: no slow decay component is discernible in the luminescence, and the measured intensity (orange) drops to zero within the time resolution of the experiment. Whereas one-photon excitation appears to result in a combination of instantaneous Raman scattering with a transient fluorescence-like broad feature, all of the multiphoton emission occurs instantaneously, further distinguishing the linear and nonlinear emission processes.

4.4.9 Temperature dependence

We investigated the effect of temperature on the one- and multiphoton emission spectra by cooling the samples down to 5 K. We found no discernible influence on either the spectral or intensity dynamics, or on the overall single hot spot emission spectra. The fact that lowering the temperature does not significantly reduce the one-photon luminescence speaks against a purely thermally-induced rearrangement of material in the hot spot as a source of the emission dynamics, such as a motion of contaminant molecules giving rise to discrete blinking. More likely, the blinking processes are photoinduced, much like in the case of single quantum dots [53, 80]. We also do not observe any significant spectral changes of the one- and multiphoton emission upon cooling, or of the one-photon luminescence lifetime. This fact suggests that the emission from the silver under one-photon excitation does not originate from a thermalized excitation, although it clearly involves a transition via a metastable state. In contrast, luminescence spectra from single molecules and quantum dots exhibit significant spectral narrowing upon cooling [76]. These temperature dependent experiments are especially important, as they enable combined and simultaneous high resolution single molecule fluorescence and Raman scattering. At these low temperatures a clear spatial anticorrelation between hot spots on the substrate which exhibit single molecule Raman scattering, and hot spots displaying nonlinear white light emission becomes apparent [10].

4.5 Discussion

4.5.1 Similar excitation pathways between one- and multiphoton hot spots

Both emission processes, linear and nonlinear, clearly display signatures of surface enhancement arising from localized plasmon excitations of the nanoparticle aggregates [74]. Individual nanoparticles do not exhibit single or multiphoton luminescence of a comparable magnitude, and efficient light emission only becomes visible when multiple nanoparticles are in close vicinity as revealed by the SEM images. Consequently, there is a strong dependence of hot spot emission on the growth time of the silver mirror. The number of one- and multiphoton hot spots observed increases with growth time

until the surface is covered to approximately 90 % with silver. Subsequently, the number of voids observed in the silver film decreases, and so does the density of optical hot spots seen. As is particularly evident in the nonlinear emission, the average brightness of the hot spots increases with growth time as the silver films change morphology from discrete nanosized particles to larger aggregates of particles. This indicates that the morphological change increases the surface-enhanced localized fields, which lead to "hotter" hot spots.

Further evidence indicating that both processes are surface-enhanced is found in the excitation polarization anisotropy. Both processes emit maximally when the incident polarization maximizes the component of the electric field parallel to the surface normal of the sample. The selective response to this polarization shows that the excitation of both types of hot spots results from the initial excitation of localized surface plasmon modes of the nanostructured metal film [82] as opposed to direct excitation of the emissive species. Preferential coupling of the hot spots to the normal electric field vector mediated by localized plasmon modes is in good agreement with the observed excitation anisotropy values. Although the degree of polarization for both linear and nonlinear excitation seemingly suggests that the hot spots behave as single dipoles in the excitation process, this conclusion may be misleading. The localized polarization of the electric field within the hot spot is most likely unaffected by the polarization state of the excitation laser. Rather, the laser polarization only controls how well the excitation field couples to the plasmon mode and thus the resulting strength of the electric field within the hot spot.

4.5.2 Different emission processes of one- and multiphoton hot spots and evidence for emissive silver clusters

The contrast between the linear and nonlinear hot spots strongly indicates that fundamental differences between the two emission processes exist. To briefly summarize, the emission spectra of both processes are generally different. On the timescale of picoseconds within the initial excitation pulse, the nonlinear excitation shows only a quasi-instantaneous emission whereas the linear excitation consists of both quasi-instantaneous Raman scattering and delayed luminescence with a decay transient of

over 150 ps. Finally, one-photon excited emission shows strong fluctuations in both intensity and spectrum on the timescale of seconds while the multiphoton emission is generally stable in both regards.

Intermittency, as seen in the linear emission, is generally a sign of bistability and can occur in a wide range of dynamic systems, such as mechanical or electronic oscillators with nonlinear feedback. In atoms, quantum dots, and molecules, blinking in the luminescence can arise when the emitting entity is no longer treated as a simple two-level system [80]. One of the simplest causes for (short-term) intermittency in the train of fluorescence photons emitted from a single molecule, for example, are random excursions to the long-lived triplet state. Treating the molecule as a three-level system allows bistability to arise, where the molecule can exist in two distinct states: emitting (within the singlet manifold) and nonemitting (within the triplet manifold). More complex but conceptually related situations can be derived from considering excursions to charge separated states: in a quantum dot, for example, the formation of a charge separated state will promote Auger recombination of subsequently generated excitations, leading to luminescence quenching [80].

Combined, the photo-activation, emission spectrum, observed intermittency and the noninstantaneous emission decay indicate that the one-photon luminescence arises from small silver clusters and involves transitions between discrete electronic levels. Thus, the linear emission is, in principle, comparable to light emission from other nanoscale structures such as molecules and quantum dots. This result is in good agreement with previous studies of silver-oxide nanoparticles, which reduce to small (25 atoms or less) luminescent silver clusters upon UV illumination [27, 28, 42, 78]. The spectrum of the broad emission after the instantaneous decay regime (Fig. 4.12c) agrees quite well with the emission reported for luminescent silver clusters photogenerated from silver oxide. Further, the pronounced spectral jitter observed in the emission of the linear hot spots is consistent with the spectral jitter observed in particles derived from the silver-oxide reduction mechanism [27]. Consequently, the broad background with noninstantaneous decay dynamics most likely arises from surface-enhanced reduction of the native silver oxide layer within the hot spot to a

small emissive silver cluster. In this context it is important to note that charging of small silver clusters was recently directly observed in transport measurements [83,84], and can likely be directly related to the optical characteristics. It is conceivable that charging of the nonmetallic emissive silver cluster could be a principle contributor to the observed blinking phenomena. The Raman signal in the one-photon excited luminescence is most likely due to carbon contaminants deposited on the substrate during growth or following exposure to the ambient atmosphere.

The lack of emission fluctuations, the contrast between the linear and nonlinear emission spectra, and the different decay dynamics lead us to conclude that the multiphoton emission cannot be due to two- or three-photon excitation of silver fluorescence [81, 85] as has been proposed for gold nanoparticles [86]. Given the variation of power-dependence, the emission possibly arises from some mixture of quasi-instantaneous, potentially coherent, nonlinear optical effects such as stimulated Brillouin [87] or broad-band hyper-Raman scattering [25]. In such a stimulated scattering process, the incident light is converted nonlinearly in frequency due to the excitation of multiple vibrations, which in turn modify the polarizability of the material in the hot spot. Continuum generation due to nonlinear optical processes is a well-known phenomenon in dielectrics such as glasses, although it is not entirely understood [87]. The effect can be dramatically enhanced under suitable confinement of light, and is exploited in photonic crystal fibers to generate very broad-band ultrashort light pulses [87]. The crucial aspect to note is that such a nonlinear continuum generation process depends on the third order susceptibility of the material, $\chi^{(3)}$. It appears that this quantity of the material being probed through nonlinear light emission does not vary with time. Both the nonlinear and linear hot spots show increased hot spot density and intensity with increasing illumination time. So, while the emission processes are different as outlined above, this striking similarity in photo-activation suggests that a likely candidate for the nonlinear emission source is also given by clusters of silver atoms, even if they may be too large to fluoresce. Such a cluster could be native to the film and undergo photomodification when illuminated, or it could be a result of silver-oxide photogeneration much like in the case of the

clusters responsible for the one-photon emission.

In the SEM images of the Tollens films, particles down to ∼2 nm in size can be identified, demonstrating that the films are made up of a broad range of particle dimensions. At such a high magnification used in the SEM, the delicate substrates themselves are damaged so that the imaging process is not reproducible. The fact that at every magnification employed in the SEM new feature sizes become visible suggests that particles are present which cannot be resolved in the SEM. Further, the one-photon excited luminescence is a strong indicator that discrete silver clusters exist in the silver film [27, 42, 78]. We sketched this scenario in Fig. 4.1d). In the following we list the additional experimental evidence which points to a polarizable species such as a small silver cluster present at the focus of a silver nanoparticle hot spot:

- Multiphoton emission only occurs at spatial positions from which Raman scattering is not observed under visible excitation [10]. This observation can be interpreted in terms of a polarizable species physically blocking the hot spot and thus attenuating the surface enhancement effect at larger distances

- SHG exhibits strong intermittency whereas the multiphoton emission from the same hot spot is stable with time [72]. This result underlines that it is not the enhancement effect which changes with time, but the nonlinear polarizability. The second-order susceptibility $\chi^{(2)}$, which governs SHG, is much more sensitive than the third-order susceptibility $\chi^{(3)}$. The former requires a break in inversion symmetry and thus probes only the surface, for example, of a particle. The latter averages over the entire bulk of a particle.

- Both one-photon and multiphoton emission clearly reveal the same enhancement process in dependence of excitation polarization and surface coverage, as does the actual SERS signal (Fig. 4.3), suggesting that all three optical processes probe the same optical enhancement phenomenon.

- The near identical emission polarization anisotropy distributions of the linear and nonlinear hot spots is a strong indication that both processes involve the excitation of a single dipole within the hot spot.

- Although one-photon emission bears characteristics of fluorescence and evidently involves an electronic transition from a metastable state, the absence of a significant temperature dependence of the emission spectrum suggests that the species responsible for light emission does not thermalize with the surrounding. Weak thermalization is a signature of limited degrees of conformational freedom as found in electronic transitions in isolated atoms and small clusters.

We conclude that optical hot spots in the film may or may not be occupied by a small silver cluster, which in itself does not dramatically affect the localized plasmon mode of the metal film. Further development of silver clusters around or within the hot spots is promoted by UV excitation, which converts native silver oxide into luminescent silver clusters. Linear excitation reveals a combination of SERS from surface contaminants and the surface-enhanced photogeneration and fluorescence of the clusters. Nonlinear excitation uncovers the surface-enhanced nonlinear response of the clusters, but does not probe all of them as seen from the fact that the hot spot densities under the multiphoton excitation conditions are lower. In fact, it is possible that nonlinear excitation only probes the largest clusters (with the largest $\chi^{(3)}$). Concomitantly, the presence of a cluster in the hot spot has important ramifications for spectroscopy and may reduce the overall surface enhancement of other processes such as SERS of analyte molecules [10].

4.5.3 Implications for SERS and other surface-enhanced processes

The spectral profiles and temporal dynamics of the linear hot spots show that the emission arises from two distinct processes. The first process is characterized by narrow spectral features and quasi-instantaneous emission decay, which both suggest SERS of contaminant species. The second process yields a broad emission most likely due to luminescence from silver clusters that were photogenerated from the native

silver oxide layer [27, 28, 42, 78]. When the spectral profiles of these two emission processes are combined, the resulting time-integrated emission spectrum is very reminiscent of a SERS spectrum with the accompanying characteristic broad background. This broad background is a common plague for SERS techniques [53,88–95], and much attention has been given to it. Some of the proposed origins include electronic Raman scattering [88,89], surface-enhanced fluorescence [53,95] and metal nanoparticle light emission [92–94]. The time resolved emission decay measurements shown here strongly suggest that ultrafast emission processes such as electronic Raman scattering are not the origin of the broad SERS background. Rather, especially on silver, the broad background most likely arises from luminescent metal clusters as proposed by Itoh *et al.* [92–94]. The presence of native silver oxide which is photoreduced to emissive silver clusters in or around SERS hot spots may have significant implications for developing a complete picture of hot spot enhancement including the accurate analysis of chemical enhancement mechanisms [96].

It is important to carefully consider the proximity of the emissive metal clusters to SERS hot spots. Complicating such considerations, emissive metal clusters are sized well below the resolution limit of optical microscopy systems. Various reports have previously claimed correlations between one-photon induced background and SERS [91], and a lack of such correlations [8]. These conflicting reports indicate the possibility that the emissive silver clusters which give rise to the background may just be near the hot spots and not actually situated within them. Indeed, our previous detailed investigations of single molecule SERS from these Tollens substrates show that most spectra can be obtained without significant background, provided that the slit of the spectrometer (see Figure 4.1) is sufficiently narrow to select only a very narrow region on the sample [10]. It would be extremely hard to prove a spatial anticorrelation between single molecule SERS hot spots and one-photon luminescence hot spots (as observed for the case of nonlinear emission) due to the extreme dynamics in linear hot spot emission. However, the fact that the background tends to be absent in the best single molecule SERS spectra under excitation in the UV to visible spectral region [11] strongly suggests that a spatial anticorrelation may exist for one-photon

hot spots and SERS.

We recently demonstrated that such a spatial anticorrelation exists between SERS under visible excitation and nonlinear hot spots, thereby providing a possible route to screen and isolate SERS active hot spots [10]. A related study used a negative resist to selectively isolate the nonlinear hot spots and use those hot spots for SERS at infrared excitation [97]. Further understanding and control of the linear response of the silver films at visible wavelengths may enable a similar approach to improve the performance and reliability of SERS by isolating only the best hot spots on the silver surface [98]. Extending such a technique to broader spectral regions is desirable in the context of resonant Raman spectroscopy, where excitation energies are defined by the analyte rather than the apparatus.

Additionally, the time resolved decay of the linear hot spot emission provides a reasonably facile route to removing the broad background contamination of SERS (when it does occur) via optical gating. The broad background generated under one-photon excitation has a distinct lifetime and can be discriminated given a timing mechanism in the detection pathway. Such a gating technique has previously been demonstrated in single molecule luminescence [99].

Finally, light generated under nonlinear excitation emerges quasi-instantaneously and does not involve any metastable intermediate state which could be modified by changes in the particle or the environment. Nevertheless, the fact that nonlinear white-light hot spots do not blink challenges the notion of blinking in single molecule Raman scattering [8], itself a quasi-instantaneous process without the involvement of metastable states. Perhaps the reason that single molecule SERS can show blinking, whereas other nanoscale instantaneous light scattering phenomena do not, lies in the inherent local dissipation of energy through activated vibrational modes, as was recently speculated [100]. Nevertheless, it is worth noting that it is, in principle, possible to carry out single molecule SERS without perturbation by blinking [11], suggesting that blinking is actually an extrinsic process not related to the specifics of the molecule under investigation.

4.6 Conclusions

Localized surface plasmon polariton modes of silver nanoparticles and their aggregates can dramatically raise the local electromagnetic field strength and mode density in nanoscale regions called hot spots [18–20, 25, 45, 47, 48, 74]. Within these hot spots the coupling of radiation to a material as well as the coupling of radiation generated by the material to the far field is greatly enhanced [101]. The most prolific manifestation of this process is SERS, which makes a powerful material finger-printing tool accessible at the single-molecule level. While SERS is an attractive analysis technique, it can be plagued by blinking, a broad background, and an extreme sensitivity to contamination, besides raising questions regarding the complete understanding of the enhancement mechanism. In this work, we extensively studied the intrinsic linear and nonlinear optical response of SERS-active silver nanoparticle films created with the Tollens reagent reaction. By comparing and contrasting the two processes we develop a picture of the intrinsic photodynamics of these films that is based upon emissive silver clusters that interact with the hot spots of the localized surface-plasmon modes. The results have important implications for further understanding and improving of SERS as a reliable analysis technique.

We showed that the linear and nonlinear responses of the silver films are excited through the same surface-enhanced pathways: the efficiency of both processes depends upon film morphology; linearly and nonlinearly excited emission come from discrete diffraction-limited spots; and excitation polarization anisotropy clearly demonstrates that the excitation occurs via localized surface plasmon modes. On the other hand, the different characteristics between the linear and nonlinear hot spots reveal that the emission origins are different. Photo-activation, emission spectra, blinking, spectral fluctuations, and decay characteristics indicate that the linear response arises from a combination of SERS from, most likely, carbon contamination and luminescence from small silver clusters that are photogenerated from the native silver oxide content of the film. In contrast to the linear hot spots, the nonlinear hot spots show different emission spectra, stable emission, instantaneous emission decay, and a variable power dependence but share the photo-activation trait leading us to conclude that the

emission arises from potentially coherent nonlinear scattering of larger silver clusters, which do not fluoresce. It is clear from these differences that the nonlinear emission does not simply arise from multiphoton excitation of the linear process.

The host of linear and nonlinear emission characteristics and the potential presence of emissive silver clusters have important implications for SERS. The linear emission characteristics demonstrate that the broad background commonly seen with SERS is likely due to emissive silver clusters. The lack of blinking for the nonlinear emission implies that SERS blinking is a property of the analyte and not of the enhancement mechanism. This stability makes the nonlinear emission useful as broadband white-light beacons for high-resolution transmission microscopy, as we recently demonstrated in single-domain spectroscopy of biological photonic crystals [56]. Further, the fact that background-free single-molecule SERS spectra can be detected suggests that a similar spatial anticorrelation may exist for the linear emission as was found for the nonlinear emission [10]. Such correlations may provide an avenue for predicting the positions, quantity, and quality of SERS hot spots. The presence of silver clusters generated from native silver oxide layers in or around the vicinity of SERS hot spots could be a crucial key to accurate analysis of chemical enhancement mechanisms.

The results presented here establish a new set of questions to investigate. One of the biggest puzzles arising from our investigations lies in the spectral dynamics of the two processes and how they relate to the fluctuations of SERS. While the exact origins of the fluctuations in the linearly excited emission remain unknown, they may be related to the blinking of SHG from the hot spots that we previously reported [72]. Future experiments should address the dynamics of one-photon induced luminescence. Another important step to take is to confidently determine whether or not a spatial anticorrelation exists between the intrinsic linear emission and SERS hot spots. Finally, well-correlated electron microscopy and optical microscopy of the hot spots is incredibly challenging, but could provide unprecedented insight into how the intrinsic optical response relates to SERS and the physical arrangement of matter within the hot spots, and may even ultimately explicitly confirm the emissive silver cluster model proposed here.

4.7 Acknowledgements

We thank Manfred Walter for helpful discussions, and Dr. Randy Polson and Dr. Matt Delong for assistance with the SEM measurements. Financial support from the Research Corporation for the Advancement of Science (Scialog program) is gratefully acknowledged, as is a Fellowship in Science and Engineering from the David & Lucile Packard Foundation.

4.8 References

[1] A. M. Michaels, M. Nirmal, and L. E. Brus, J. Am. Chem. Soc. **121**, 9932 (1999).

[2] S. M. Nie and S. R. Emery, Science **275**, 1102 (1997).

[3] K. Kneipp et al., Phys. Rev. Lett. **78**, 1667 (1997).

[4] A. R. Bizzarri and S. Cannistraro, Chem. Phys. **290**, 297 (2003).

[5] H. X. Xu, E. J. Bjerneld, M. Kall, and L. Borjesson, Phys. Rev. Lett. **83**, 4357 (1999).

[6] N. P. W. Pieczonka and R. F. Aroca, ChemPhysChem **6**, 2473 (2005).

[7] J. Jiang, K. Bosnick, M. Maillard, and L. Brus, J. Phys. Chem. B **107**, 9964 (2003).

[8] A. R. Bizzarri and S. Cannistraro, Phys. Chem. Chem. Phys. **9**, 5315 (2007).

[9] P. G. Etchegoin and E. C. Le Ru, Phys. Chem. Chem. Phys. **10**, 6079 (2008).

[10] M. J. Walter, N. J. Borys, G. Gaefke, S. Höger, and J. M. Lupton, J. Am. Chem. Soc. **130**, 16830 (2008).

[11] M. J. Walter et al., Phys. Rev. Lett. **98**, 137401 (2007).

[12] K. A. Bosnick, J. Jiang, and L. E. Brus, J. Phys. Chem. B **106**, 8096 (2002).

[13] L. Brus, Acc. Chem. Res. **41**, 1742 (2008).

[14] J. P. Camden et al., J. Am. Chem. Soc. **130**, 12616 (2008).

[15] J. A. Dieringer, R. B. Lettan, K. A. Scheidt, and R. P. Van Duyne, J. Am. Chem. Soc. **129**, 16249 (2007).

[16] D. P. Tsai et al., Phys. Rev. Lett. **72**, 4149 (1994).

[17] V. M. Shalaev and A. K. Sarychev, Phys. Rev. B **57**, 13265 (1998).

[18] S. Gresillon et al., Phys. Rev. Lett. **82**, 4520 (1999).

[19] A. K. Sarychev, V. A. Shubin, and V. M. Shalaev, Phys. Rev. B **60**, 16389 (1999).

[20] P. Gadenne et al., Physica B **279**, 52 (2000).

[21] M. Breit et al., Phys. Rev. B **64**, 125106 (2001).

[22] M. A. van Dijk, M. Lippitz, and M. Orrit, Acc. Chem. Res. **38**, 594 (2005).

[23] V. P. Safonov et al., Phys. Rev. Lett. **80**, 1102 (1998).

[24] M. I. Stockman, S. V. Faleev, and D. J. Bergman, Phys. Rev. Lett. **87**, 167401 (2001).

[25] S. Ducourtieux et al., J. Nonlinear Opt. Phys. Mater. **9**, 105 (2000).

[26] M. Moskovits, Rev. Mod. Phys. **57**, 783 (1985).

[27] L. A. Peyser, A. E. Vinson, A. P. Bartko, and R. M. Dickson, Science **291**, 103 (2001).

[28] P. C. Andersen, M. L. Jacobson, and K. L. Rowlen, J. Phys. Chem. B **108**, 2148 (2004).

[29] G. T. Boyd, Z. H. Yu, and Y. R. Shen, Phys. Rev. B **33**, 7923 (1986).

[30] V. A. Markel, L. S. Muratov, M. I. Stockman, and T. F. George, Phys. Rev. B **43**, 8183 (1991).

[31] W. Chen, A. G. Joly, and J. Roark, Phys. Rev. B **65**, 245404 (2002).

[32] Y. Dai et al., Chem. Phys. Lett. **439**, 81 (2007).

[33] E. Dulkeith et al., Phys. Rev. B **70**, 205424 (2004).

[34] C. D. Geddes, A. Parfenov, I. Gryczynski, and J. R. Lakowicz, J. Phys. Chem. B **107**, 9989 (2003).

[35] C. D. Geddes, A. Parfenov, I. Gryczynski, and J. R. Lakowicz, Chem. Phys. Lett. **380**, 269 (2003).

[36] A. Maali, T. Cardinal, and M. Treguer-Delapierre, Physica E **17**, 559 (2003).

[37] M. Treguer et al., Solid State Sci. **7**, 812 (2005).

[38] J. P. Wilcoxon, J. E. Martin, F. Parsapour, B. Wiedenman, and D. F. Kelley, J. Chem. Phys. **108**, 9137 (1998).

[39] J. Zheng, Y. Ding, B. Z. Tian, Z. L. Wang, and X. W. Zhuang, J. Am. Chem. Soc. **130**, 10472 (2008).

[40] G. Zhu, V. I. Gavrilenko, and M. A. Noginov, J. Chem. Phys. **127**, 104503 (2007).

[41] M. Eichelbaum, J. Kneipp, B. E. Schmidt, U. Panne, and K. Rademann, ChemPhysChem **9**, 2163 (2008).

[42] M. L. Jacobson and K. L. Rowlen, Chem. Phys. Lett. **401**, 52 (2005).

[43] A. V. Aiboushev et al., Phys. Lett. A **372**, 5193 (2008).

[44] A. Bouhelier et al., Phys. Rev. Lett. **95**, 267405 (2005).

[45] E. Y. Poliakov, V. A. Markel, V. M. Shalaev, and R. Botet, Phys. Rev. B **57**, 14901 (1998).

[46] K. Seal et al., Phys. Rev. Lett. **94**, 226101 (2005).

[47] V. A. Markel et al., Phys. Rev. B **59**, 10903 (1999).

[48] S. Ducourtieux et al., Phys. Rev. B **64**, 165403 (2001).

[49] J. P. Heritage, J. G. Bergman, A. Pinczuk, and J. M. Worlock, Chem. Phys. Lett. **67**, 229 (1979).

[50] C. K. Chen, A. R. B. Decastro, and Y. R. Shen, Phys. Rev. Lett. **46**, 145 (1981).

[51] C. K. Chen, T. F. Heinz, D. Ricard, and Y. R. Shen, Phys. Rev. B **27**, 1965 (1983).

[52] A. Mooradian, Phys. Rev. Lett. **22**, 185 (1969).

[53] R. L. Birke, J. R. Lombardi, and J. I. Gersten, Phys. Rev. Lett. **43**, 71 (1979).

[54] W. L. Barnes, A. Dereux, and T. W. Ebbesen, Nature **424**, 824 (2003).

[55] J. N. Anker et al., Nat. Mater. **7**, 442 (2008).

[56] D. Chaudhuri et al., Nano Lett. **9**, 952 (2009).

[57] Y. Saito, J. J. Wang, D. A. Smith, and D. N. Batchelder, Langmuir **18**, 2959 (2002).

[58] Z. J. Wang, S. L. Pan, T. D. Krauss, H. Du, and L. J. Rothberg, Proc. Natl. Acad. Sci. U. S. A. **100**, 8638 (2003).

[59] Z. J. Wang and L. J. Rothberg, J. Phys. Chem. B **109**, 3387 (2005).

[60] Z. Wang and L. J. Rothberg, Appl. Phys. B **84**, 289 (2006).

[61] S. Link and M. A. El-Sayed, Annu. Rev. Phys. Chem. **54**, 331 (2003).

[62] F. Hache, D. Ricard, and C. Flytzanis, J. Opt. Soc. Am. B **3**, 1647 (1986).

[63] O. A. Aktsipetrov, P. V. Elyutin, A. A. Nikulin, and E. A. Ostrovskaya, Phys. Rev. B **51**, 17591 (1995).

[64] L. L. Jensen and L. Jensen, J. Phys. Chem. C **112**, 15697 (2008).

[65] H. Harutyunyan, S. Palomba, J. Renger, R. Quidant, and L. Novotny, Nano Lett. **10**, 5076 (2010).

[66] V. P. Drachev et al., J. Mod. Opt. **49**, 645 (2002).

[67] H. J. Simon, D. E. Mitchell, and J. G. Watson, Phys. Rev. Lett. **33**, 1531 (1974).

[68] S. I. Bozhevolnyi, J. Beermann, and V. Coello, Phys. Rev. Lett. **90**, 197403 (2003).

[69] J. Beermann and S. I. Bozhevolnyi, Phys. Rev. B **69**, 155429 (2004).

[70] M. I. Stockman, D. J. Bergman, C. Anceau, S. Brasselet, and J. Zyss, Phys. Rev. Lett. **92**, 057402 (2004).

[71] T. Zentgraf, A. Christ, J. Kuhl, and H. Giessen, Phys. Rev. Lett. **93**, 243901 (2004).

[72] N. J. Borys, M. J. Walter, and J. M. Lupton, Phys. Rev. B **80**, 161407 (2009).

[73] P. V. Kamat, J. Phys. Chem. B **106**, 7729 (2002).

[74] P. Johansson, H. X. Xu, and M. Kall, Phys. Rev. B **72**, 035427 (2005).

[75] O. L. A. Monti, J. T. Fourkas, and D. J. Nesbitt, J. Phys. Chem. B **108**, 1604 (2004).

[76] W. E. Moerner and M. Orrit, Science **283**, 1670 (1999).

[77] K. L. Norrod and K. L. Rowlen, Anal. Chem. **70**, 4218 (1998).

[78] M. L. Jacobson and K. L. Rowlen, J. Phys. Chem. B **110**, 19491 (2006).

[79] A. M. Moran, J. H. Sung, E. M. Hicks, R. P. Van Duyne, and K. G. Spears, J. Phys. Chem. B **109**, 4501 (2005).

[80] M. Lippitz, F. Kulzer, and M. Orrit, ChemPhysChem **6**, 770 (2005).

[81] P. Zolotavin et al., Chem. Phys. Lett. **457**, 342 (2008).

[82] L. Novotny and B. Hecht, *Principles of Nano-Optics*, Cambridge University Press, New York, 2006.

[83] J. I. Gonzalez, T. Vosch, and R. M. Dickson, Phys. Rev. B **74**, 235404 (2006).

[84] S. A. Patel et al., J. Phys. Chem. C **113**, 20264 (2009).

[85] V. P. Drachev et al., Phys. Rev. B **69**, 035318 (2004).

[86] M. R. Beversluis, A. Bouhelier, and L. Novotny, Phys. Rev. B **68**, 115433 (2003).

[87] J. M. Dudley, G. Genty, and S. Coen, Rev. Mod. Phys. **78**, 1135 (2006).

[88] E. Burstein, Y. J. Chen, C. Y. Chen, S. Lundquist, and E. Tosatti, Solid State Commun. **29**, 567 (1979).

[89] A. Otto, Surf. Sci. **75**, L392 (1978).

[90] A. Weiss and G. Haran, J. Phys. Chem. B **105**, 12348 (2001).

[91] A. A. Moore, M. L. Jacobson, N. Belabas, K. L. Rowlen, and D. M. Jonas, J. Am. Chem. Soc. **127**, 7292 (2005).

[92] T. Itoh et al., J. Photochem. Photobiol., A **183**, 322 (2006).

[93] T. Itoh et al., J. Phys. Chem. B **110**, 21536 (2006).

[94] T. Itoh et al., J. Chem. Phys. **124**, 134708 (2006).

[95] E. C. Le Ru et al., J. Phys. Chem. C **111**, 16076 (2007).

[96] W. E. Doering and S. M. Nie, J. Phys. Chem. B **106**, 311 (2002).

[97] E. D. Diebold, P. Peng, and E. Mazur, J. Am. Chem. Soc. **131**, 16356 (2009).

[98] Y. Fang, N. H. Seong, and D. D. Dlott, Science **321**, 388 (2008).

[99] K. Becker and J. M. Lupton, J. Am. Chem. Soc. **128**, 6468 (2006).

[100] M. Ringler et al., Nano Lett. **7**, 2753 (2007).

[101] J. R. Lakowicz et al., Anal. Biochem. **301**, 261 (2002).

CHAPTER 5

THE ROLE OF PARTICLE MORPHOLOGY IN INTERFACIAL ENERGY TRANSFER IN CDSE/CDS HETEROSTRUCTURE NANOCRYSTALS

Semiconductor heterostructure nanoparticles possess electronic properties that are easily tunable with material selection, particle size, and particle shape. CdSe/CdS core-shell nanoparticles, in particular, act as model light-harvesting systems where optical energy absorbed by the CdS shell is "funneled" into the CdSe core therefore making them intriguing model systems to study with regards to photovoltaics or photocatalysis. In this chapter, the role of nanoparticle shape on the electronic properties of CdSe/CdS heterostructures is probed on near-spherical, rod, and tetrapod morphologies. The results both explicitly illustrate how shape anisotropy affects the electronic properties and identify potential interfacial barriers in the heterostructure that interrupt the energy transfer to the core.

This chapter is taken from a manuscript published in 2010 by *Science* on page 1371 of volume 330. It was coauthored by Manfred J. Walter and John M. Lupton who made the initial classification discovery as well as Jing Huang and Dmitri V. Talapin who synthesized the colloidal nanoparticle samples.[1] Subsection headings have been added for structural clarity and are not present in the original manuscript.

---

[1]Reproduced with permission from N. J. Borys, M. J. Walter, J. Huang, D. V. Talapin, and J. M. Lupton; The role of particle morphology in interfacial energy transfer in CdSe/CdS heterostructure nanocrystals; Science 330, 1371 (2010).

5.1 Abstract

Nanoscale semiconductor heterostructures such as tetrapods can be used to mimic light-harvesting processes. We used single-particle light-harvesting action spectroscopy to probe the impact of particle morphology on energy transfer and carrier relaxation across a heterojunction. The generic form of an action spectrum [in our experiments, photoluminescence excitation (PLE) under absorption in CdS and emission from CdSe in nanocrystal tetrapods, rods, and spheres] was controlled by the physical shape and resulting morphological variation in the quantum confinement parameters of the nanoparticle. A correlation between single-particle PLE and physical shape as determined by scanning electron microscopy was demonstrated. Such an analysis links local structural nonuniformities such as CdS bulbs forming around the CdSe core in CdSe/CdS nanorods to a lower probability of manifesting excitation energydependent emission spectra, which in turn is probably related to band alignment and electron delocalization at the heterojunction interface.

5.2 Introduction

Advances in the synthesis of semiconductor nanoparticles have enabled exquisite control over composition and shape, yielding spherical, linear [1, 2], and branched structures such as tetrapods [3–5]. Although many semiconductor nanoparticles originally consisted of only one material, further opportunities for tailoring electronic functionalities are anticipated from nanoscale semiconductor heterostructures combining two or more materials [5]. Indeed, a host of applications has emerged from precise control over nanostructure functionality, ranging from photovoltaics [2, 6] to commercial lightemitting devices. A microscopic understanding of the migration of excitation energy in heterojunctions and the resulting interfacial charge transfer [7] is particularly important in developing photocatalytic compounds to split water [8] or reduce CO_2 [9]. Due to only a slight mismatch in the lattice constants of the two materials, yet well contrasted band gaps, the CdSe/CdS heterostructure has evolved as one of the workhorses for relating nanoparticle synthesis and shape to spectroscopic properties. Here we describe an optical classification of the quantum

confinement in complex CdSe/CdS core/shell nanostructures by means of single-particle light-harvesting action spectroscopy, a versatile noncontact tool to measure electron transport or energy transfer on mesoscopic length scales [10]. For a variety of nanostructure shapes, we probed the photoluminescence excitation (PLE) of the absorbing CdS through emission from the lower-gap CdSe.We identified two distinct categories of action spectra, characteristic of the physical shape and quantum confinement parameters of the semiconductor heterostructures, and showed how the energetic landscape can inhibit complete electron transfer across the CdSe/CdS interface. This single-particle classification highlights the sensitivity of ensemble performance, such as in light-harvesting, to morphological characteristics that affect the intrinsic nature of the interfaces, thereby suggesting routes to future synthetic optimization.

Large optical absorption cross sections, enhanced stability, high quantum yields, and size-tunable electronic structure make semiconductor nanocrystals particularly interesting for light-harvesting and energy conversion applications [2,6]. Nevertheless, there is still no clear consensus on the microscopic nature of interfacial energy levels and the process of carrier migration from one semiconductor to another. Very similar CdSe/CdS nanostructures can exhibit properties of either a type I heterostructure, in which both electron and positively charged hole are confined to one material, or a type II heterostructure, in which electron and hole separate between the materials [11–14]. Naturally, such a distinction is crucial to choosing the correct material for a particular application: Light emission requires type I junctions, whereas charge separation in photovoltaics requires type II [13]. Such knowledge of the interface is crucial for designing nanoparticle superstructures, such as inorganic dendrimers with a treelike branched architecture, with superior light-harvesting properties. A first step to such a structure is the heterojunction tetrapod [5].

Semiconductor nanoparticles are well suited to microscopic optical studies, which have revealed a surprising diversity in electronic properties between particles that are typically masked in ensemble-level measurements [15]. Htoon *et al.*, for example, uncovered both discrete excitonic states and a quasicontinuum in the core of spherical CdSe particles capped with a ZnS shell [16]. We probed energetic relaxation in

individual CdSe/CdS nanoheterostructures of different shapes after optical excitation of the higher-gap CdS. This approach, leveraging single-particle PLE over a wide spectral range, illuminates the nature of both the high-gap material absorption and the subsequent intraparticle relaxation process, which are both ultimately crucial in designing light-harvesting applications [6]. In contrast, most single-quantumstructure PLE spectroscopy [16–18] to date has been carried out over relatively narrow spectral ranges to probe distinct excitonic features, or else has analyzed excitation enhancement by metal nanoparticles at discrete wavelengths [19].

5.3 Results and discussion

We focused our attention on CdSe/CdS tetrapods, which are inorganic light-harvesting complexes with very large absorption cross sections, which make them easily visible in single-particle measurements. A schematic of a CdSe/CdS tetrapod nanoparticle and a suggestive band diagram [20] are shown in the inset of Fig. 5.1. The structures consist of a CdSe core approximately 4 nm in diameter, which is surrounded by an antenna-like CdS shell. The shell has four arms that are 20 nm in length and 6 nm in diameter. We purified the tetrapod solution to an ensemble composition of at least 90% tetrapods, which appeared to be geometrically uniform in transmission electron microscopy (TEM) (See Section 5.5 and Ref. [5]). Previous comparisons of theory and experiment have indicated that, on average, the CdSe/CdS interface should form a quasi-type II heterostructure, with an excited electron delocalizing over the CdSe and CdS conduction bands and the associated hole localizing on the lower-gap CdSe core [14]. Initial studies on the tetrapods have suggested a similar electronic structure [20], although the energy offsets are such that a range of interfacial localization phenomena is conceivable [13]: It is not straightforward to extrapolate band diagrams derived from bulk material parameters to solution-grown nanostructures. For these heterostructures, at energies above the CdS fundamental absorption edge, the CdS extinction dwarfs that of the CdSe, thus resulting in an absorption spectrum dominated by the CdS. The electronic structure, on the other hand, yields a luminescence spectrum arising from recombination in CdSe [5,21]. The

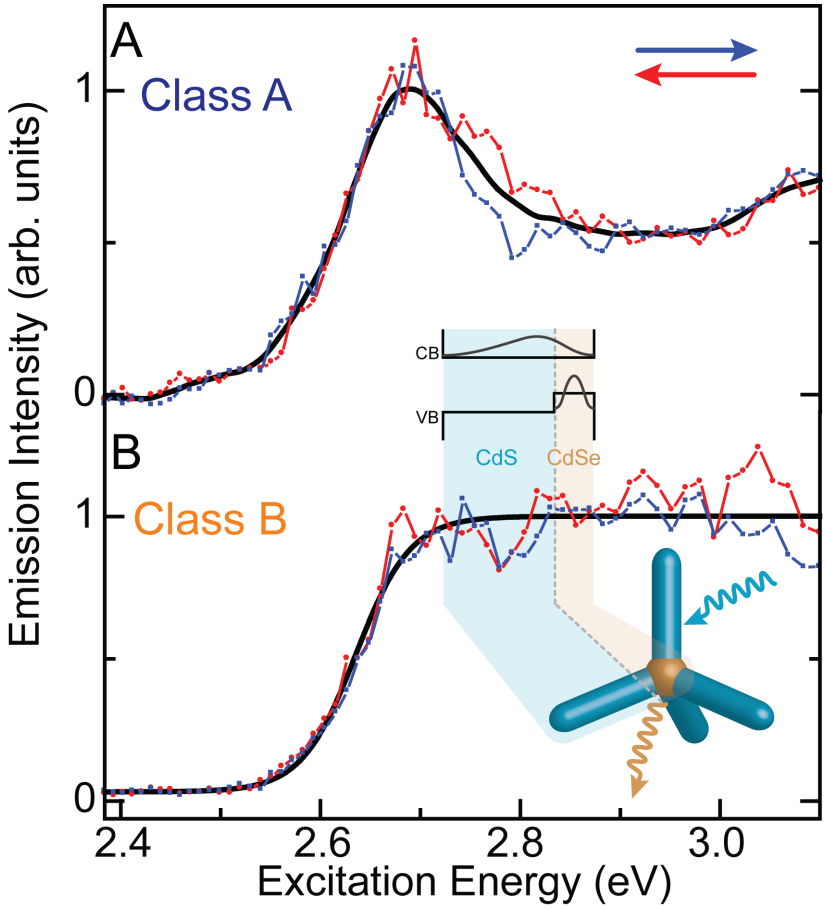

Figure 5.1. Light-harvesting action spectroscopy at 4 K of two single semiconductor tetrapods consisting of a lowgap CdSe core and high-gap CdS arms. The nanoparticles are excited primarily above the CdS absorption edge, and emission is detected from the CdSe core. A sketch of the assumed electron and hole probability density distribution within the electronic band structure is shown in the inset in the middle. (A) For the first particle, the onset of absorption from the quantum-confined CdS exciton gives rise to a distinct peak that is then followed by absorption into a continuum of states at higher energy (red, scan downward in energy; blue, scan upward). (B) For the second particle, the peak associated with the CdS exciton is not present, and the spectrum is marked by a continuum of states after the onset of CdS absorption (the black lines are a guide to the eye).

similarity of the ensemble nanoparticle PLE and absorption spectra indicates that this light-harvesting process is highly efficient [5]. We expect the prominent onset of the PLE to correspond with the quantum-confined exciton of the CdS, followed by the typical continuum of higher energy states.

Such behavior was indeed observed in single-particle light-harvesting action at 4 K in Fig. 5.1A. We recorded the CdSe emission intensity while sweeping the laser excitation both down and up in energy (see Section 5.5). The particle exhibited a clear peak in the CdS absorption that can be attributed to the quantum-confined excitonic transition [22, 23]. We refer to PLE spectra with such behavior as class A. A second single tetrapod showed strikingly different behavior depicted in Fig. 5.1B, revealing particle-to-particle variations that are masked in ensemble measurements. In this case, there is no clear peak after the CdS absorption onset. We term these PLE spectra class B. Both classes were repeatedly observed in spatial proximity during the same excitation scan.

Although the tetrapods perform the desired light-harvesting function, they do not offer the best system in which to search for structural origins of the distinct PLE classification. We therefore used two further model systems to study the influence of particle form on PLE: nanorods, which mimic one arm and the core of the tetrapod; and nanospheres with a thick CdS shell. All structures had a similar CdSe core that was 4 nm in diameter. Figure 5.2 shows single-particle spectra of 150 tetrapod, 150 rod, and 75 near-spherical nanoheterostructures, normalized to the CdS absorption onset. Representative TEM images for each nanostructure are shown in the lower insets. The rods consist of a CdS arm 60 nm in length and approximately 6 nm in diameter surrounding the CdSe core. TEM indicated that the sample contained two general shapes of rods: rods that have a constant diameter over their length and those that have a bulb feature surrounding the CdSe core, resulting in a nonuniform rod diameter [11, 21]. Finally, the CdS shell for the near-spherical structures was a 4-nm thick layer surrounding the CdSe core. TEM of these particles revealed that the thick CdS shell results in a non-uniform distribution of particles with anisotropic deviations from a perfect sphere. For the tetrapods and rods, each single-particle PLE

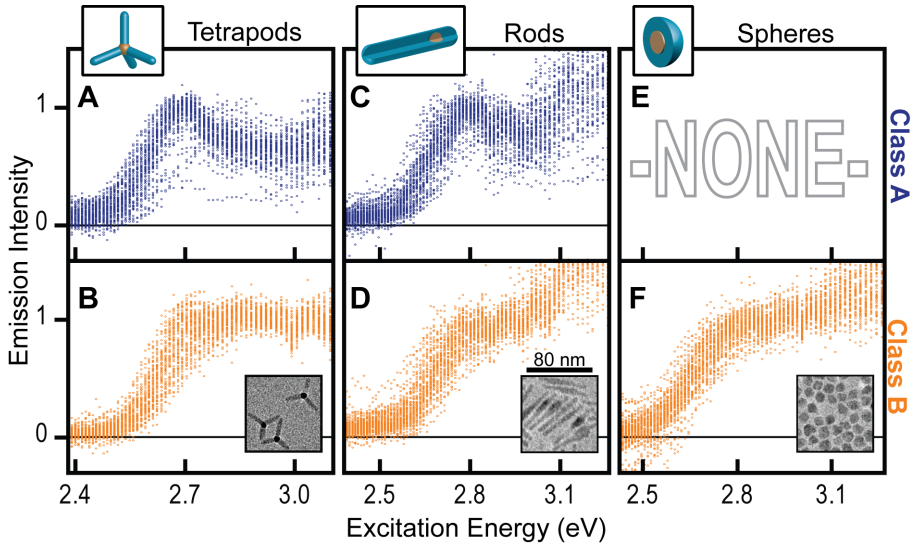

Figure 5.2. Classification of single-particle light-harvesting action spectra for tetrapod, rod, and near-spherical nanoheterostructures. A total of 150, 150, and 75 raw spectra for tetrapods, rods, and spheres, respectively, are sorted into two groups. All curves are normalized to the CdS absorption onset intensity but are otherwise not manipulated. (A and B) 75 class A and 75 class B single-particle PLE spectra from tetrapod structures. (C and D) 75 class A and 75 class B single-particle PLE spectra from rod structures. (E and F) The near-spherical structures show only class B single-particle PLE spectra. Inset in (B) to (F) are representative TEM images of the tetrapods, rods, and spheres. Although the tetrapods appear uniform, the rod ensemble manifests two morphologies: one with a uniform diameter and the other with a pronounced bulb feature. The near-sperical structures are non-uniform in their deviations from isotropy.

spectrum can generally be categorized as class A (Fig. 5.2, A and C, respectively) or class B (Fig. 5.2, B and D, respectively). In contrast, we observed exclusively class B spectra for the near-spherical structures (Fig. 5.2F). We conclude that the origin of the different classes is not found in the combination of constituent materials but is related to the shape of the nanocrystal, which determines the symmetry of the confinement potential. Other approaches to representing the raw data, along with quantitative thresholds for differentiating between the two classes, are discussed in Section 5.5.4.

Through its relation to the quantum confinement effect, physical shape plays a crucial role in the optical and electronic properties of semiconductor nanocrystals

[13,22,24]. For the rods, where quantum confinement in the CdS is influenced mostly by diameter [25], the bulb structures consist of a range of diameters that will smear out the excitonic transition and will likely lead to particles with a class B spectrum. The same effect of shape variations in the direction of radial quantum confinement could also give rise to exclusively class B spectra in the near-spherical particles. In addition, quantum confinement in absorption in these particles may be weaker as the larger particle diameters approach the Bohr exciton radius in CdS, thus reducing the visibility of excitonic transitions.

To verify the role that shape plays in the PLE spectrum of a single nanocrystal, we correlated PLE measurements with scanning electron microscopy (SEM) of single rods. The correlation process is discussed in Section 5.5.6. Figure 5.3 shows 12 PLE spectra and the SEM images of the corresponding nanorods. The pairs were selected

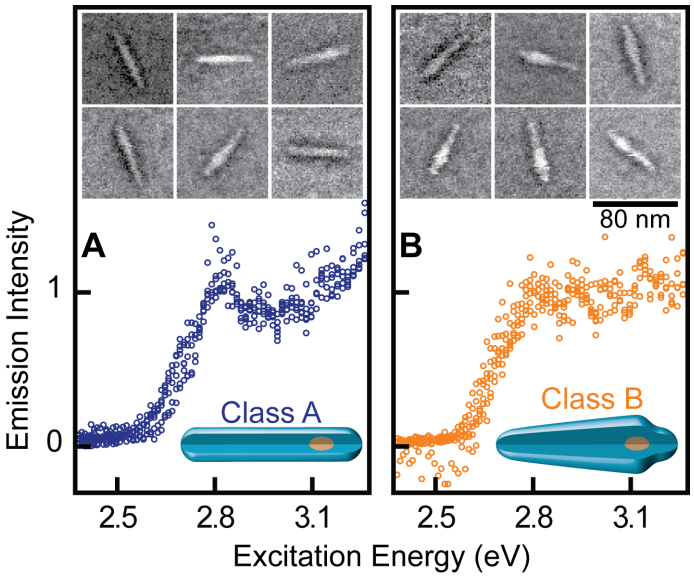

Figure 5.3. Correlated SEM and PLE spectra of 12 single CdSe/CdS nanorods. (A) Six class A PLE spectra normalized to the CdS onset and plotted together with their corresponding SEM images, representative of rods with a uniform diameter (cartoon at bottom). (B) The SEM images of six rods that exhibit a class B PLE spectrum indicate that the spectral shape is attributable to rods that have a pronounced bulb feature and non-uniform diameter as sketched schematically in the cartoon. All correlated image-PLE pairs were chosen solely on the basis of the quality of the PLE spectrum, without any knowledge of the corresponding SEM image.

solely on the basis of the quality of the PLE spectrum over up and down sweeps without any knowledge of the corresponding image. Figure 5.3A shows six class A PLE spectra normalized and plotted together; Fig. 5.3B shows six class B spectra. Inset in the plot are the corresponding SEM images. A clear trend that confirms the shape hypothesis is observable: All of the rods in Fig. 5.3A exhibit a class A PLE spectrum, and five out of six have a uniform diameter over the length of the rod. On the other hand, in Fig. 5.3B, all of the rods exhibit a class B PLE spectrum and have a pronounced bulb feature as anticipated (see Section 5.5.6 for a discussion of the geometric thresholds invoked). These observations are consistent with single-particle PL (Section 5.5.7),which demonstrates that rods with a class A PLE spectrum have higher-energy residual CdS emission due to their smaller diameters (stronger quantum confinement) than rods with a class B PLE spectrum. The basic statistical analysis presented in Section 5.5.8 indicates that the probability of the results in Fig. 5.3 occurring by chance is 0.3%.

The similarity in PLE and emission spectra of rods, spheres, and tetrapods suggests that excessive CdS growth around the core could be responsible for the formation of two distinct spectroscopic classes of tetrapods. In addition, variations in effective arm diameter within a single tetrapod [20] or, quite generally, variations in intraparticle CdS-CdSe coupling strength that disrupt the particle symmetry, could lead to a loss of excitonic structure in PLE. We therefore propose that the single-particle PLE can serve as a predictor of particle morphology and indeed provides insight into the tetrapod shape, which is hard to obtain by other means.

Bulblike particle morphologies probably have featureless PLE spectra because the CdS shell is not defined by one fixed diameter, and therefore a range of excitonic transition energies exists. This morphological disorder within a single particle also appears to affect band alignment within the heterojunction, as revealed by spectrally resolving tetrapod emission as a function of excitation energy for 50 single tetrapods. Of these tetrapods, 26% [13 tetrapods (Section 5.5.9)] showed a surprising dependence of the tetrapod emission energy on the excitation energy. Three such cases are detailed in Fig. 5.4.

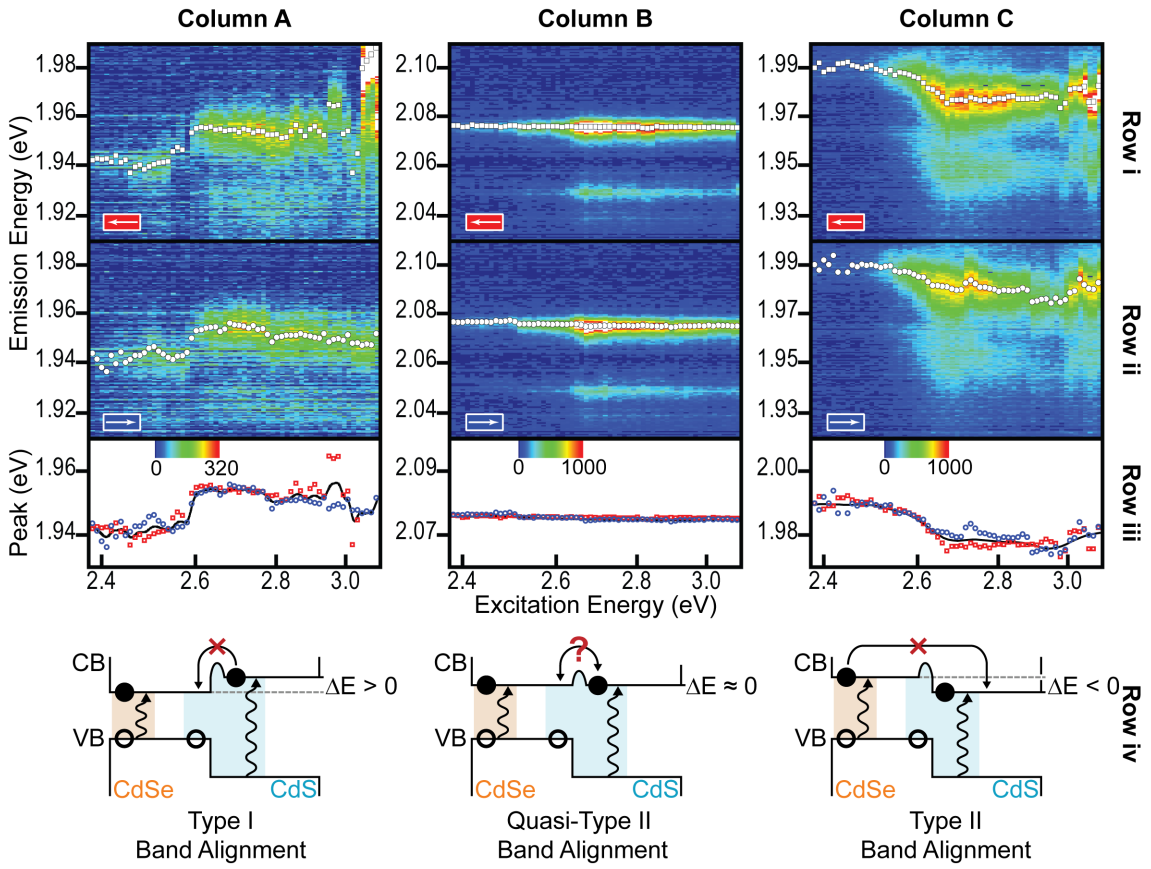

Figure 5.4. Single-particle emission spectra as a function of excitation energy for three individual class A tetrapods, revealing the possible band alignment schemes. (Column A) The emission spectrum shifts to higher energies as the excitation energy is raised. Two-dimensional plots of emission as a function of excitation are shown for the laser sweep downward (Row i) and upward (Row ii) in energy. The main emission peak energy, extracted by fitting two Gaussians to the emission spectrum, is overlaid as white circles. (Row iii) The peak position as a function of excitation energy shows a step-like shift of ∼10 meV close to the absorption onset of CdS at 2.6 eV. (Row iv) This situation can be rationalized in terms of a type I band alignment, where a barrier to thermalization of the electron from the CdS to the CdSe exists. Below 2.6 eV, direct excitation of the CdSe core occurs, whereas emission at higher excitation energies results from an interfacial exciton. (Column B) No spectral shift is seen with excitation energy, suggesting a quasitype II band alignment. By analogy to column A, it is conceivable that a barrier to electron transfer between CdS and CdSe also exists due to, for example, lattice strain. (Column C) The type II band alignment is characterized by a shift of emission to lower energies as the excitation energy is raised from absorption in the CdSe core to the CdS shell. A barrier to electron transfer from CdSe to CdS must exist to prevent the core electron from transferring to the shell under excitation of the core. The black lines in the peak position plots are smoothed averages that serve as a guide for the eye.

The particle in column A of Fig. 5.4 exhibits a shift in emission to higher energy as the excitation energy is raised, although the shape of the emission spectrum remains characterized by the CdSe electronic transition and its phonon sideband. It is important to consider both sweep directions of the exciting laser because nanocrystals exhibit random spectral diffusion [26]; the spectral changes are reversible upon downward (row i) and upward (row ii) sweeps. Row iii of column A plots the PL peak energy, which shows a distinct jump at an excitation energy of 2.6 eV. The position of the spectral jump corresponds to the onset of CdS absorption at 4 K and indicates a transition from direct excitation of the CdSe core to excitation of the CdS arm and subsequent relaxation to the CdSe. In contrast, the particle in column B exhibits emission independent of excitation. This case would be expected for a semiconductor heterostructure in which the high-energy electron-hole pair formed in the wide-gap semiconductor (CdS) relaxes down to the narrower-gap CdSe. Finally, in column C, the emission energy decreases with increasing excitation energy. As in column A, a change in the emission peak is observed around excitation at 2.6 eV.

To rationalize these observations, we consider the subtleties of conduction and valence band offsets between CdSe and CdS in row iv of Fig. 5.4. Studies of CdSe/CdS nanoparticles at the ensemble level have suggested that the CdSe valence band is consistently higher in energy than that of the CdS, although the conduction band alignment of the two materials is sensitive to nanoparticle geometry and may result in a type I, type II, or quasi-type II electronic structure (see sketches in Fig. 5.4 for definition) [11–13]. Such band offsets will affect the emission spectrum if a barrier in the conduction band inhibits electron transfer between CdS and CdSe, which is conceivable given the interfacial strain due to the lattice mismatch of the two materials [27]. We propose that the tetrapods in columns A and C of Fig. 5.4 are characterized by conduction band offsets ΔE, so that at least two distinct exciton states exist: CdSe core excitons and CdSe/CdS interfacial excitons. Because both states are emissive and hence stable, an interfacial barrier must be present, which prevents complete electron transfer to the lowest state in the conduction band, thereby impeding thermalization of the emissive exciton. A barrier to electron transfer must also exist in the situation

in column C, because the excited electron does not thermalize to the lower-level CdS conduction band under direct excitation of the core. By analogy, the barrier to electron delocalization could also be present for tetrapods in which the absence of a shift in emission energy indicates conduction band alignment. The barrier can only exist for one of the carriers, because complete blocking at the interface would result in recombination in the CdS arm, which is spectrally distinct (Section 5.5.7). Noting that our spectroscopy cannot distinguish between conduction and valence band blocking, we follow the earlier assignment of effective hole localization in the core of CdSe/CdS nanoparticles because of a larger offset in the valence band than in the conduction band [28]. We speculate that the greater effectiveness of hole transfer across the interface as compared to electron transfer could arise from the difference in wave function symmetry of the carrier species, or result from the much larger energy-level offset.

The observation that excitation energies well above the band gap of both CdSe and CdS (that is, at 3.1 eV) do not result in complete thermalization and thus emission at the lowest energy of the system (Fig. 5.4, column A), which is only observed under direct core excitation, indicates that additional excitation energy does not play a role in electron transfer to the core. The CdS electron therefore cools before the CdSe/CdS interfacial exciton is formed. Our preliminary statistics on the PLE spectra (Section 5.5.9) indicate that excitation energy-dependent emission is much more prominent in class A tetrapods. This observation is again consistent with the implied morphological disorder of the single class B tetrapod structures, because more narrowly defined (class A) energy levels should be more susceptible to band misalignment at the heterojunction.

5.4 Conclusions

Single-particle light-harvesting action thus reveals distinct spectroscopic behavior that is masked in the ensemble, providing insight into the uniformity of the quantum confinement and the degree of electronic delocalization across a heterojunction. Morphologies in which the quantum confinement varies within the particle (due to

the formation of a CdS bulb around the CdSe core, as observed in nanorods) give rise to a lifting of the spectral signature of well-defined quantum confinement by smearing out excitonic transitions. As shown in the single-particle spectrally resolved PLE measurements, band misalignment that is more prevalent in morphologically uniform particles (class A) reveals nonthermalized interfacial excitons, which suggest the presence of an intrinsic barrier to electron transfer between CdS and CdSe. Consequently, whereas particle uniformity and the resulting confinement may be desirable in, for example, light-emitting devices, nanoparticles with low symmetry of the confinement potential (that is, with structural variations: class B) are more suited for light-harvesting applications because of a reduced influence of interfacial barriers. The challenge posed to nanoparticle synthesis is to extend shape engineering to morphology control, so as to create samples in which, for example, all particles exhibit class B morphologies.

5.5 Supporting information

5.5.1 Materials and methods

For the PLE measurements in Figures 5.1, 5.2, and 5.4, tetrapod, rod, and near-spherical structures were all processed from dilute toluene solutions mixed with Zeonex to provide a suitable matrix for deposition on a quartz substrate via spin-coating. For the correlated SEM and PLE measurements, the rods were diluted in a toluene solution without a matrix and then deposited on the silicon reference grids described below. Single particle experiments were carried out in a home-built wide-field low temperature fluorescence microscope operating at 4 K. Circularly polarized laser light was focused onto the sample, mounted on a cold-finger cryostat using silver paste, at an angle of incidence of $\sim 30^{\circ}$. The luminescence was collected with a long working-distance (7.7 mm, numerical aperture 0.55) Olympus microscope objective, projected onto the entrance slit of a 50 cm monochromator (Acton) and detected using a CoolSnap (Princeton Instruments) back-illuminated cooled charge-coupled device (CCD) camera. The wavelength of the exciting laser (Coherent Chameleon Ultra II Ti:Sapphire system, 80 MHz repetition rate, $\sim$140 fs pulse length) could be tuned

automatically, and was frequency-doubled by an APE second-harmonic generation autotracker giving illumination pulses with a spectral bandwidth of 11.8 meV at 400 nm and 13.4 meV at 540 nm. The excitation photon flux was kept constant by varying the laser intensity using an automated neutral density wheel prior to the detection of luminescence at each excitation wavelength. Luminescence was detected either in imaging, using a mirror in the spectrometer, in which case up to 30 single nanoparticles could be tracked in dependence of excitation wavelength simultaneously; or under spectral dispersion where the emission spectrum of up to 5 particles could be recorded as a function of excitation wavelength. We performed several hundred control measurements and always observed light emission from the characteristic CdSe core, which is easily distinguished from CdS by the spectral position and discrete longitudinal optical phonon band. We found no systematic dependence of PLE spectra on excitation density over a fivefold variation in laser power. As nanoparticle blinking increases with photon cycling rate [15] we chose low excitation powers ($\sim$10 W/cm^2 on quartz and $\sim$30 W/cm^2 on Si wafers). CCD exposure times were 3 s for imaging and 10-30 s for spectroscopy. Note that both particle classes displayed comparable emission intensities, blinking, spectral diffusion, single step photobleaching and polarized luminescence as expected for single particle emission. Aggregates of particles exhibit dramatically higher emission intensities and none of these spectroscopic features. Two independent batches of tetrapods and one independent batch of nanorods exhibited both classes of PLE spectra indicating a lack of sensitivity to the synthesis conditions. SEM measurements were conducted on an FEI Field Emission NovaNano 200 with a through-lens detector, a working-distance of $\sim$3 mm, a beam current of $\sim$50 pA, and acceleration voltage of 5 kV. Small landing energies and low dwell times allowed for focusing without inflicting significant degradation on the nanorods.

5.5.2 TEM overview of tetrapod sample

Figure 5.5 provides an overview image of one of the batches of the CdSe/CdS tetrapods used in this study and illustrates the purity of the batch as well as particle

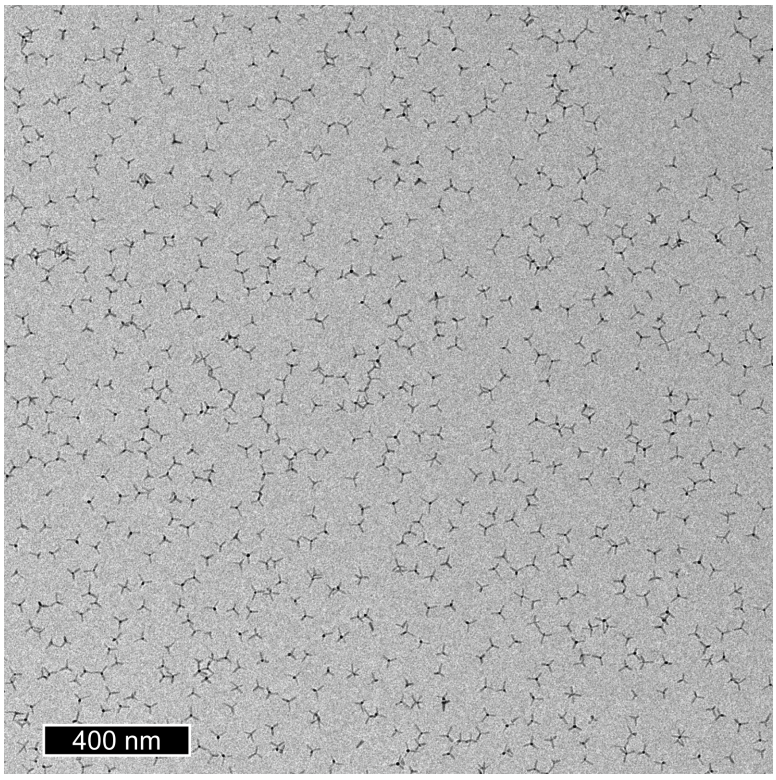

Figure 5.5. Overview TEM image of CdSe/CdS tetrapods used in this study.

uniformity.

5.5.3 Comparison of the ensemble PLE spectrum to the average of single particle PLE spectra

A comparison of ensemble absorption and ensemble PLE of the tetrapods is given in Ref. [5]. Figure 5.6 shows a comparison of the average PLE spectrum of the 150 single tetrapods in Figure 5.2 of the main text to an ensemble PLE spectrum. The ensemble film was prepared in the same manner as the single particle film where the only difference was the concentration of the tetrapod solution, which was 260 times larger than the single particle concentration. While the concentrated solution provided a much denser distribution, microscopy images showed structured emission suggesting that the tetrapods were still isolated from each other, limiting the influence of interparticle effects. The single particle and ensemble PLE spectra in Figure 5.6 were both recorded at 4 K. We note the deviation of the average PLE spectrum from

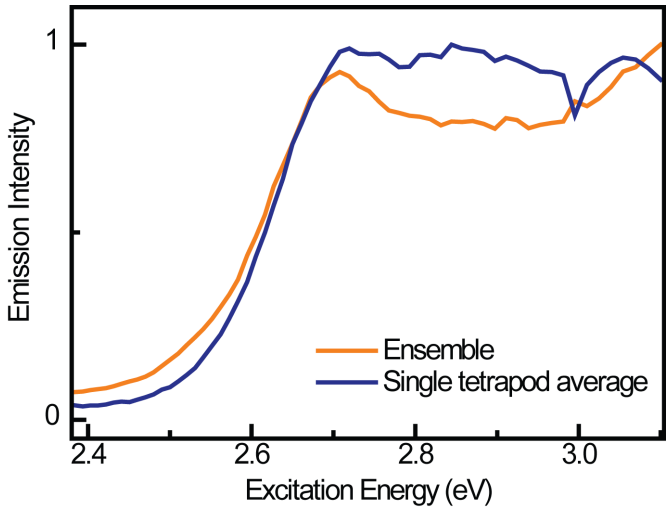

Figure 5.6. Comparison of the ensemble (orange curve) PLE spectrum of tetrapods to the average of the 150 tetrapod spectra presented in Figure 5.2 (blue curve). Both measurements were conducted at 4 K. For a comparison with absorption, see [5].

the ensemble and attribute it to our particle selection process where we chose the most prominent class A and class B particles and excluded irresolvable intermediate cases where the spectrum may be distorted by blinking. For the single particles, the class B particles dominate the average: they are larger than class A particles and on average $\sim 5\times$ brighter. This fact suggests that intermediate-case particles are most likely to be attributable to a class A spectrum, as the ensemble (orange line) shows overall class A characteristics.

5.5.4 Class A and class B designations

To further clarify the process used to discern between the class A PLE spectra and class B PLE spectra displayed in Figure 5.2 of the main text, all of the individual PLE spectra used for Figure 5.2 are plotted in the form of a waterfall plot in Figure 5.7. Although it is difficult to discern an overall characteristic shape due to the large number of PLE spectra (75 for each panel) and the single spectrum noise arising from random fluctuations in nanoparticle PL intensity, each single particle PLE spectrum can be identified and its corresponding class designation can be verified as defined in Figure 5.1 of the main text. To systematically study the different shapes of the PLE

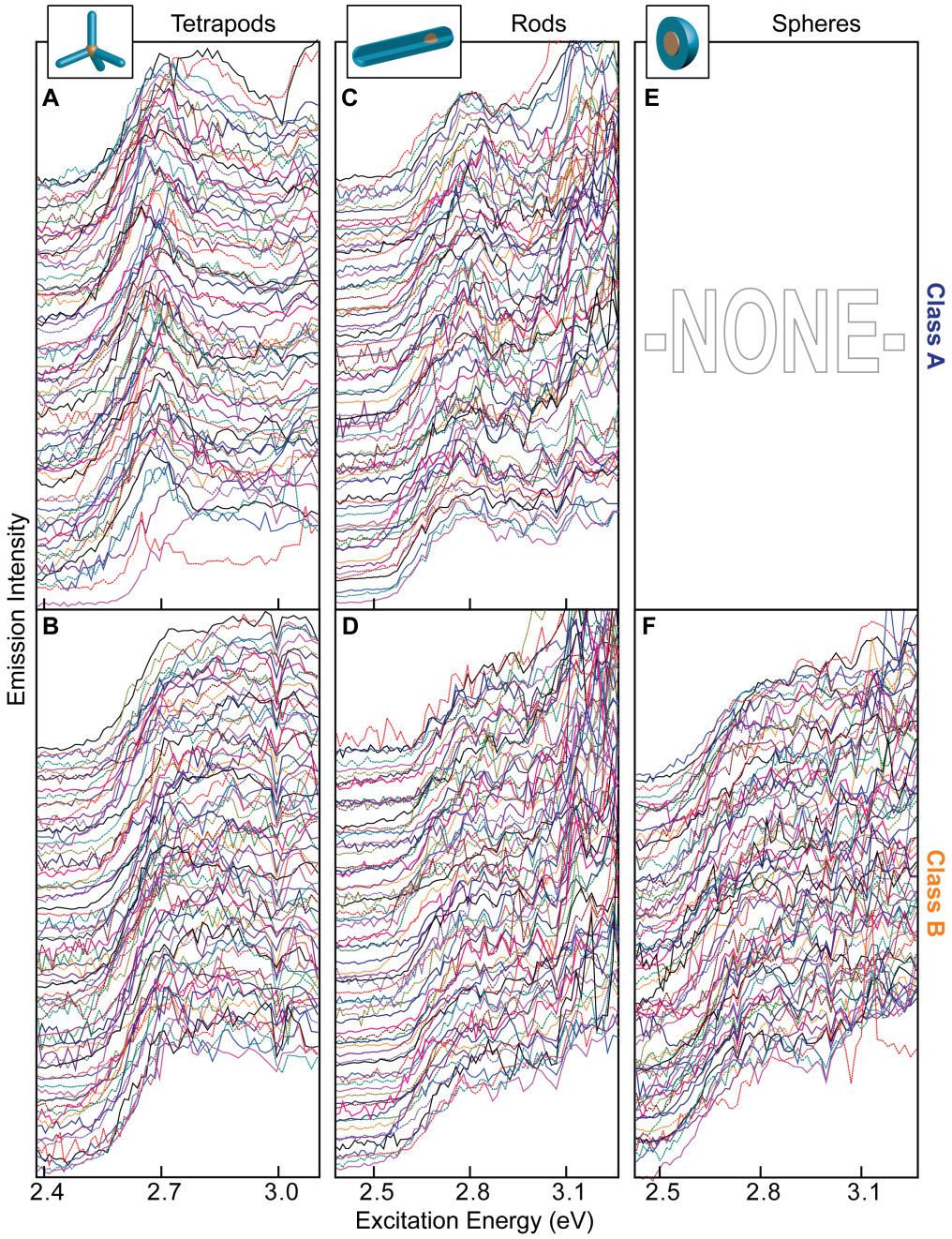

Figure 5.7. Waterfall plot of all individual single particle PLE spectra. The individual single nanoparticle PLE spectra used in Figure 5.2 of the text are plotted in a waterfall configuration to show each individual spectrum (the average of the up and down sweeps in laser excitation energy are plotted). Panels A-F contain the data used in the corresponding panels in Figure 5.2 of the main text. The small feature seen in some of the spectra at 3.0 eV excitation is a residue of the measurement technique and has no physical meaning. It arises due to a slight change in the laser beam profile within the second harmonic generating unit.

spectra, each spectrum was individually inspected to verify the repeatability of the shape over the up and down sweeps in excitation energy. Then, each PLE spectrum was respectively assigned a class A or class B designation depending on the presence or lack of a reduction in emission intensity of at least 20% over a range of at least 50 meV following the CdS absorption onset (see Figure 5.1 of the main text).

To clearly identify statistical trends in the shape of the single particle spectra, each single particle PLE spectrum was normalized such that the emission intensity at the high-energy side of the CdS absorption onset is equal to 1. More precisely, the value used to normalize the curve is the emission intensity (CCD counts) corresponding to the excitation energy where the slope of the PLE spectrum drastically decreases from the initial slope corresponding to the CdS absorption onset. Such normalization allows for comparison of the shapes of single particle PLE spectra with respect to the CdS onset from particles with different overall emission intensities. Accordingly, the normalized data in Figure 5.7 are shown in Figure 5.8 with the PLE spectra colored following their assigned class label. This approach to data representation serves to illustrate the average profile of the two classes of PLE spectra and clearly demonstrates that these two subsets are different. No further manipulation of the raw data has taken place in this case.

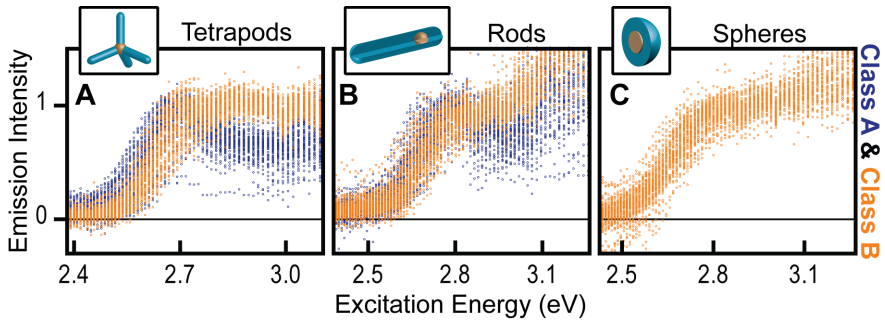

Figure 5.8. Overlaid scatter plot of all individual PLE spectra. Data from Figure 5.7 are normalized and classified as class A or class B highlighting the difference in the average shape of the subsets of particles. Panels A, B, and C contain the 150 tetrapod, 150 rod, and 75 sphere single particle PLE spectra used in Figure 5.2 of the main text colored with their respective class designation.

5.5.5 Correlated TEM and single particle PLE measurements

Transmission electron microscopy (TEM) provides the best resolution to image single nanoparticles to reveal the subtleties in shape, size, and interfaces. We attempted to perform correlated TEM and optical PLE measurements on one and the same CdSe/CdS nanorod, by depositing single particle concentrations onto a TEM substrate that consisted of 24 4 nm thick silicon dioxide (SiO_2) support films reinforced by a 200 nm silicon nitride (Si_3N_4) grid etched in the center of a 200 μm thick silicon wafer (Ted Pella PELCO Silicon Dioxide Support Films, part number 21530-10). The SiO_2 support film is transparent to electrons and is capable of supporting nanoparticles deposited via spin-coating, making it ideal for performing correlated TEM and optical measurements on nanoparticles.

The structure of the TEM grid, however, is not suited for *low temperature* optical measurements. Due to the small thicknesses of the Si_3N_4 grid and the SiO_2 support film, the substrate temperature on the support film cannot reach 4 K using our cold-finger cryostat. Figure 5.9 compares the emission spectrum of a CdSe/CdS nanorod on a SiO_2 support film of a TEM grid that was contacted to the cryostat cold finger at 4 K for over 5 hours to the emission spectrum of a nanorod from the same batch in a matrix (Zeonex, 10 mg/ml) deposited on a quartz substrate. The significantly larger linewidth and red shift of the emission peak indicate that the nanorods on the TEM substrate are significantly closer to room temperature than those on a quartz substrate cooled to 4 K. This behavior was observed on 3 individual samples indicating that thermal contact between the SiO_2 support film and the larger silicon substrate is insufficient to cool the nanorods.

The inability to completely cool the support film on the TEM substrate results in PLE spectra that have a significantly larger signal-to-noise ratio due to increased blinking dynamics of the nanoparticle system. Further, most PLE spectra were not consistent over up and down sweeps of the excitation source impeding the ability to separate true features in the PLE spectra from artifacts due to blinking. Consequently, we were unable to acquire acceptable PLE spectra for rods on a TEM grid for correlated PLE and TEM measurements.

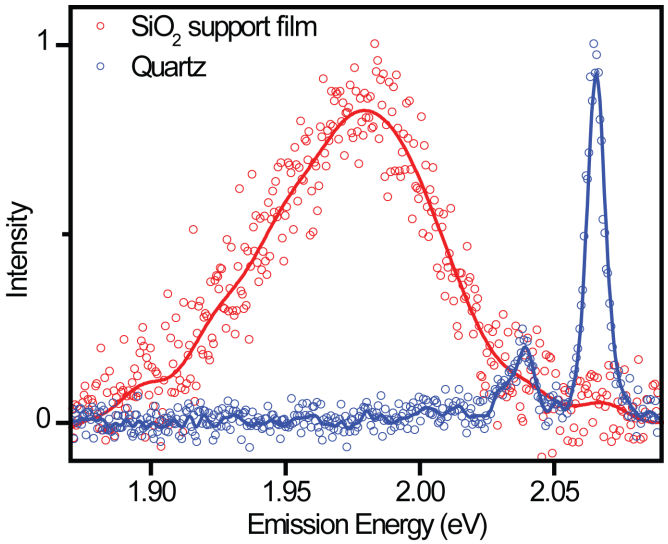

Figure 5.9. Comparison of single CdSe/CdS nanorod emission spectrum on the SiO_2 support film of a TEM grid (red data points) to the emission spectrum of a nanorod embedded in Zeonex on quartz (blue data points). Solid lines are smoothed representations of the corresponding data points and serve as a guide to the eye. Both spectra were taken under cryogenic conditions with the cold-finger of the cryostat at 4 K. The structure of the TEM grid lacks sufficient thermal conductivity to cool the SiO_2 support film to cryogenic temperatures as is evident in the broader, red-shifted emission of the rods on the TEM grid structure compared to those in the Zeonex matrix on a quartz substrate.

5.5.6 Correlation process for SEM and single particle PLE measurements

Imaging the same CdSe/CdS nanorod with SEM that was measured optically allowed us to correlate the nanoparticle shape with its PLE spectrum. All correlated measurements were conducted on a 10 mm × 10 mm n-doped silicon substrate with a layer of native oxide and 50 nm thick chromium reference markings made via optical lithography. The n-doped silicon substrate was used to minimize sample charging during imaging with SEM. Figure 5.10 shows the reference structure. As illustrated in panel A, it consists of 3 styles of 9 grids that contain 16 cells each that are sized to match the field of view of the optical microscope. The nanorods are bright enough that we were able to use the most detailed grid and cell style (second column in the reference structure) allowing us to easily locate the same positions both optically and with SEM. Not shown in the figure is a marking visible to the naked eye used to ensure the same orientation of the sample in the SEM and optical microscope. Each grid structure is labeled at the top with a series of 5 μm × 5 μm boxes representing numbers 1-9 allowing us to easily identify the same grid. The same cell within the grid structure was identified in both microscope systems by the respective style and horizontal position in the grid. Panel B shows the optical microscope image of cell 14 in grid 5. By exciting the region at 410 nm and using a 415 nm long-pass filter in the emission path, we are able to image diffraction-limited luminescence from the nanorods and linear scattering from the edges of the chromium markings. Only the vertical edges of the markings scatter light due to the wide-field illumination configuration of our microscope.

The reference marks on the substrate made correlating high resolution SEM images of the nanorods to their PLE spectra a straightforward process. First, PLE spectra of the nanorods were collected in cells that showed an acceptable concentration of nanoparticles. Following the optical measurements, the PLE spectra were analyzed and cells containing a large number of high quality PLE spectra were chosen to image with SEM. Using the reference markings described in detail above, the same cell was located with the SEM. Subsequently, with the optical image as a guide, high resolution

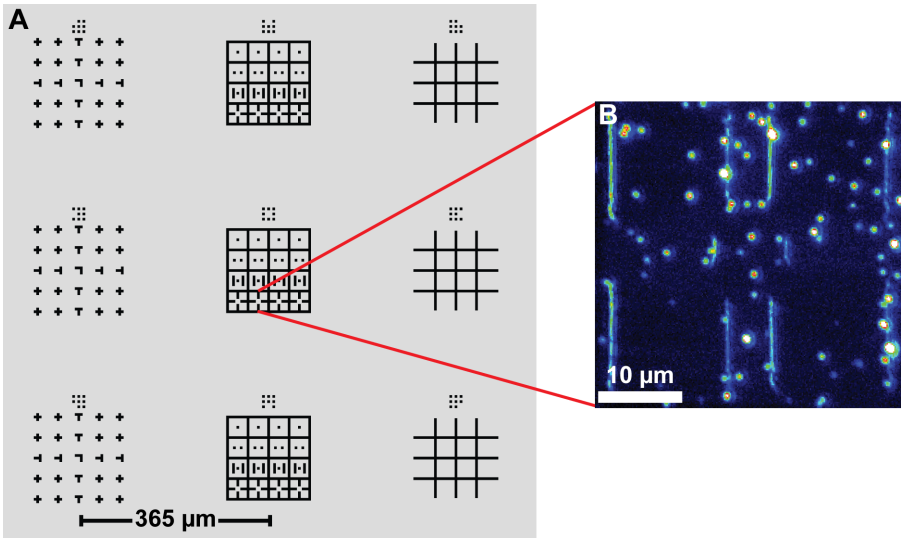

Figure 5.10. Custom reference substrate consisting of 9 grids that contain 16 cells each used for the correlated single-particle PLE and SEM measurements. Black markings (excluding the panel label and scale bar) in panel A are 50 nm thick chromium films deposited on an n-type silicon wafer (gray area) with optical lithography. Panel B displays a false color image of the indicated cell and single nanorods under the optical microscope. Vertical edges in the cell scatter excitation light that leaks through the microscope emission filter, and the diffraction limited spots correspond to luminescence from the single nanorods.

SEM images of the cell were taken in the regions where nanorods were anticipated to lie. For every high resolution image that contained a nanorod, the position of the sample translation stage was recorded. Care was taken to align the electron beam and never use the SEM's beam-shift functionality to maximize the accuracy of the stage coordinates at different magnifications. Upon completing the characterization of a single cell of the reference structure, a lower resolution image of the entire cell was recorded. Due to deposition effects common in SEM, the areas of the higher resolution scans were clearly visible as dark rectangular regions on this overview image. These markings served to verify the positions of the high resolution images of the nanorods on the overview image as initially determined by the sample stage coordinates.

A representative overview image of a cell with visible deposition "scars" from the high resolution scans is shown in panel A of Figure 5.11. The resulting nanorod positions from the placement procedure described above are marked by the annotations on the image. The red circles indicate nanorods that have a corresponding diffraction-limited spot in the optical image of the cell shown in panel B. The white square in both panel A and B highlights the sample region and corresponding luminescent spot that are imaged at a higher resolution in panel C. The white square in panel C encloses the only nanorod identified in that region allowing us to confidently assign the respective PLE spectrum to the nanorod. The blue circle annotation in panel A is a nanorod that was located by SEM but not with optical microscopy indicating that the nanorod is "dark", i.e. it does not show luminescence. To exclude the possibility of correlating dark nanorods to a PLE spectrum, several cells were completely raster-scanned at a high resolution to verify that luminescent nanorods are in the overwhelming majority and the occurrence of dark nanorods is exceedingly rare.

5.5.7 CdS arm emission from class A and class B nanorods

While Figure 5.3 of the main text establishes that the physical shape of a nanorod significantly influences the spectral form of the electronic transitions in the CdS, as a consequence of the quantum confinement effect, shape should also influence

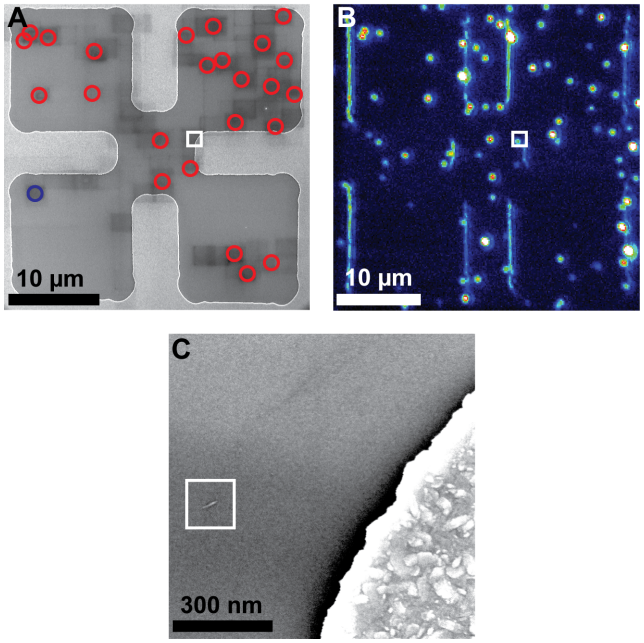

Figure 5.11. Correlation between SEM and optical microscopy. An overview of a single cell on the reference substrate imaged on the SEM is displayed in panel A with the locations of identified nanorods indicated by the annotations. The combined luminescence and scattering image of the same cell obtained on the optical microscope is shown in false color representation in panel B, where the vertical lines are the edges of the chromium markings of the grid, and the diffraction-limited spots correspond to luminescence from single nanorods. A high resolution SEM image of the region denoted by the white square in panel A is shown in panel C and, using simple pattern matching, can be correlated to the diffraction-limited spot marked by the white square in panel B.

the corresponding transition energies. These energies can be probed by spectrally resolving any direct luminescence from the CdS arm, i.e., the weak luminescence from excitons which did not relax to the core. Figure 5.3 shows that a rod exhibiting a class A PLE spectrum has a uniform diameter, whereas a rod with a class B PLE spectrum features a pronounced CdS bulb in the vicinity of the CdSe core. Further, TEM images of the nanorods reveal that those rods with the uniform spatial profile have a smaller diameter (∼6 nm) than those with the bulb-feature (the bulb diameter is ∼10 nm). Since quantum confinement in the rods is strongest in the radial direction (quantified by rod diameter), any CdS emission from class A nanorods should be higher in energy than that from the rods with a class B PLE spectrum due to stronger quantum confinement in the narrower class A particles.

Approximately 13% of the nanorods show detectable emission from the CdS arms due to incomplete energy transfer to the CdSe core. In this case, the CdS emission is significantly dimmer than the emission from the CdSe core, indicating that these rods are still efficient light harvesters. Figure 5.12 shows statistics on the CdS emission energies from 22 class A and 22 class B single nanorods. The probability that a nanorod shows CdS emission does not depend upon its corresponding PLE spectrum as detected under luminescence from the CdSe core: as in the more general case when arm emission is not considered, ∼50% of the nanorods have a class A PLE spectrum while the remaining have a class B PLE spectrum. The average arm emission energy for class A nanorods (panel A) is 2.63 eV, while for class B nanorods (panel B) it is 2.60 eV. Thus the CdS exciton energy in rods with a class B PLE spectrum is ∼30 meV lower than that of rods with a class A PLE spectrum indicating a larger average diameter for nanorods with a class B PLE spectrum. This difference in CdS emission energy, along with the difference in diameter of a uniform rod with respect to a bulb in a non-uniform rod, is in agreement with the quantum-confinement energies and corresponding nanocrystal size of the first electronic transition in CdS as summarized by Yang and Jiang in Ref. [29]. Thus, the spectroscopic data on CdS arm emission confirms that the CdS portion of the nanorods with a class A PLE spectrum is generally smaller in diameter than for rods with a class B PLE spectrum.

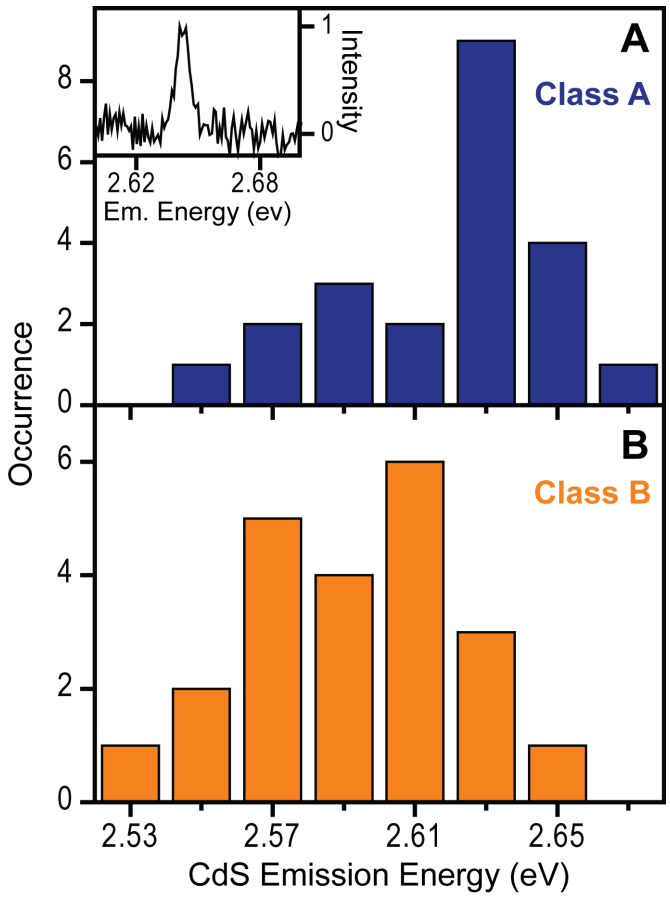

Figure 5.12. CdS arm emission from 22 class A and 22 class B nanorods compared to quantum-confined bandgap energies reported in the literature. The CdS emission from class A nanorods shown in panel A occurs at an average energy of 2.63 eV. In contrast, the average CdS emission for class B nanorods shown in panel B is 30 meV lower in energy than the class A nanorods. Inset in Panel A is a sample spectrum of residual CdS emission from a nanorod at 4 K

5.5.8 Statistical analysis of PLE measurements and particle shape

To assess the statistical significance of the correlation presented in Figure 5.3 of the main text, we applied a simple hypothesis test to the data. We pose the question: what is the probability that the PLE spectrum will predict whether or not a bulb is present on the corresponding nanorod 11 out of 12 times if a correlation does not exist between the PLE spectrum and physical shape? In other words, what is the probability that the correlation depicted in Figure 5.3 happened merely by chance given that nanorods with and without bulbs occur on the substrate with approximately equal probability?

This question is addressed with a simple hypothesis test where the null hypothesis assumes that the PLE spectrum cannot predict the physical shape of the nanorod. The test statistic is the count of successful predictions in the 12 cases depicted in Figure 5.3: the PLE spectrum accurately predicted the shape of the rod in 11 out of 12 trials. The null hypothesis and test are best described by a binomial distribution analogous to a coin-flipping experiment. Thus, we apply a binomial distribution with a trial count of 12 and individual event probability of 1/2.

The probability of the PLE spectrum successfully predicting the shape of x rods out of $n = 12$ trials with a probability $p = 1/2$ per trial is:

$$P(n, x, p) = \begin{pmatrix} n \\ x \end{pmatrix} (p)^x (1-p)^{n-x} \tag{5.1}$$

For significance, the probability of successfully predicting x or more trials should be considered. This probability is calculated with the cumulative distribution function, which is the sum of the individual probabilities:

$$CDF(n, x, p) = \sum_{i=x}^{n} P(n, i, p) \tag{5.2}$$

Table 5.1 lists the probability for all possible values of x as described above. For the situation presented in Figure 5.3 where 11 out of 12 cases were successfully predicted, the probability of this occurring if the null hypothesis is true is 0.32%. Thus, we confidently reject the null hypothesis and claim that the correlation is

Table 5.1. Probabilities from the hypothesis test used assess the significance of the SEM and single particle PLE correlation.

# of correct guesses (x)	# of incorrect guesses ($12 - x$)	Probability assuming null hypothesis ($CDF(12, x, 0.5)$)
≥ 0	≤ 12	1.0000
≥ 1	≤ 11	0.9998
≥ 2	≤ 10	0.9968
≥ 3	≤ 9	0.9807
≥ 4	≤ 8	0.9270
≥ 5	≤ 7	0.8062
≥ 6	≤ 6	0.6128
≥ 7	≤ 5	0.3872
≥ 8	≤ 4	0.1938
≥ 9	≤ 3	0.0730
≥ 10	≤ 2	0.0193
≥ 11	≤ 1	0.0032
≥ 12	≤ 0	0.0002

statistically significant concluding that the PLE spectrum is a reliable predictor of the shape of the corresponding nanorod.

5.5.9 Preliminary statistics on excitation dependent emission

If the systematic dependence of emission energy on excitation energy is a result of the misalignment of the CdSe and CdS conduction bands (Figure 5.4), it should occur more often in nanoparticles that exhibit a class A rather than class B PLE spectrum. The smeared out energy levels in the class B particles (which lead to a broader absorption) will be more likely to align. Preliminary statistics on the occurrence of excitation dependent emission reported in Figure 5.13 suggest that the induced spectral diffusion effect occurs primarily in class A nanoparticles. A total of 50 tetrapods showed a reliable spectrally-resolved PLE spectrum that allowed us to both determine the type of PLE spectrum and detect the systematic change of emission energy in the presence of random spectral diffusion. Of the 50 tetrapods, 30 exhibited a class A PLE spectrum while the remaining 20 showed a class B spectrum.

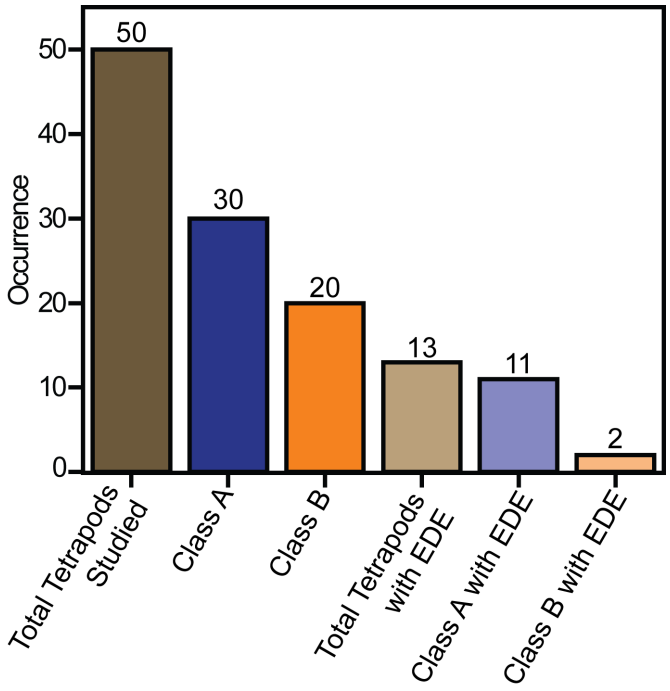

Figure 5.13. Preliminary statistics on the occurrence of excitation dependent emission (EDE) in tetrapods. Fifty total tetrapods were studied where 30 tetrapods exhibited a class A PLE spectrum and 20 had a class B spectrum. Thirteen out of 50 tetrapods showed different emission energies upon directly exciting the core rather than the arm; 11 of which had a class A PLE spectrum while the remaining 2 had a class B spectrum.

Thirteen of the 50 tetrapods showed a detectable change in emission energy when the core was excited as opposed to the arms. Of those 13, 11 tetrapods (85%) had a class A PLE spectrum suggesting that the excitation dependent emission caused by conduction band misalignment is more prevalent in class A particles where the energetic landscape is more well-defined. We expect this effect to be less likely in class B particles, but not completely nonexistent. Furthermore, 11 out of the 30 class A particles showed different emission states providing an initial estimate that 37% of class A particles exhibit some degree of conduction band misalignment giving rise to two nondegenerate ground-state excitons in the system.

5.5.10 Example spectra for excitation dependent emission

To aid in the understanding of the excitation dependent emission data presented in Figure 5.4 of the main text, 6 sample emission spectra are plotted in a conventional format in Figure 5.14. Single tetrapod emission spectra are shown for each tetrapod in Figure 5.4 under direct core excitation at 2.50 eV (panels A, C, and E) and direct arm excitation at 2.70 eV (panels B, D, and F). Note that both the single particle PL linewidths and the electron-phonon coupling strengths and thus the side band

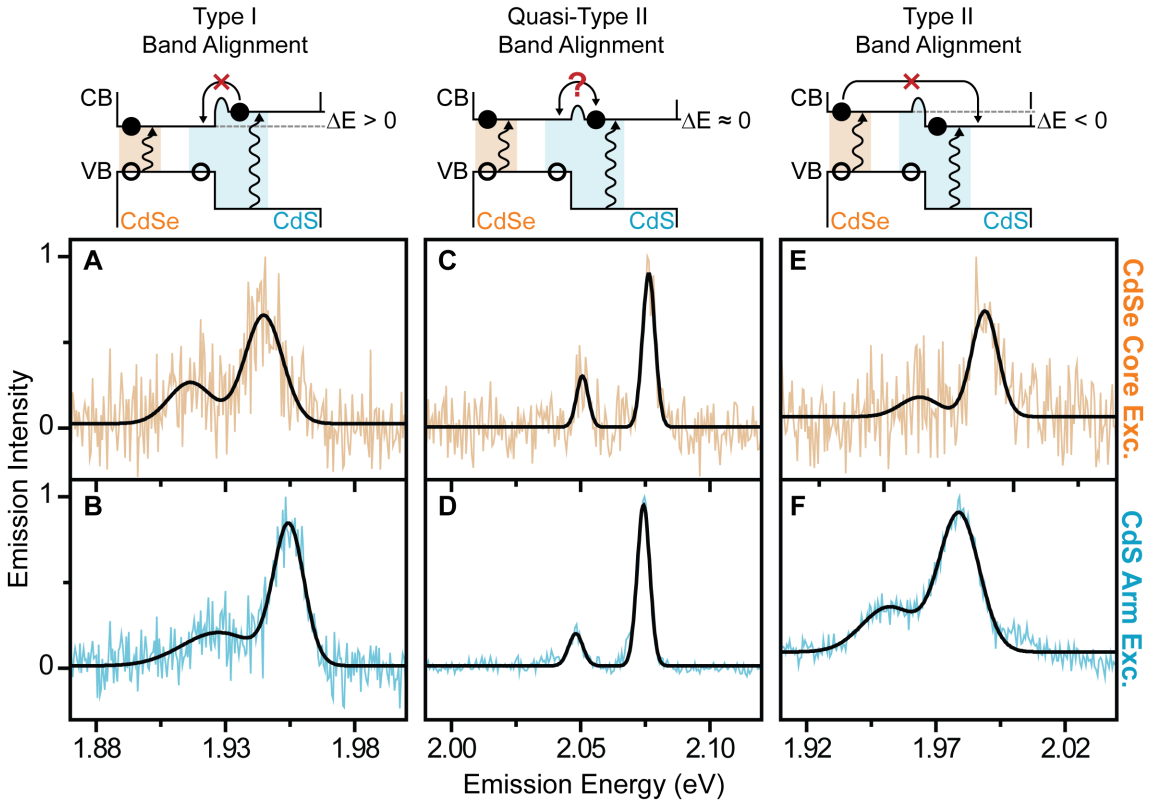

Figure 5.14. Sample single tetrapod emission spectra at 4 K presented in Figure 5.4 of the main text with core excitation at 2.50 eV and arm excitation at 2.70 eV. Panels A and B show that under Type I band alignment, the tetrapod emission is lower in energy with core excitation compared to arm excitation. If the bands align, the tetrapod emission energy does not depend on arm or core excitation as shown in Panels C and D. Finally, with Type II band alignment, panels E and F show that tetrapod emission is higher in energy under core excitation compared to arm excitation. The solid black lines are double Gaussian peak fits that highlight the emission peak positions.

intensities vary significantly from particle to particle, and indeed can change during a single particle PL measurement [14, 15]. This variation is due to the intricacies of spectral diffusion in CdSe nanoparticles, which arises due to temporal changes in local surface charge density. A variation in local charge density effects a changing quantum-confined Stark effect besides modifying the electron-phonon coupling strength of the Fröhlich phonons in these polar crystals [14,15]. The position of the CdSe LO phonon band relative to the electronic transition is constant at 27 meV, as expected [14, 15].

5.6 Acknowledgements

The authors thank K. van Schooten for technical assistance and R. Polson, M. DeLong, and S. Rupich for help with SEM measurements and are indebted to NSF (grants CHE-0748473 and DMR-0213745) and the U.S. Department of Defense Office of Naval Research (grant N00014-10-1-0190). J.M.L. and D.V.T. are fellows of the David and Lucile Packard Foundation.

5.7 References

[1] X. Peng et al., Nature **404**, 59 (2000).

[2] W. U. Huynh, J. J. Dittmer, and A. P. Alivisatos, Science **295**, 2425 (2002).

[3] L. Manna, D. J. Milliron, A. Meisel, E. C. Scher, and A. P. Alivisatos, Nat. Mater. **2**, 382 (2003).

[4] T. Mokari, E. Rothenberg, I. Popov, R. Costi, and U. Banin, Science **304**, 1787 (2004).

[5] D. V. Talapin et al., Nano Lett. **7**, 2951 (2007).

[6] P. V. Kamat, J. Phys. Chem. C **112**, 18737 (2008).

[7] A. Pandey and P. Guyot-Sionnest, Science **322**, 929 (2008).

[8] L. Amirav and A. P. Alivisatos, J. Phys. Chem. Lett. **1**, 1051 (2010).

[9] Y. Qu et al., Nano Lett. **10**, 1941 (2010).

[10] M. J. Walter and J. M. Lupton, Phys. Rev. Lett. **103**, 167401 (2009).

[11] D. Steiner et al., Nano Lett. **8**, 2954 (2008).

[12] A. Sitt, F. D. Sala, G. Menagen, and U. Banin, Nano Lett. **9**, 3470 (2009).

[13] A. Pandey and P. Guyot-Sionnest, J. Chem. Phys. **127**, 104710 (2007).

[14] J. Müller et al., Nano Lett. **5**, 2044 (2005).

[15] S. A. Empedocles, R. Neuhauser, K. Shimizu, and M. G. Bawendi, Adv. Mater. **11**, 1243 (1999).

[16] H. Htoon, P. J. Cox, and V. I. Klimov, Phys. Rev. Lett. **93**, 187402 (2004).

[17] H. Akiyama, M. Yoshita, L. N. Pfeiffer, K. W. West, and A. Pinczuk, Appl. Phys. Lett. **82**, 379 (2003).

[18] T. Ihara et al., Phys. Rev. Lett. **99**, 126803 (2007).

[19] Y. Chen et al., Appl. Phys. Lett. **93**, 053106 (2008).

[20] C. Mauser et al., Phys. Rev. B **77**, 153303 (2008).

[21] E. Yoskovitz, G. Menagen, A. Sitt, E. Lachman, and U. Banin, Nano Lett. **10**, 3068 (2010).

[22] A. Efros and M. Rosen, Annu. Rev. Mater. Sci. **30**, 475 (2000).

[23] T. Vossmeyer et al., J. Phys. Chem. **98**, 7665 (1994).

[24] M. Saba et al., Adv. Mater. **21**, 4942 (2009).

[25] J. Planelles, F. Rajadell, and J. I. Climente, J. Phys. Chem. C **114**, 8337 (2010).

[26] R. G. Neuhauser, K. T. Shimizu, W. K. Woo, S. A. Empedocles, and M. G. Bawendi, Phys. Rev. Lett. **85**, 3301 (2000).

[27] A. M. Smith and S. Nie, Acc. Chem. Res. **43**, 190 (2010).

[28] X. Peng, M. C. Schlamp, A. V. Kadavanich, and A. P. Alivisatos, J. Am. Chem. Soc. **119**, 7019 (1997).

[29] C. Yang and Q. Jiang, Mat. Sci. Eng. B **131**, 191 (2006).

CHAPTER 6

CONCLUDING REMARKS

6.1 Summary

Effectively harnessing the coupling of light to nanoscale semiconductor and metal material systems remains a challenge for material science. Both material systems may play crucial roles in the next generation of photovoltaics, photocatalysts, ultra-sensitive photodetectors, or biological labels and trace analytics [1–3]. This work is a small contribution to the increased understanding of relevant electronic properties of two such systems.

6.1.1 Metal nanoparticle systems

For the silver nanoparticle systems which show pronounced surface-enhanced optical hot spots, several important and interesting results have come from a thorough characterization of the intrinsic linear and nonlinear responses. Perhaps most importantly, the host of spectroscopic data further confirm that few-atom clusters either reside or are photogenerated on these films [4]. These clusters can lie directly in or in close proximity to the film's hot spots, interact with the enhanced electric field and thus have important implications for surface-enhanced Raman scattering (SERS). First, accurate knowledge of the chemical environment of the hot spot is a necessity for a complete understanding of the enhancement mechanism of SERS; the presence carbon-contamination and a native-oxide layer that can dynamically photo-reduce into an emissive silver cluster of varying charge states must be considered for an accurate assessment of the chemical enhancement mechanism [5,6]. Second, this work strongly suggests that the broad background typically associated with SERS [7, 8] arises from the fluorescence of the photogenerated silver clusters within the hot spot, and supports the conclusion that the immediate presence of silver clusters within a

hot spot tends to reduce the hot spot's Raman enhancement ability [9].

While important characterization for SERS comes from the linear response of the metal films, the nonlinear response should not be dismissed. Detailed analysis clearly connects the emission to the surface-enhancement and morphology of the metal film and suggests that the emission comes from similar silver clusters as are identified under linear excitation. Although the origin remains a conjecture, the broadband nonlinear emission has already been effectively utilized as a potential screening method for SERS hot spots [9, 10] as well as a facile light source for high resolution transmission microscopy [11], which is currently under consideration for a patent [12].

On a more fundamental level, the SHG emission arising from rough silver films shows pronounced intensity and polarization fluctuations, which are reminiscent of the blinking observed in single quantum emitters [13–15]. The dynamics reported here are the first known reported fluctuations and appear to be intrinsic to the material system as they remained unchanged by every accessible experimental parameter. Unlike luminescence, SHG emission is typically an ultrafast process that should not involve a long-lived dark state [16], and the origin of the fluctuations remains a mystery. Nevertheless, the fluctuations must be considered and effectively managed when using SHG as a quantitative tool in biological imaging [17].

6.1.2 Semiconductor nanoparticles

The work by M. J. Walter [18] spectroscopically identified the two subensembles of tetrapods, but did not accurately identify the origin. The work presented here continued the investigation by probing two additional morphologies: rods and spheres. The resulting conjecture from the additional data was unequivocally confirmed with the formidable task of correlating single particle spectroscopic measurements to high resolution electron microscopy for the rods. The end result was an explicit confirmation of what many chemists readily assumed: anisotropic morphologies and the resulting variation in quantum confinement potential "smear" out well-defined electronic states in these nanoparticle systems. However, the anisotropy may not necessarily be a bad thing as the more uniform particles appear to be more susceptible to interfacial barriers that prevent complete energy transfer to a light-harvesting

center. The insight gained suggests crucial structural goals for specifically tailoring semiconductor nanoparticle structures depending on the desired application.

6.2 Future directions

It is rare for scientific work to entirely conclude and comprehensively answer every question. More often, rather, answering one question exposes several more mysteries and opportunities. Accordingly, there remains a large variety of additional projects of varying complexity which would nicely augment this work. Some of these include:

- *Origins of broadband nonlinear emission*: the broadband nonlinear emission is often referred to as two-photon luminescence [19]. However, its ultrafast decay presented in this work seems to suggest that it is a process that may be coherent. A definitive understanding of this emission would be invaluable to those who use it to characterize metal nanoparticle systems.

- *Origins of SHG blinking*: every experimental parameter available was varied to try and influence the observed SHG blinking but did not show influence. Thus, the origins of the SHG blinking remain unknown, and can only be speculated to be electrical charging of small metal nanoparticles. Further studying of this effect may have to make use of a novel experimental apparatus that is able to isolate the SHG signal from the CE background and monitor it on much faster timescales than presented here.

- *Emissive silver clusters*: while the presence of emissive silver clusters is considered primarily parasitic in this work, they are gaining increased attention because of their catalytic properties [20–22]. The Tollens film may provide an avenue for few-atom silver cluster production and isolation.

- *Hot spot excitation spectroscopy*: preliminary results indicate that the average energetic *width* of the excitation resonances of the hot spots of the Tollens films depends upon morphology. The transition from discrete metallic nanoparticles with broad resonances to complex aggregate formations with narrow resonances may be observed by investigating how linear and nonlinear excitation spectra of

hot spots change as a function of growth time. Such a measurement would be an experimental realization of the "bottom-up" approach used in Chapter 1 to describe the surface plasmon modes of nanoparticle aggregates. Furthermore, localization microscopy techniques [23], can potentially be used to identify spatial shifts below the diffraction-limit of hot spot emission positions as a function of excitation energy.

- *Polarization anisotropy of semiconductor heterostructures*: in general, shape anisotropy leads to increased polarization of the emission for semiconductor nanoparticles [24]. However, this concept has yet to be *explicitly* confirmed on the single particle level. In principle, the techniques applied in Chapter 5 can be used to directly project an emission and excitation dipole onto a single nanoparticle. While the results are easily anticipated they are not guaranteed.

- *Multiparticle interactions between semiconductor heterostructures*: the interactions between particles, such as energy transfer, are important to fully understand in the context of device applications such as photovoltaics [18]. By modifying the single-particle deposition process, small aggregate formation of semiconductor nanocrystals may be achieved. The optical properties of these aggregates, including excitation spectroscopy and polarization anisotropy, can then be probed and correlated with high resolution electron microscopy in a similar fashion as Chapter 5. Such measurements could provide detailed information on interparticle dynamics in small nanocrystal aggregates.

At the highest level, the goal of this work was to derive detailed structural information from in-depth optical measurements. While both semiconductor and metal nanoparticle systems have been studied by a large number of research groups for a relatively long stretch of time, this work shows that a lot can still be learned about the physical and electronic characteristics of these systems from diligent and careful analysis of optical measurements.

6.3 References

[1] D. V. Talapin, J. S. Lee, M. V. Kovalenko, and E. V. Shevchenko, Chem. Rev. **110**, 389 (2010).

[2] P. V. Kamat, J. Phys. Chem. B **106**, 7729 (2002).

[3] K. Kneipp, H. Kneipp, I. Itzkan, R. Dasari, and M. Feld, Chem. Rev. **99**, 2957 (1999).

[4] L. A. Peyser, A. E. Vinson, A. P. Bartko, and R. M. Dickson, Science **291**, 103 (2001).

[5] A. Otto, M. Lust, A. Pucci, and G. Meyer, Can. J. Anal. Sci. Spectrosc. **52**, 150 (2007).

[6] M. Moskovits, J. Raman Spectrosc. **36**, 485 (2005).

[7] N. Pieczonka and R. Aroca, ChemPhysChem **6**, 2473 (2005).

[8] T. Itoh et al., J. Chem. Phys. **124**, (2006).

[9] M. J. Walter, N. J. Borys, G. Gaefke, S. Höger, and J. M. Lupton, J. Am. Chem. Soc. **130**, 16830 (2008).

[10] E. D. Diebold, P. Peng, and E. Mazur, J. Am. Chem. Soc. **131**, 16356 (2009).

[11] D. Chaudhuri et al., Nano Lett. **9**, 952 (2009).

[12] J. M. Lupton et al., Subdiffraction wide-field white light transmission microscopy of near-opaque media *U.S. patent application Serial No. 61/080,097, 2008, pending.*

[13] R. Verberk and M. Orrit, J. Chem. Phys. **119**, 2214 (2003).

[14] M. Nirmal et al., Nature **383**, 802 (1996).

[15] F. D. Stefani, J. P. Hoogenboom, and E. Barkai, Phys. Today **62**, 34 (2009).

[16] R. W. Boyd, *Nonlinear Optics*, Academic Press, 2003.

[17] N. Hodas, (private communication).

[18] M. J. Walter, *Light-harvesiting in single conjugated polymer chains and semiconductor nanocrystals*, PhD thesis, University of Utah, 2009.

[19] M. R. Beversluis, A. Bouhelier, and L. Novotny, Phys. Rev. B **68**, 115433 (2003).

[20] Y. Lei et al., Science **328**, 224 (2010).

[21] P. Gruene et al., Science **321**, 674 (2008).

[22] Z. Y. Li et al., Nature **451**, 46 (2008).

[23] A. McLeod et al., Phys. Rev. Lett. **106**, 037402 (2011).

[24] J. Hu et al., Science **292**, 2060 (2001).